ISSN 1816-112X

Science Citation Index Expanded, Materials Science Citation Index and ISI Alerting

Advanced Steel Construction
an international journal

Cover: The 139mx73m clear span Spectacle Roof designed by Second-order Direct Analysis without assumption of effective length

e-copy of IJASC is free to download at "www.ascjournal.com" in internet and mobile apps.

General Information
Advanced Steel Construction, an international journal

Aims and scope

The International Journal of Advanced Steel Construction provides a platform for the publication and rapid dissemination of original and up-to-date research and technological developments in steel construction, design and analysis. Scope of research papers published in this journal includes but is not limited to theoretical and experimental research on elements, assemblages, systems, material, design philosophy and codification, standards, fabrication, projects of innovative nature and computer techniques. The journal is specifically tailored to channel the exchange of technological know-how between researchers and practitioners. Contributions from all aspects related to the recent developments of advanced steel construction are welcome.

Instructions to authors

Submission of the manuscript. Authors may submit on-line at **www.hkisc.org**

Asian Pacific , African and organizing editor :	Professor S.L. Chan, Email: ceslchan@polyu.edu.hk
American editor :	Professor W.F. Chen, Email: waifah@hawaii.edu
European editor :	Professor R. Zandonini, Email: riccardo_zandonini@ing.unitn.it

All manuscripts submitted to the journal are recommended to accompany with a list of four potential reviewers suggested by the author(s). This list should include the complete name, address, telephone and fax numbers, email address, and at least five keywords that identify the expertise of each reviewer. This scheme will improve the process of review.

Style of manuscript

General. Author(s) should provide full postal and email addresses and fax number for correspondence. The manuscript including abstract, keywords, references, figures and tables should be in English with pages numbered and typed with double line spacing on single side of A4 or letter-sized paper. The front page of the article should contain:

a) a short title (reflecting the content of the paper);
b) all the name(s) and postal and email addresses of author(s) specifying the author to whom correspondence and proofs should be sent;
c) an abstract of 100-200 words; and
d) 5 to 8 keywords.

The paper must contain an introduction and a conclusion. The length of paper should not exceed 25 journal pages (approximately 15,000 words equivalents).

Tables and figures. Tables and figures including photographs should be typed, numbered consecutively in Arabic numerals and with short titles. They should be referred in the text as Figure 1, Table 2, etc. Originally drawn figures and photographs should be provided in a form suitable for photographic reproduction and reduction in the journal.

Mathematical expressions and units. The Systeme Internationale (SI) should be followed whenever possible. The numbers identifying the displayed mathematical expression should be referred to in the text as Eq. 1, Eq. 2.

References. References to published literature should be referred in the text, in the order of citation with Arabic numerals, by the last name(s) of the author(s) (e.g. Zandonini and Zanon [3]) or if more than three authors (e.g. Zandonini et al. [4]). References should be in English with occasional allowance of 1-2 exceptional references in local languages and reflect the current state-of-technology. Journal titles should be abbreviated in the style of the Word List of Scientific Periodicals. References should be cited in the following style [1, 2, 3].

Journal: [1] Chen, W.F. and Kishi, N., "Semi-rigid Steel Beam-to-column Connections, Data Base and Modelling", Journal of Structural Engineering, ASCE, 1989, Vol. 115, No. 1, pp. 105-119.

Book: [2] Chan, S.L. and Chui, P.P.T., "Non-linear Static and Cyclic Analysis of Semi-rigid Steel Frames", Elsevier Science, 2000.

Proceedings: [3] Zandonini, R. and Zanon, P., "Experimental Analysis of Steel Beams with Semi-rigid Joints", Proceedings of International Conference on Advances in Steel Structures, Hong Kong, 1996, Vol. 1, pp. 356-364.

Proofs. Proof will be sent to the corresponding author to correct any typesetting errors. Alternations to the original manuscript at this stage will not be accepted. Proofs should be returned within 48 hours of receipt on-line.

Copyright. Submission of an article to "Advanced Steel Construction" implies that it presents the original and unpublished work, and not under consideration for publication nor published elsewhere. On acceptance of a manuscript submitted, the copyright thereof is transferred to the publisher by the Transfer of Copyright Agreement and upon the acceptance of publication for the papers, the corresponding author must sign the form for Transfer of Copyright.

Permission. Quoting from this journal is granted provided that the customary acknowledgement is given to the source.

Page charge and Reprints. There will be no page charges if the length of paper is within the limit of 25 journal pages. A total of 30 free offprints will be supplied free of charge to the corresponding author. Purchasing orders for additional offprints can be made on order forms which will be sent to the authors. These instructions can be obtained at the Hong Kong Institute of Steel Construction, Journal website: http://www.hkisc.org

The International Journal of Advanced Steel Construction is published quarterly by learnt society, The Hong Kong Institute of Steel Construction, c/o Department of Civil & Environmental Engineering, The Hong Kong Polytechnic University, Hung Hom, Kowloon, Hong Kong.

The Hong Kong Institute of Steel Construction
HKISC
c/o Department of Civil and Environmental Engineering,
The Hong Kong Polytechnic University,
Hunghom, Kowloon, Hong Kong, China.
Tel: 852- 2766 6047 Fax: 852- 2334 6389
Email: *ceslchan@polyu.edu.hk* Website: *http://www.hkisc.org/*
ISSN 1816-112X
Science Citation Index Expanded, Materials Science Citation Index and ISI Alerting

ISSN 1816-112X

Science Citation Index Expanded, Materials Science Citation Index and ISI Alerting

Advanced Steel Construction
an international journal

VOLUME 13 NUMBER 1 MARCH 2017

Technical Papers

REFLECTOR WIND LOAD CHARACTERISTICS OF THE LARGE ALL-MOVABLE ANTENNA AND ITS EFFECT ON REFLECTOR SURFACE PRECISION

Yan Liu*[,1], Hong-liang Qian[2] and Feng Fan[2]

[1] *School of Civil Engineering, Chang'an University, Xi'an 710061, P.R.China*
[2] *School of Civil Engineering, Harbin Institute of Technology, Harbin 150090, P.R.China*
**(Corresponding author: E-mail: actor_liu@126.com)*

Received: 23 August 2015; Revised: 19 January 2016; Accepted: 20 February 2016

ABSTRACT: The wind load could cause the deformation of the reflector surface, seriously affect the resolution and the sensitivity of the antenna and degrade its performance. So the analysis of the wind characteristics of the reflector surface is particularly important. For one thing, the wind loads acting on an open parabolic reflector, as a commonly used type of reflector (F/D=0.3), are obtained by the wind tunnel test and CFD technique and wind characters of the parabolic reflector are revealed. Wind-induced dynamic behaviors under different upwind profiles are also analyzed by the finite element method (FEM). After that based on the numerical simulation, a large number of different kinds of reflectors are researched and analyzed and the results for different diameters, focal length to diameter ratios are acquired to provide sufficient information for wind force proofing design of the antenna structures. Finally, taking the established 110m antenna structure as the example and based on the instantaneous pressures derived from the wind tunnel tests, the mechanic performances of the structure at the survival wind speed and working speed are respectively investigated, and consequently the reliability of its mechanic performance is evaluated. The surface RMS of structural responses under various wind loads conditions and internal mechanisms are finally discussed to provide valuable data for the deformation control of the actuators in further work.

Keywords: Antenna structure, Wind tunnel test, Numerical simulation, Wind-induced vibration response, Wind force proofing design.

DOI: 10.18057/IJASC.2017.13.1.1

1. INTRODUCTION

As a multi-functional, automatic, high-integrated electronic mechanical equipment, the radio telescope structure is subjected to random wind load in the operation of variable-position rotation, which causes the surface deviation of deformed reflector from the theoretical designed reflector. This error has an important influence on the surface accuracy of the reflector [1-3].

For the calculation of wind load, the wind pressure distribution on the reflector surface is required. The influence factors on the distribution are complex and diverse, not only by the wind turbulence in the wind, but also by the wind angle, pitch angle of the antenna structure, the geometrical characteristics of the reflector surface and so on. From the view of the present situation of the domestic application, Miyun 50m antenna in Beijing, Shanghai 65m antenna and 110m to be built in Xinjiang all belongs to the same category of the all-movable radio telescope which has a focal length to diameter ratio of 0.3, a circular aperture and parabolic reflector. This situation reflects that the geometric characteristics of the reflector are very common. From the research status of wind force proofing design for the antenna structures, foreign scholars have carried out the wind tunnel test at 4 upwind attitudes for the focal length to diameter ratios 0.5 and 0.25 respectively and acquired the average wind pressure distribution. It can be seen in this achievement the analysis cases for different upwind attitudes are scarce. In domestic the wind tunnel tests study for the focal length to diameter ratio 0.3 with 12 upwind attitudes have been carried out to give the overall drag

coefficient of reflector but the average wind pressure distribution of the surface is not given. According to the Load Code for the Design of Building Structures, facing the results achieved, although the spherical shell in the geometrical shape is the most close to the parabolic surface, there are still some differences between the two above. Simultaneously the results of the spherical shell derive from the enclosed structure yet the reflector of the antenna in wind field belongs to an open type structure. So the circling flow characteristics around for the two types of structures are quite different.

It can be seen that the research results of this kind of structure are not comprehensive. The comprehension for its wind load and wind induced vibration response characteristics is very poor. It is necessary to carry out a large number of wind tunnel tests and numerical simulations for the reflector structure and provide the meaningful references for the wind load proofing design of the antenna structure and the valuable data for the deformation control of the actuators caused by the wind load.

2. CFD NUMERICAL SIMULATIONS

In this work the research objects are different radio telescopes so in the numerical simulation the grid division strategy is significant to solve the FEM [4-7]. The problems need to be done reflect in that the reflector has an open parabolic surface, it is difficult to deal with the grid division around the surface area and not easy to form a high quality grid. So it is intended to make a hybrid mesh for the computational domain. Meanwhile it is necessary to increase the grid around the upper and lower surface, adjust the gradient ratio of the grid and the y^+ value near the surface boundary to further improve the mesh quality and calculation accuracy.

Where，y^+ is introduced to represent the distance from the centroid of the near wall mesh to the wall surface. This dimensionless quantity is related with speed, viscosity and shear stress of the fluid. The specific division is illustrated in section 2.3.

2.1 Computational Domain Settings

In the numerical simulation of wind pressure distribution the computational domain is closed by setting several wall surfaces to guarantee the blocking probability is less than 5%. So it is necessary to determine the appropriate computational domain. Computational domain comprises upper reaches L_1, lower reaches L_2, windward width B, and height H. The computational domain is shown in Figure 1 [8-9] and each parameter set is list in Table 1.

a）Longitudinal section of computational domain

b) Horizontal plane of computational domain

Figure 1. Configuration Items of the Computational Domain

Table 1. Computational Field Setting

Model size	$l \times b \times h$
Computational domain	$L_1 = 5l$， $L_2 = 15l$， $H = 8h$， $B = 10b$

2.2 Turbulence Model and Boundary Conditions

According to the references the complete Reynolds stress model has a relatively high accuracy for solving the flow around a bluff body and its use range is wide. So in this work the RSM turbulence model is used to solve the constant pressure field around a constant flow of the reflector structure. The boundary conditions of the model are set in Table 2.

2.3 Meshing

Meshing has a direct influence on the results of numerical simulation and is mainly embodied with the gird size and the grid type. Based on many times in meshing for the flow field around the reflector structure, finally the grid type and grid quantity adopted for each part of the flow field are shown in Table 3 and Figure 2.

1）The outside domain uses the structural hexahedral mesh which could provide a fine grid size, decrease the grid quantity and guarantee the grid quality. While the inside domain uses unstructured tetrahedral grid which could achieve effective meshing to the flow field around the reflector structure.

Table 2. Boundary Condition Setting in CFD

Inlet boundary condition	Shear flow is considered: wind profile $V_z = V_{10}(z/10)^{\alpha}$, geomorphic type B $\alpha = 0.15$, $V_{10} = 33.5m/s$ according to the basic wind pressure. The governing equations of the incompressible turbulent wind flow around buildings are presented by the RANS equations as follows. $\frac{\partial u_i}{\partial x_i} = 0$, $\frac{\partial}{\partial x_j}(\rho u_j u_i) = -\frac{\partial p}{\partial x_i} + \frac{\partial}{\partial x_j}[\mu(\frac{\partial u_i}{\partial x_j} + \frac{\partial u_j}{\partial x_i}) - \rho\overline{u_i' u_j'}]$. Turbulence properties are defined by means of kinetic energy and turbulent dissipation rate. $k = 1.5(V_Z \cdot I)^2$, $\varepsilon = \frac{1}{l}0.09^{\frac{3}{4}}k^{\frac{3}{2}}$. Where l represents turbulent characteristic scale, and I represents turbulent intensity. Turbulent intensity of the incoming flow: Refers to data of the second geomorphic type in Australia Code[10-11]. Reference coordinate system: Y axis represents the length direction of the computational domain and Z represents the height direction of the structure.
Outlet boundary condition	Fully developed flow boundary condition is adopted and the normal gradient of any physical quantity ψ in the flow field is zero.
Wall condition	Top and both sides computational domain: free slip wall condition. Reflector surface and ground: no slip wall condition.

2) Because the parabolic reflector has a gradient of spatial curvature and the thickness of the model is only 100mm. The near wall region adopts the prismatic boundary layer grid to realize the precise control to the meshing and meet the requirements of the minimal wall distance [12-15]. The distance can be characterized by the dimensionless value y^+ which could be expressed in formula (1). The closest grid point near the wall surface is adopted to be 0.025D, with corresponding wall unit y+ ranging from about 8~30. The determination of y+ is controlled and realized by mesh division.

$$y^+ = \frac{\rho u_\tau y}{\mu} \quad (1)$$

Where u_τ represents the frictional velocity, y represents the normal distance from the nodes in the first row to the wall surface. ρ represents the air density, and μ represents the kinematic coefficient of viscosity.

Table 3. Mesh Division for Calculation Area in the Flow Field

Model	Computational domain	Mesh type	Mesh quantity
Parabolic reflector	Outside domain	Structured hexahedral mesh	1000,000
	Inside domain	Unstructured tetrahedral mesh	500,000
	Near wall region	Prismatic boundary layer mesh	150,000

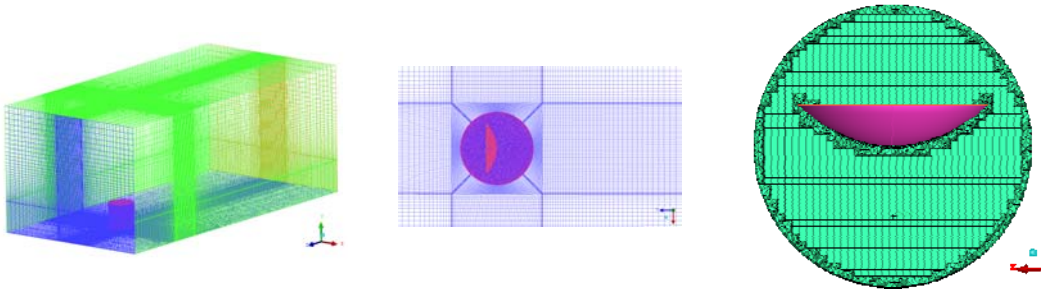

a) Outer calculation domain b) Inner calculation domain c) Domain of near the wall

Figure 2. Mesh of the Numerical Domain

2.4 Analysis Cases

The wind direction is defined as shown in Figure 3. According to the symmetry of the model, the wind angle for test is selected about every 30° in the range of 0°to 180°. In the pitching rotation the angles of 5°, 30°, 60° and 90° are selected for test. Based on the above parameters there are 22 analysis cases in total (For the pitch angle of 90°, any wind direction is polar symmetrical about the central axis of the reflector so a kind of wind angle is enough).

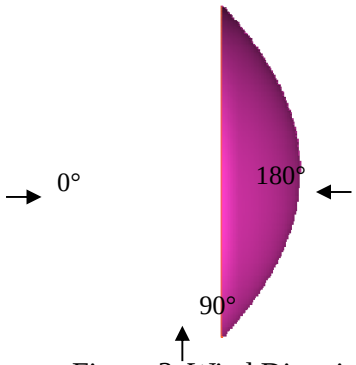

Figure 3. Wind Direction Angle

2.5 CFD Simulation Results

The numerical simulations are carried out by the software Fluent and the average wind pressure distribution on the reflector surface is described in the form of contour by the software Tecplot, shown in the Figure 4~7. From the figures, under the pitch angle of 5° for the model, when the

wind angle is less than 90° the reflector surface is completely under the positive pressure and with the increase of the wind angle, the partial pressure coefficient of the edge region increases. When the wind angle is 90°for the same pitch angle, the negative pressure begins to appear on the reflector surface as the wind suction and the wind pressure distribution along the wind direction is basically symmetrical. The negative pressure area of the reflector surface gradually expands with the increase of the wind angle till the wind angle runs up to 180°, the reflector surface is completely under the negative pressure. When the pitch angle of the model is 30° or 60°, the wind pressure distribution of the reflector surface is similar to that of the 5° pitch angle model. In addition, under the same direction with the increase of the pitch angle, the local positive pressure coefficient increases and the distribution area expands. Especially for the pitch angle of 60° under the wind angle of 60°, the maximum positive pressure coefficient reaches 1.9. The wind pressure distribution on the reflector surface not only has a good symmetry but also shows the maximum negative pressure in the front edge of the windward side for the pitch angle of 90° under the wind angle of 0°. Meanwhile the absolute value of the negative pressure coefficient gradually decreases and turns to the positive pressure along the flow direction. In the lower reaches the positive pressure begins to increases and the positive pressure area is greater than that of the negative area in general.

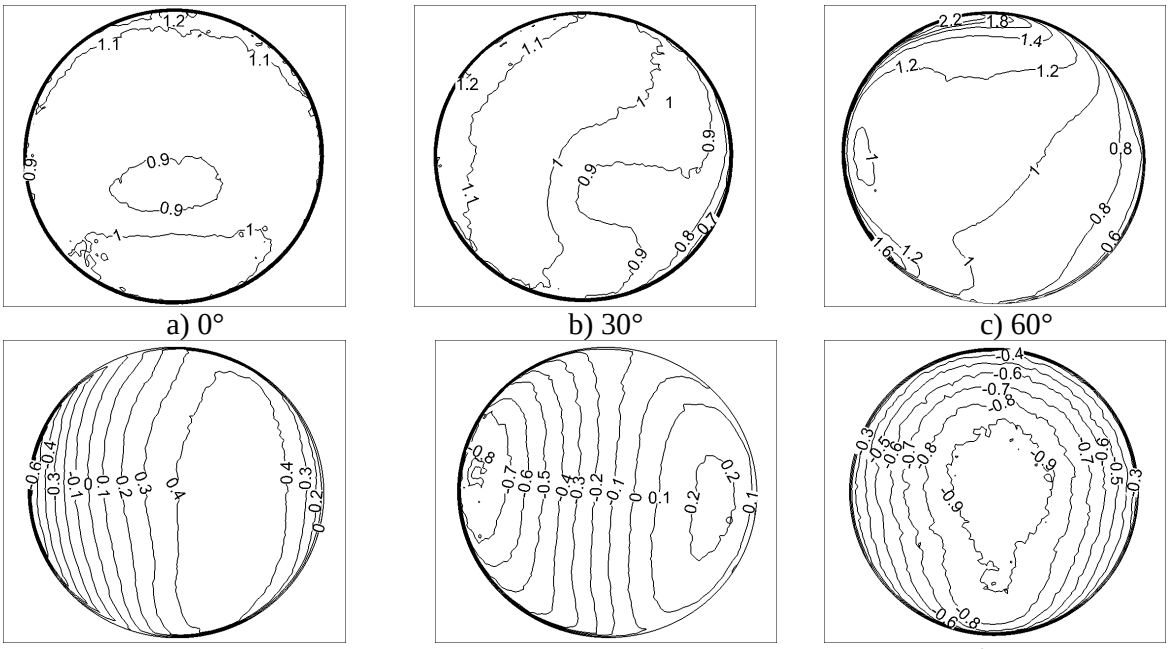

a) 0° b) 30° c) 60°

d) 90° e) 120° f) 180°

Figure 4. Mean Wind Pressure Coefficients of Reflector under Different Wind Angles for 5°Pitch Angle

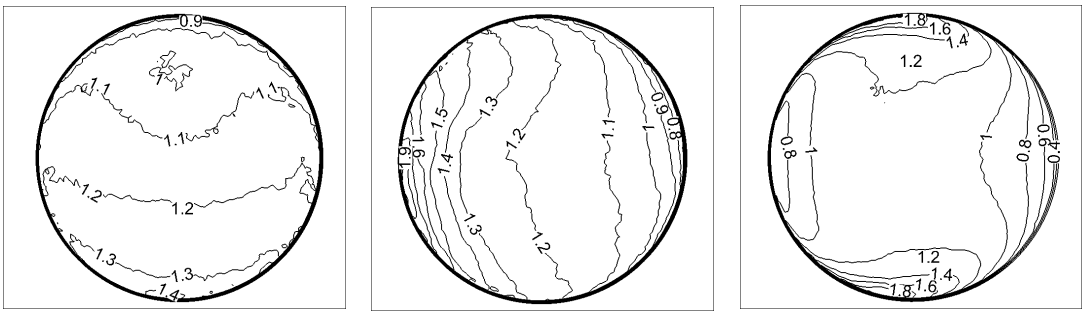

a) 0° b) 30° c) 60°

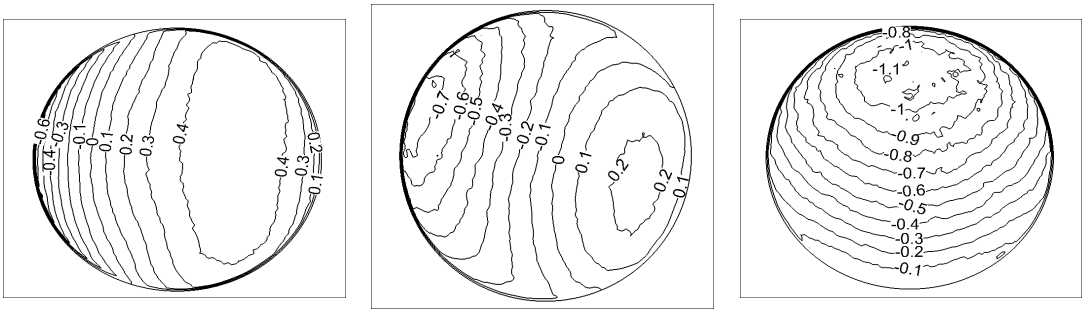

d) 90° e) 120° f) 180°

Figure 5.Mean Wind Pressure Coefficients of Reflector under Different Wind Angles for 30°Pitch Angle

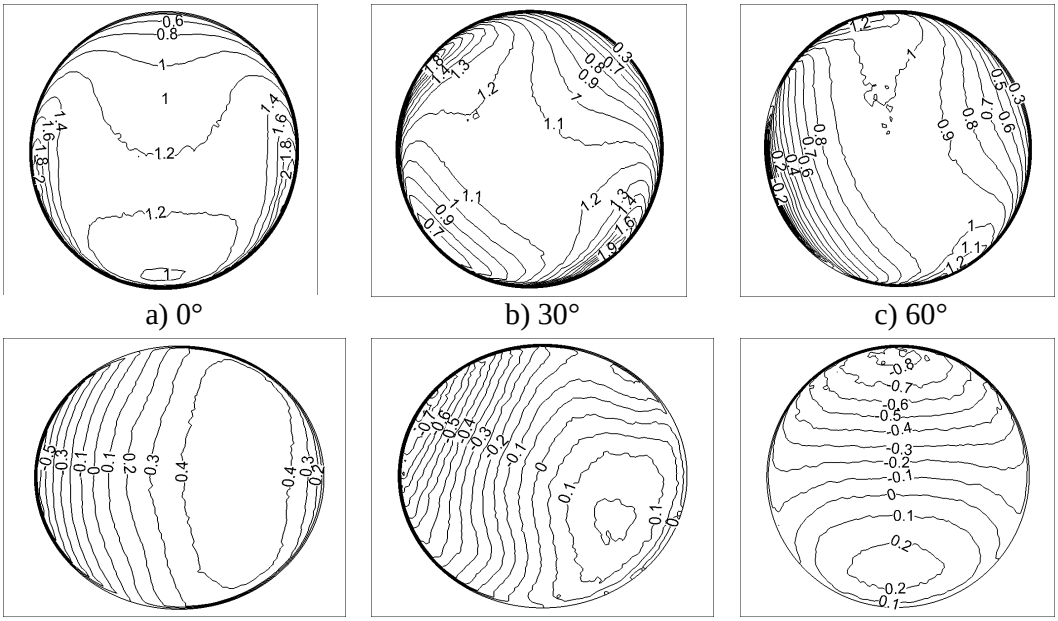

a) 0° b) 30° c) 60°

d) 90° e) 120° f) 180°

Figure 6. Mean Wind Pressure Coefficients of Reflector under Different Wind Angles for 60°Pitch Angle

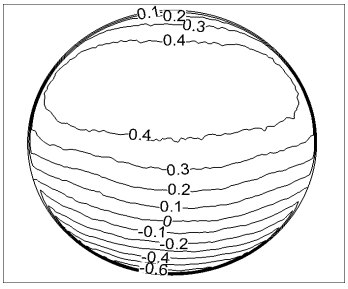

Figure 7. Mean Wind Pressure Coefficients of Reflector for 90°Pitch Angle

3. WIND TUNNEL TEST

In order to verify CFD numerical simulation validity for parabolic reflector structure, scale model test for the 110m (F/D=0.3) reflector structure is carried out in the wind tunnel. The test cases concur with the simulation cases and the test is the manometric test of rigid models. By comparison

between the test and simulation, the wind pressure characteristics of the parabolic reflector structure are described furtherly and the internal mechanism is revealed.

3.1 Wind tunnel facility and measurement system

The manometric test is carried out in the State Key Laboratory for Wind Tunnel and Water flume in Harbin Institute of Technology. The wind tunnel has a double closed test section with the single reflow (shown in Figure 8). The laboratory is a comprehensive experiment platform which integrates the wind field simulation of the near ground surfaces, the deep ocean wave simulation and the rainfall simulation. The small section is 4m in width, 3m in height and 25m in length and the testing wind speed is 3m/s~50m/s. The big section is 6m in width, 3.6m in height and 50m in length and the testing wind speed is 3m/s~27m/s. This work is carried out in the small testing section.

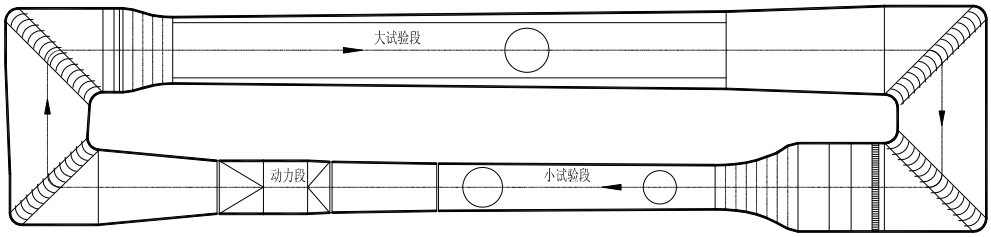

Figure 8. Outline Drawing of Wind Tunnel in HIT

Manometry system uses the electronic pressure scanning valve system produced by Scanivalve scanning company in the USA for scanning and measurement. Finally, the data is recorded and processed by the signal acquisition and data processing software realized in the PC, shown in the Figure 9.

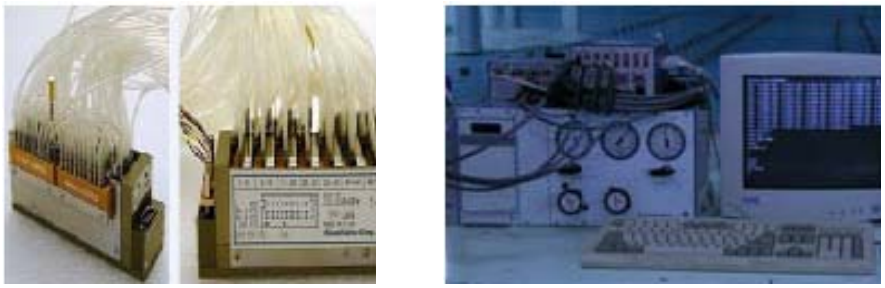

Figure 9 Electronic pressure scanner system for DSM3400

3.2 Simulation of the Atmospheric Boundary Layer

In the wind tunnel, it is necessary to accurately reproduce the atmospheric boundary layer flow characteristics and ensure credible results. Namely the flow field in the wind tunnel tests should be similar with the atmospheric boundary layer wind flow in the outside world. Its wind speed and turbulence intensity vary with the height. And there are some certain requirements for fluctuating wind power spectrum.

3.2.1 The mean wind profile

Below the gradient wind lever, because of the friction near the ground, near-Earth wind speed decreases with the decrease of its height above the ground. The relation between the average wind speed and the height is described as the velocity profile curve. Usually logarithmic and exponential functions are adopted to describe the curve rule. In this paper, exponential law is used as the following formula (2).

$$\frac{U_{(Z)}}{U_r} = (\frac{Z}{Z_r})^{\alpha} \tag{2}$$

Where $U_{(Z)}$ represents the average wind speed at arbitrary height, Z represents the height, $U_{(r)}$ represents the average wind speed at the standard reference height, $Z_{(r)}$ represents the reference height, α represents the surface roughness index, the structure is situated at a Class B landform and its index value is 0.15.

3.2.2 Turbulent intensity

Turbulence intensity at arbitrary height is expressed as equation (3)

$$I_z = \sigma_u(z) / U(z) \tag{3}$$

Turbulence intensity decreases with the increase of the height, usually 20%~30% close to the ground. Chinese specification has no requirement for this at present and the Japanese specification gives specific recommendations about the turbulence intensity.

3.2.3 The power spectral density function

Atmospheric turbulence is a random and fluctuating process. The power spectral density function of fluctuating wind velocity is an important parameter to describe the wind field. At present the power spectrums of Davenport, Karman and Kaimal are frequently used in analysis.

1) Davenport spectrum (based on the Canadian specification NBC and Chinese specification GBJ [16-19])

$$\frac{fS_u(f)}{\sigma_u^2} = \frac{4x^2}{6(1+x^2)^{4/3}} \tag{4}$$

Where $x = fL_u / \overline{U}_{10}$, f represents the frequency, L_u represents the turbulence integral scale, approximate to 200, and $\overline{U}_{10}$ represents the average wind speed at the height of 10m.

2) Karman spectrum (based on the Japanese specification AIJ)

$$\frac{fS_u(f)}{\sigma_u^2} = \frac{4x}{(1+70.8x^2)^{5/6}} \tag{5}$$

Where $x = fL_u / \overline{U}_{10}$.

3) Kaimal spectrum (based on the American specification ASCE)

$$\frac{fS_u(f)}{\sigma_u^2} = \frac{200x}{6(1+50x)^{5/3}} \tag{6}$$

Where $x = fz / U(z)$.

3.2.4 Wind field simulation

In this paper, passive technology is adopted for the simulation of atmospheric boundary layer in the wind tunnel. The concrete geomorphic type is realized with wedge, the bezel and the roughness, shown in Figure 10 a). The comparison between measured wind speed values and the theoretical spectrum spectral curve is shown in Figure 10 b). Its wind speed profile and the turbulence intensity profile are shown in Figure 10 c) and d) respectively. It obviously that the measured wind speed spectrum in the wind tunnel is the most close to theoretical Karman spectrum.

a) Passive simulation device

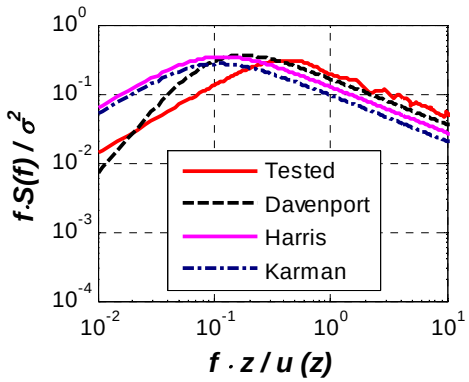

b) Comparison of measurement and theoretical value for wind speed spectrum

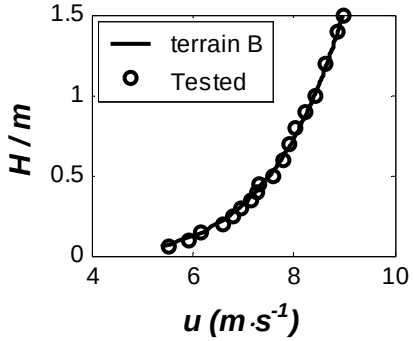

c) Wind profile

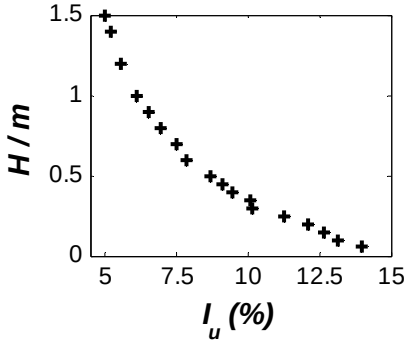

d) Turbulence intensity profile

Figure 10. Wind Tunnel Simulation for Terrain B of the Atmospheric Boundary Layer

3.3 Test Model and the Procedures Description

The test model is shown in the Figure 11. The pitch axis of the lower frame is 250mm high off the basement. A series of bolt holes are opened in the lateral and vertical steel pipe on the basis of angular relations to achieve the rotation of the reflector in the pitch direction by arm swing. After each rotation, the lateral and the vertical steel pipes are connected by the corresponding holes to maintain a balance as shown in Figure 12 and 13. In order to acquire not only adequate stiffness and strength of the model, but also facilitation in processing technology, the reflector surface adopts acrylic plexiglass plates. In view of the wind tunnel blockage ratio requirements, the geometry ratio of the model is 1/200. Model has a span of 550 mm and its ratio of rise to span is 1/4.8. Each acrylic plexiglass plate of two layers has a thickness of 5mm and the metal pressure tube has a length of 8mm. In light of the layout of the pipeline, the minimum interlayer thickness needs 10mm space and its size is shown in Figure 14. Convex and concave in the model are arranged by measurement points. Each side has 91 measurement points and these measuring points are shown in Figure 15.

a) Front view b) Perspective view

Figure 11. Experimental Model in the Wind Tunnel

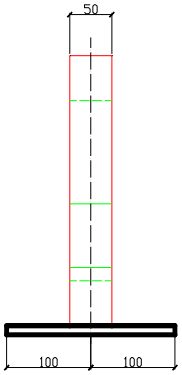

Figure 12. Front View of the Lower Bracket

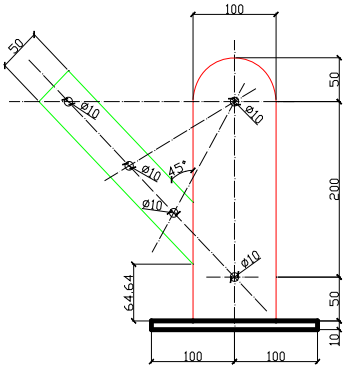

Figure 13. Side View of the Lower Bracket

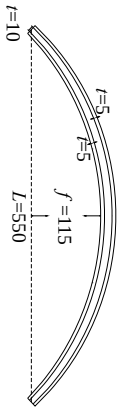

Figure 14. Reflector Section Plan of the Test Model

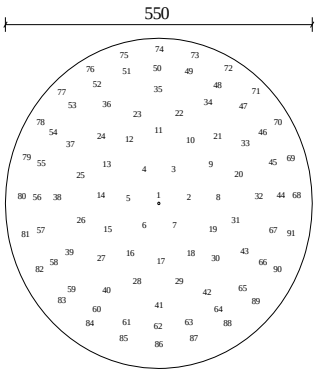

Figure 15. Pressure Tap Arrangement

3.4 Similarity Ratio Design

The wind speed in the tunnel is 14m/s and the test speed ratio is 1:4. The signal sampling frequency of the pressure valve is 625Hz and the sampling duration is 20s. Each individual measurement point collects 12500 times for the data as a sample, five samples in total. According to the similarity theory, the equation 7 shows the relation between the real structure and the test model.

$$n_m L_m / U_m = n_p L_p / U_p \tag{7}$$

Where n represents the frequency, L represents the geometry size, U represents the wind speed. The subscript m represents the model and p stands for the prototype. It can be obtained from the above equation that $n_m = 150$ Hz. Based on the Naikuitesi sampling criteria, the minimum sampling frequency in the experimental is 150Hz × 2 = 300Hz. It can be concluded that the test sampling frequency 625Hz meets the requirements. The similarity ratios of the rest relevant variables are shown in Table 4. In order to obtain reliable experimental data, the final time course of the wind pressure is the average of many samplings.

Table 4. Scaling Laws for Wind Tunnel Tests

Clause	Model data	Prototype data	Similarity ratio
Diameter	550mm	110m	1:200
Velocity	14m/s	56m/s	1:4
Time	20s	16.6min	1:50

The wind pressure value of each measurement point is expressed as the dimensionless pressure coefficient according to the equation 8.

$$C_{pi}(t) = \frac{P_i(t) - P_\infty}{P_0 - P_\infty} \tag{8}$$

Where $C_{pi}(t)$ is the pressure coefficient at any hole of the model. $P_i(t)$ stands for the measured wind pressure of the structure surface. P_0 and P_∞ represent the average total pressure and the mean static pressure at the reference point respectively. Reference point is the highest point of the reflector surface. For wind-resistant design and comparison with the corresponding specifications, it is necessary to transfer the measured pressure coefficient into the shape factor. For example the relation between the shape factor μ_{si} and the average pressure coefficient is expressed as the following equation 9.

$$\mu_{si} = \overline{C}_{pi}\left(\frac{Z_r}{Z_i}\right)^{2\alpha} \tag{9}$$

Where Z_i represents the height of the measuring point, and Z_r represents the the height of the standard reference point.

3.5 Test Results

Based on the software MATLAB, the corresponding program and the average pressure data contour line drawing process are programmed. The collected process data is processed according to the equation 8. Then the average pressure data is used to make the contour line for all the test conditions as shown in Figure 18 to Figure 21. It can be seen from the figures that when the pitch angle is 5°and wind angle is within 90°, the reflector surface are completely under the positive pressure, and to the wind angle of 60°, the maximum pressure coefficient is 1.2. When the wind angle is 90°, the negative pressure zone begins to appear at the reflector surface and there is wind suction. When the wind angle is beyond 90 °, the reflector surface negative pressure area gradually expands. When the wind angle is 120°, the boundary between the positive and negative pressure zones appears at the centre of the reflector. Until wind angle is 180°, reflective surface is completely controlled by negative pressure. In addition, when pitch angle is 30°or 60°, contour lines of the pressure distribution are more intensive. It is concretely demonstrated by the edge of the reflector surface where pressure distribution gradient is more intense but the pressure gradient of central area is gentler. When the pitch angle is 90°and the wind angle is 0°, the reflector surface

pressure distribution shows a good symmetry and the maximum wind suction occurs at the windward edge. Along the flow direction, the absolute value of the negative coefficient gradually decreases until the positive pressure appears and gradually increases. Overall the positive pressure area of the reflector surface is bigger than the negative pressure area under the wind load. Nevertheless the negative area mainly focuses on the local region of the windward front of the reflector surface.

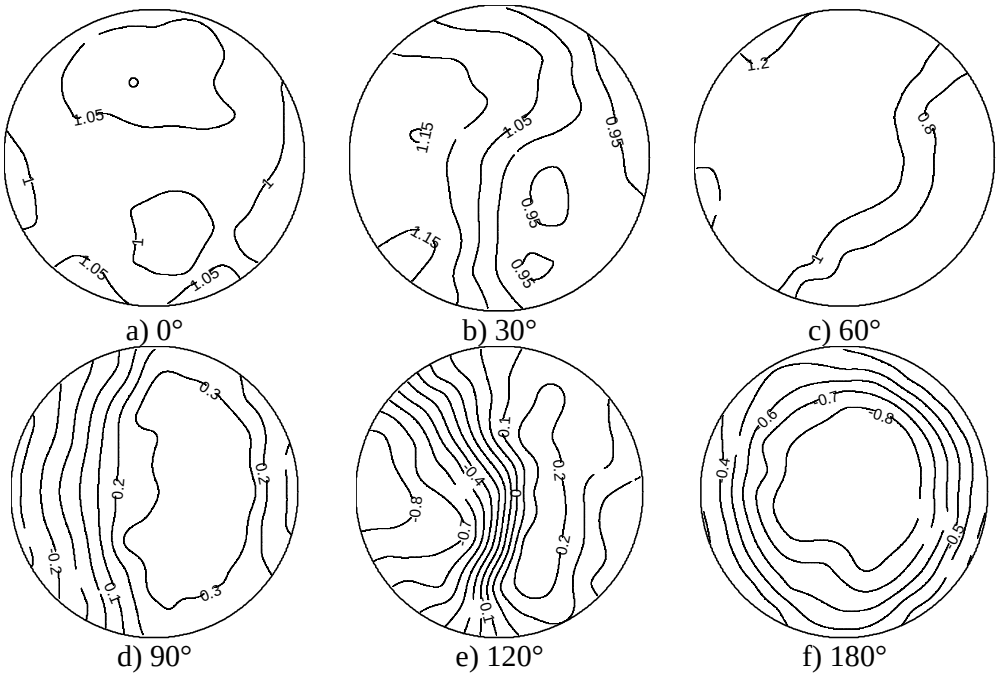

a) 0° b) 30° c) 60°

d) 90° e) 120° f) 180°

Figure 18. Mean Wind Pressure Coefficients of Reflector in Different Wind Directions for 0° Pitch Angle

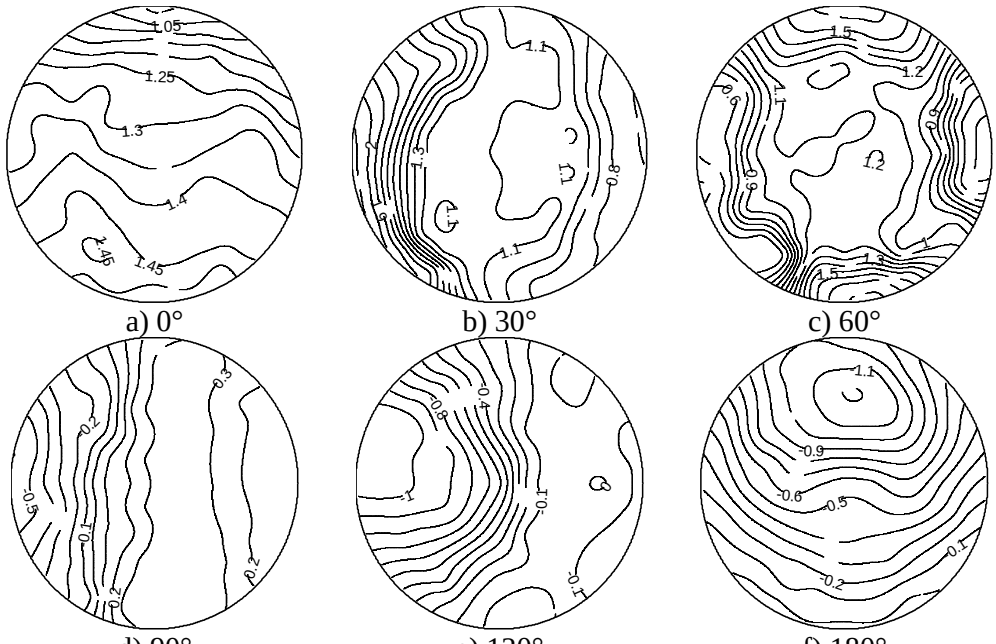

a) 0° b) 30° c) 60°

d) 90° e) 120° f) 180°

Figure 19. Mean Wind Pressure Coefficients of Reflector in Different Wind Directions for 30° Pitch Angle

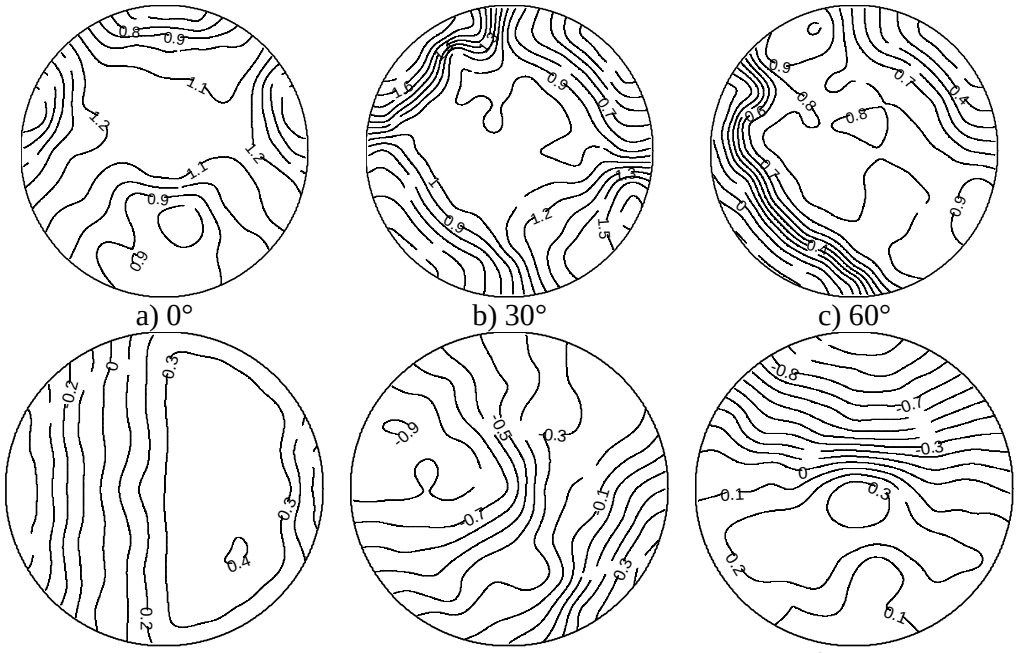

Figure 20. Mean Wind Pressure Coefficients of Reflector in Different Wind Directions for 60° Pitch Angle

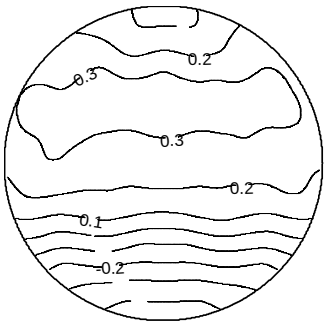

Figure 21. Mean Wind pressure Coefficients of Reflector for 90°Pitch Angle

3.6 Comparison between the Results from Simulation and the Test

In view of a great deal of test cases, so 0°, 90°, 180° in the range of wind angles are selected as typical cases to fully express the gradient variation of the average wind pressure coefficient (C_p) based on the direction of incoming flow as the symmetrical axis. Figure 22~24 give the comparison of the average wind pressure coefficient between the simulation and the wind tunnel tests. On the whole, under the wind angle 0°, the simulation generally seems to underestimate the pressure coefficients compared to the experimental results. The differences between two approaches are larger than that of two other wind angles. This is mainly under such wind angle, the pressure gradient is so great (wind pressure coefficient varies severely) in the local edge region of the reflector back. This character leads to the difference between the numerical simulation and the test is larger than other wind angles for different pitch angles models, and the contrast effect is not very ideal. As for the wind angle 90° and 180°, simulation results are slight larger than that of the experiments but then most data are well consonant. This is mainly because the position of separating points for airflow with the wall surface changes significantly which leads to a different wake effect. Specifically for the wind angle 90°, the differences between simulation and test are almost within 8% and the maximal difference for some individual point reaches 57% which appears at the pitch angle 30° model. For the wind angle 180°, at each pitch angle model, there are only

some single points (just one or two) having the maximal difference which could reaches beyond 50%, but almost the differences from all the data are within 10%. On balance, the results show that the distributions from two research methods above tend to be almost parallel and the data values are well consonant. The results of numerical simulation are well verified by the wind tunnel test. This shows that CFD is a practical and effective method to carry out the wind characteristics analysis to parabolic reflector of the antenna structure.

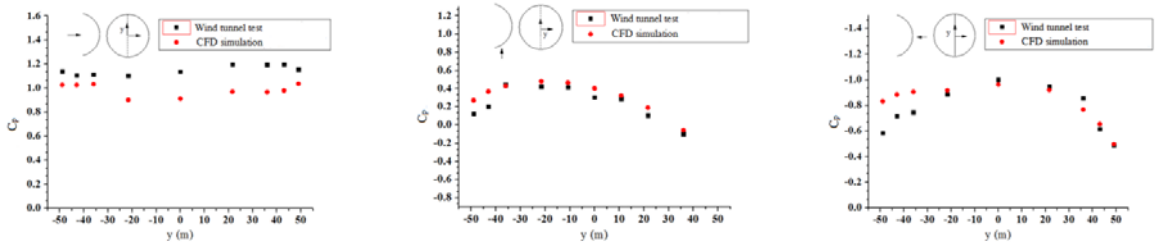

a) 0°wind angle b) 90°wind angle c) 180°wind angle

Figure 22. Comparison between Numerical Simulated and Test Results on Reflector at 5°Pitch Angle

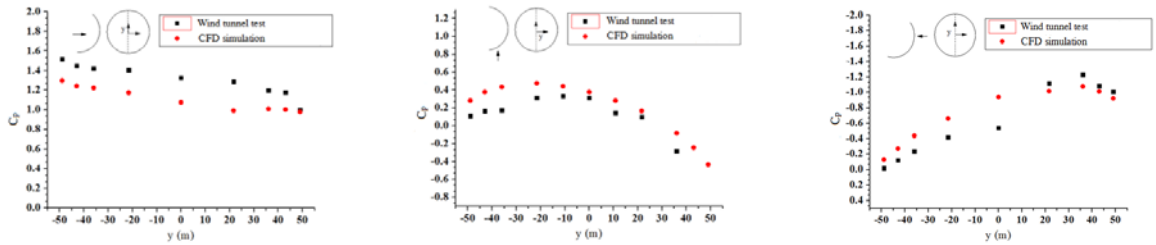

a) 0°wind angle b) 90°wind angle c) 180°wind angle

Figure 23. Comparison between Numerical Simulated and Test Results on Reflector at 30°Pitch Angle

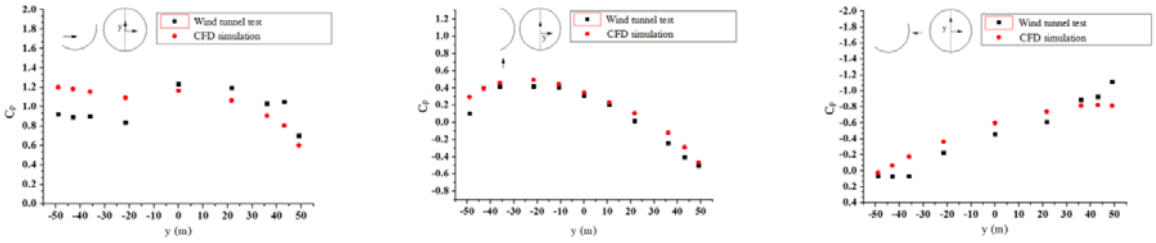

a) 0°wind angle b) 90°wind angle c) 180°wind angle

Figure 24. Comparison between Numerical Simulated and Test Results on Reflector at 60°Pitch Angle

4. SHAPE FACTOR OF THE REFLECTOR SURFACE

Based on the research findings in numerical simulation and wind tunnel test, here in order to acquire the precise wind load for the design of the back frame structure, aiming at different types of reflectors it is necessary to make a partition on the reflector surface and provide the shape factor corresponding with each divided region.

In partition, thanks to the symmetry of the reflector structure, so reflector surface is divided along the ring direction and radial direction according to the formation law of the reflector. Simultaneously in the light of the average wind pressure distribution, the wind pressure gradient of the edge region is large whereas that of the region near the center is relatively flat. So outer ring region is divided densely and inner ring region is divided sparsely. The concrete partition is shown in Figure 25.

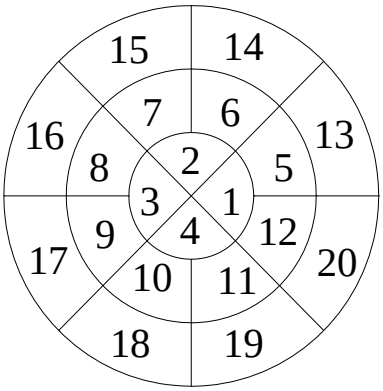

Figure 25. Regional Division of the Telescope Surface

In general, all-movable antenna structures could be classified according to its aperture diameter. The diameters within 50m belong to the intermediate region of size and above 100m belong to the large span. At present, all-movable antennae within 50m are widely distributed throughout the world and the relevant research results constitute a rich harvest. There are about 10 all-movable antennae more or less distributed around the world. Above 100m there are only two respectively in the United States and Germany. So on the basis of the current situation, the apertures of 65m and 90m are selected as illustrating analysis examples in the intermediate region of size meanwhile the aperture of 110m is selected as illustrating analysis example in the large span region of size. In addition two kinds of focal length to diameter ratios (0.3 and 0.5 shown in Figure 26) combined with different aperture diameters above are selected as numerical examples to analyze wind field the characteristics by CFD simulation. The obtained mean wind pressure in each node could be calculated and converted into corresponding shape factor according to the formula (9). Finally shape factor for each divided region could be acquired based on the partition in Figure 25 and all computational results are summed up to be shown in Figure 27~32. Based on these 6 figures the shape factor of the reflector surface can be directly found with regard to different diameters, focal length to diameter ratios, pitch angles and wind directions for antenna structures design in the future.

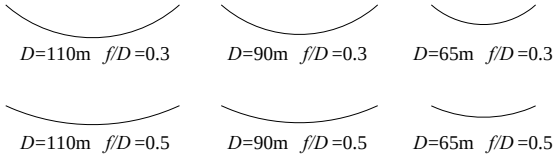

Figure 26. Different Reflector Surfaces

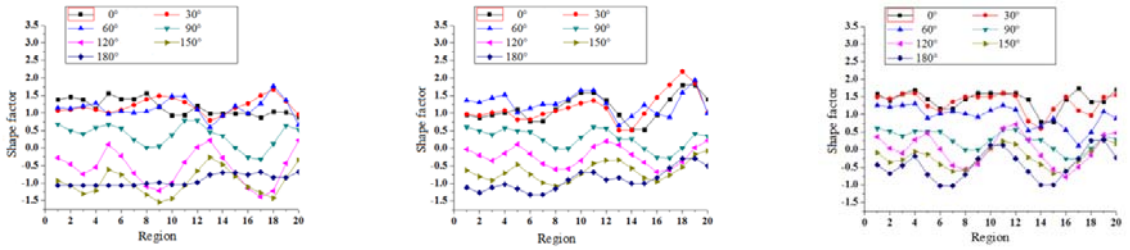

a) 5° b) 30° c) 60°

Figure 27. Shape Factor of Wind Load at Different Pitch Angle for 110m Aperture Reflector（*F*/*D*=0.3）

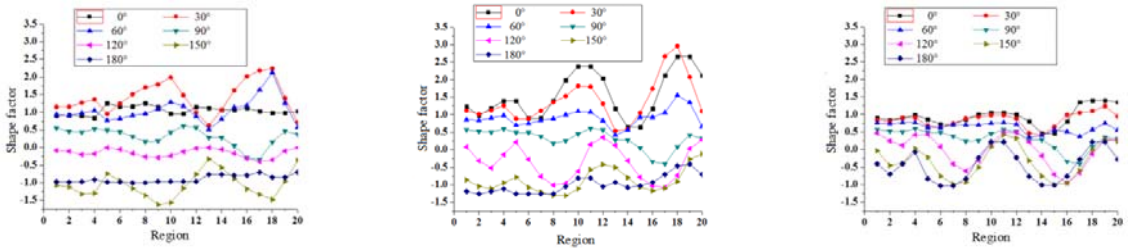

a) 5° b) 30° c) 60°

Figure 28. Shape Factor of Wind Load at Different Pitch Angle for 110m Aperture Reflector（*F*/*D*=0.5）

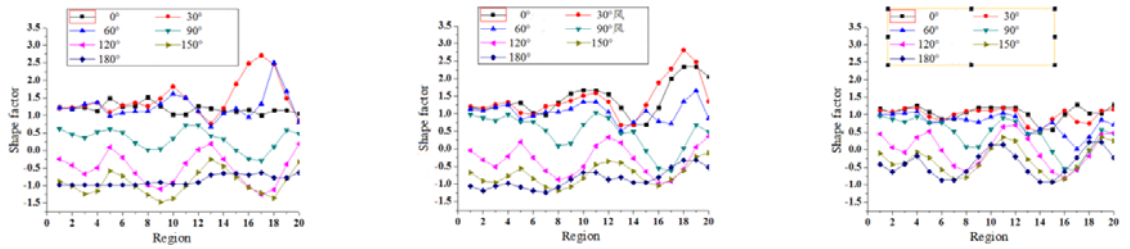

a) 5° b) 30° c) 60°

Figure 29. Shape Factor of Wind Load at Different Pitch Angle for 90m Aperture Reflector（*F*/*D*=0.3）

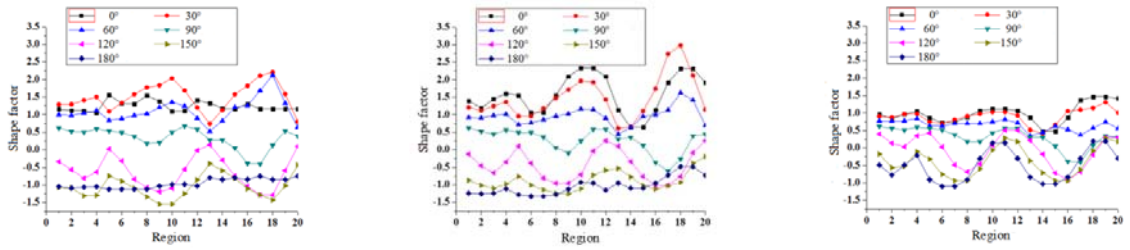

a) 5° b) 30° c) 60°

Figure 30. Shape Factor of Wind Load at Different Pitch Angle for 90m Aperture Reflector（*F*/*D*=0.5）

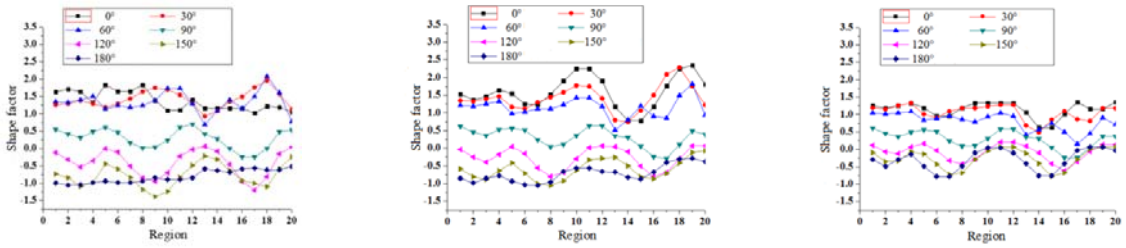

a) 5° b) 30° c) 60°

Figure 31. Shape Factor of Wind Load at Different Pitch Angle for 65m Aperture Reflector（*F*/*D*=0.3）

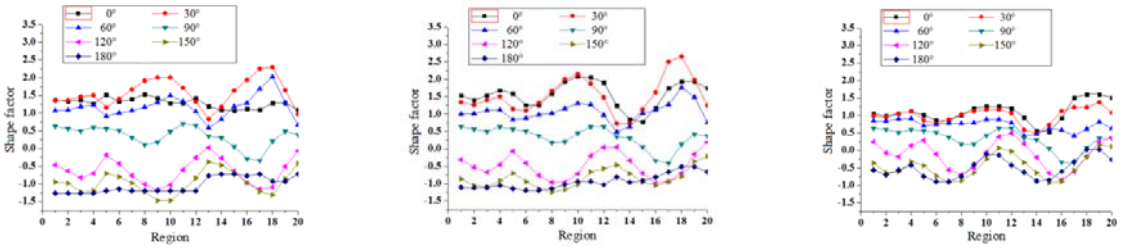

a) 5° b) 30° c) 60°

Figure 32. Shape Factor of Wind Load at Different Pitch Angle for 65m Aperture Reflector（*F*/*D*=0.5）

5. WIND INDUCED VIBRATION RESPONSE

The reflector structure of the antenna is a typical large span structure which is not appropriate to use quasi steady assumption under the complex wind load, so it is difficult to estimate the dynamic effect of fluctuating wind. The antenna structure is respectably sensitive to the fluctuating wind in view of its longer natural vibration period and weaker stiffness. Besides dynamic response characteristics for this open type of reflector structure under the fluctuating wind so that it is necessary to furtherly make a dynamic response analysis for the antenna structure based on the time course of wind pressure from the wind tunnel test and probe into the wind induced vibration response of this kind of structure under different pitch angles proposed above.

The time course of wind pressure obtained from the wind tunnel test is determined according to the similarity ratio relationship between the real structure and the test model, shown in the formula (10).

$$(fL/U)_m = (fL/U)_p \tag{10}$$

Where, f represents the frequency, L represents the geometry size, U represents the wind velocity, the subscript m represents test model and p represents the real structure. In the wind tunnel test, sampling frequency is 625Hz, geometric scaling ratio is 1:200, and the wind speed at the height of gradient wind is 14m/s (corresponding to the 56m/s at the actual height of 350m). The basic pressure for the period of 100 years at Qitai County is 0.7kN/m^2.

5.1 Self Vibration Characteristics Analysis

The natural frequency is an important parameter to analyze the dynamic response of the structures. In this work the self vibration characteristics are analyzed by subspace iteration method for 4 kinds of typical pitch angles combined with the wind tunnel test. Here taking the model of 90° pitch angle as an example, from the first 10 order natural frequencies shown in the Table 5, it can be seen that the frequency distribution of the antenna structure is dense, the frequency of each adjacent mode is very close, the fundamental frequency is low and the structure is more flexible. Due to limited space, Figure 33 gives only first two order modes from which it could be seen that the first order mode is mainly expressed as the rotation of the back frame and the pitching mechanism around the pitch axis, and the second order mode is mainly expressed as the translation of the back frame along the pitch axis with respect to the azimuth pedestal. The remaining modes are mainly expressed as local vibration or torsion of the structure.

Table 5. Ten Order Frequencies of the Telescope Structure

Order	1	2	3	4	5	6	7	8	9	10
Frequency	0.887	1.032	1.158	1.214	1.358	1.545	1.681	1.843	1.972	2.125

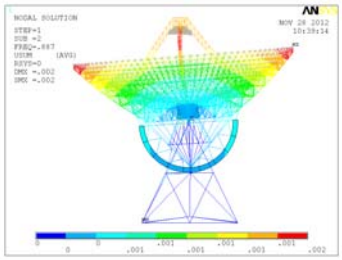

a) The first order

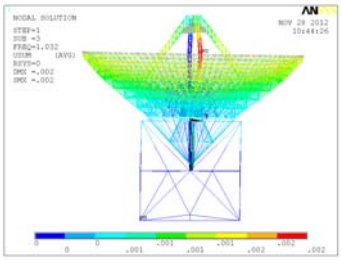

b) The second order

Figure 33. The Mode of Structure Vibration

5.2 Analysis Method

The antenna structure is analyzed for the wind-induced response by using nonlinear time-history analysis method. The structure is discretized by using the finite element method and the wind loads are exerted on the corresponding nodes. The structure response is obtained by directly solving the equations of structure motion in the time domain. The calculating results of this method are more realistic than the linear approach in the frequency domain. It could be applied to any system and any incentive in principle. And the more complete information about the whole process of structural dynamic response could be got. It is the effective way to analyze the wind induced dynamic response of the antenna structure.

5.2.1 Wind vibration factor of the displacement and stress

According to the specification, the dynamic effects of wind load are taken as the static load in the form of wind-induced vibration coefficient. Namely the wind pulse is expressed as the equation 11

$$\beta = \frac{P_e}{\overline{P}} = \frac{\overline{P} + P_d}{\overline{P}} = 1 + \frac{P_d}{\overline{P}} \tag{11}$$

Where β is the wind pulse, P_e is the equivalent static wind load, $\overline{P}$ is the static wind load, P_d is the dynamic wind load.

For the time-history analysis for wind-induced vibration of the complex spatial structure using finite element method, the wind pulse directly bases on the structure response. Namely the wind vibration factor of the displacement and internal force are expressed as the equation 12.

$$\beta = \frac{D_y}{\overline{D}_y} \tag{12}$$

The above equation $\overline{D}_y$ represents the structural response under the static wind loads, including structural displacement responses and stress responses. D_y represents the total extreme wind-induced vibration response of the structure, including static and dynamic response. The relation between them is expressed as the equation 13.

$$D_y = \overline{D}_y \pm g \cdot sign(\overline{D}_y)\sigma_y \tag{13}$$

Among them, $sign$ is a sign function, σ_y is the mean square error of the response for fluctuating wind. g is the peak factor and its value is related with the number of times during which the effect is beyond the average load effect in an average hour. When the probability distribution of the average load effect is normal distribution, g can be expressed according to the equation (14). Where T is the observation time (typically 1 hour), v is the horizontal crossing number, which is in the range from 3.0 to 4.0, and 3.5 is selected in this paper.

$$g = \sqrt{2\ln vT} + 0.577 / \sqrt{2\ln vT} \tag{14}$$

5.2.2 Whole wind pulse

The wind pulse of the displacement in each point and of the stress for each element could be obtained according to the equation 15. But for the large span structure, because the spectrum has the intensive modes and the mode contributing a lot may not appear in the first vibration mode, so it is difficult to determine which mode has the significant effect on wind-induced vibration response. In this paper, the wind pulse of the overall displacement and stress based on the maximum dynamic response is used and expressed as the following equation 16.

$$\beta_d^* = \frac{\{\beta_{di} \times U_{wi}\}}{\{U_{wi}\}_{\max}} \tag{15}$$

$$\beta_s^* = \frac{\{\beta_{si} \times S_{wi}\}}{\{S_{wi}\}_{\max}} \tag{16}$$

Where $\{U_{wi}\}$ and $\{\beta_{di} \times U_{wi}\}$ are the maximum nodal displacement and time-history displacement respectively under the static wind loads and the total wind loads. Where $\{S_{wi}\}$ and $\{\beta_{si} \times S_{wi}\}$ are the maximum element stress and time-history element stress respectively under the static wind loads and the total wind loads.

5.3 Vibration Response Results Analysis

5.3.1 Analysis scheme and response index

According to the wind tunnel test results, the overall drag coefficients of the antenna structure under 3 kinds of pitch attitudes are shown in Figure 34, and no matter what pitch angle, the resistance coefficient of 0°wind angle reaches the maximum value. So the wind angle of 0° is selected as the analysis condition for wind-induced vibration response analysis respectively under the pitch angle of 5°, 30°, 60°. Combined with the characteristics of the large span structure and the wind-induced vibration response concerned by the design staff, the normal displacement of each node on the reflector and axial stress + bending stress of the element are used as the indicators of the wind-induced vibration response.

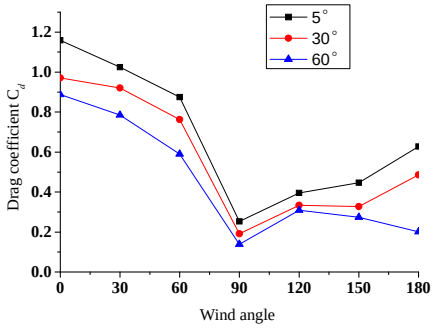

Figure 34. C_d in Different Directions

5.3.2 Results analysis of wind induced vibration response

Extreme stress and extreme displacement in time-history for the 3 models are shown in Figure 35 and Figure 37. In order to analyze the response characteristics under the fluctuating wind loads in the frequency domain, Fourier transformation is used to convert the response process from the time domain to the frequency domain. The corresponding extreme stress and displacement power spectral density function are shown in Figure 36 and Figure 38. According to the power spectral density function, it can be seen that the wind induced vibration response of the structure is a narrowband process. For the same pitch angle model, the dynamic response from the extreme stress and extreme displacement power spectrum are highly consistent. Combined with the aforementioned natural frequencies of the structure, for the 5°pitch angle, it is shown that the vibration energy concentrated near the first order frequency (0.7Hz) nearby. For the 30° pitch angle, it is still shown that the vibration energy concentrated in the first-order frequency (0.7Hz) nearby, nevertheless the amplitude of energy has increased. For the 60°pitch angle, the higher modes (the third order and the forth order) begin to contribute to the performance of the vibration energy of the structure and from the energy distribution that the peak appear at the frequency of 0.9Hz and 1.1Hz. What's more, the relation between the energy magnitude and the pitch angle shows that the vibration energy increases gradually with the increase of the pitch angle. Later the extreme stress distribution and the displacement distribution of the model are given respectively in Figure 39 and Figure 40. It can be seen in the extreme stress distribution under the wind angle of 0°, the largest stress reaching 170MPa mainly concentrated in the radius element on the second ring of the upper chord and this condition appears in the model of pitch angle of 30°. It also can be seen from the normal displacement that under the wind angle of 0°, the displacement shows the symmetry along the vertical axis and the extreme displacements of each model appear at the overhangying end and two sides of the reflector surface. In 3 models, the maximal normal displacement is up to 24cm and appears in the 5°pitch angle attitude. Due to space limitations, the calculation results of other models for different pitch angles are shown in Table 6. According to the time-history analysis

results, the extreme response for each pitch angle of the antenna structure is determined while the wind pulse for wind force proofing design in the future are provided in Table 6.

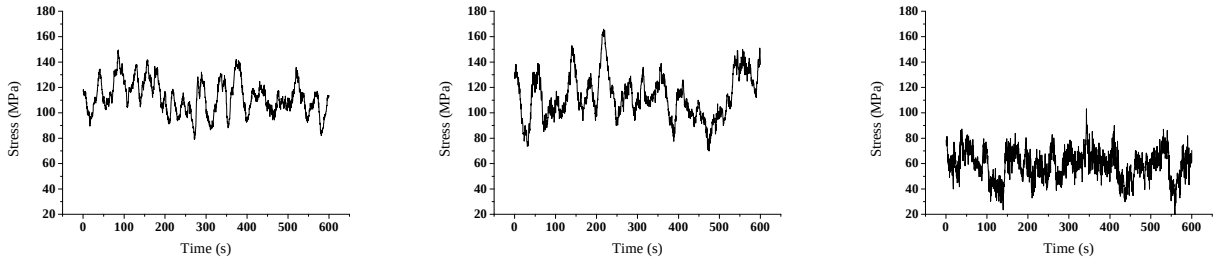

a) 5° b) 30° c) 60°

Figure 35. Time-history of the Extreme Stress for Different Kinds of Pitch Angle Models

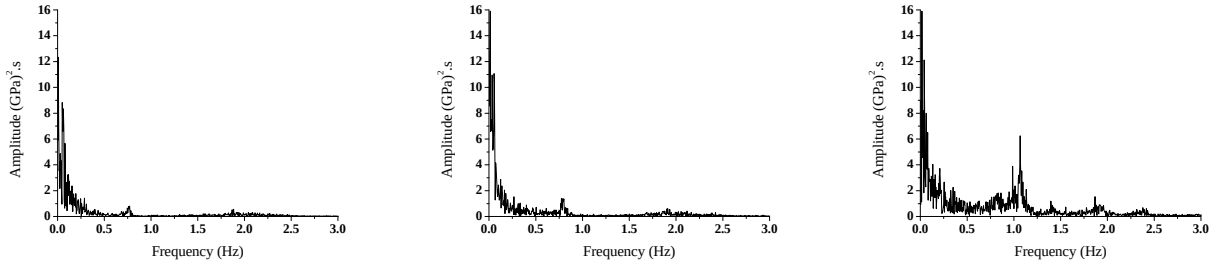

a) 5° b) 30° c) 60°

Figure 36. Power Spectral of the Extreme Stress for Different Kinds of Pitch Angle Models

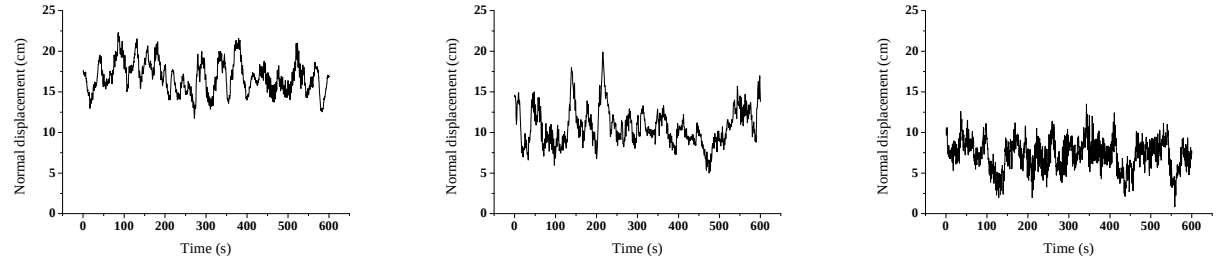

a) 5° b) 30° c) 60°

Figure 37. Time-history of the Extreme Displacement for Different Kinds of Pitch Angle Models

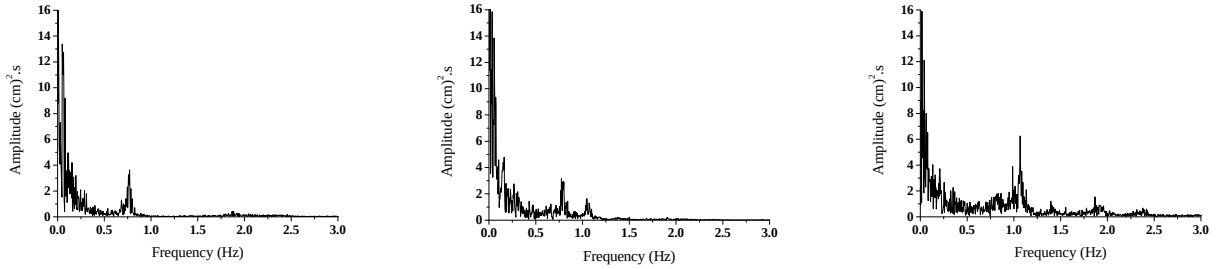

a) 5° b) 30° c) 60°

Figure 38. Power Spectral of the Extreme Displacement for Different Kinds of Pitch Angle Models

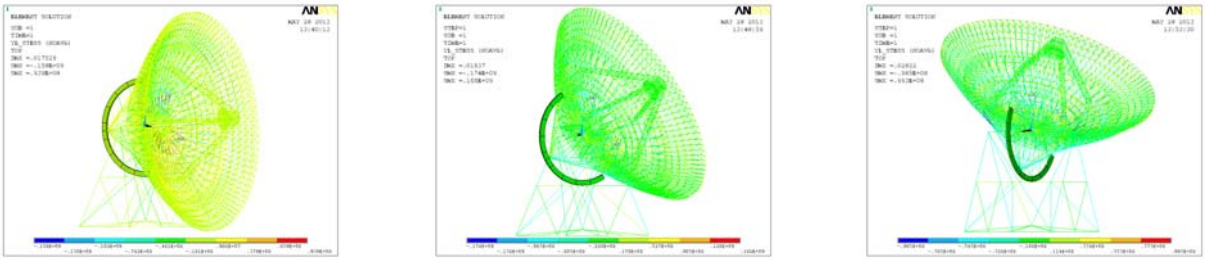

a) 5° b) 30° c) 60°

Figure 39. Extreme Value Distribution of Stress for Different Kinds of Pitch Angle Models

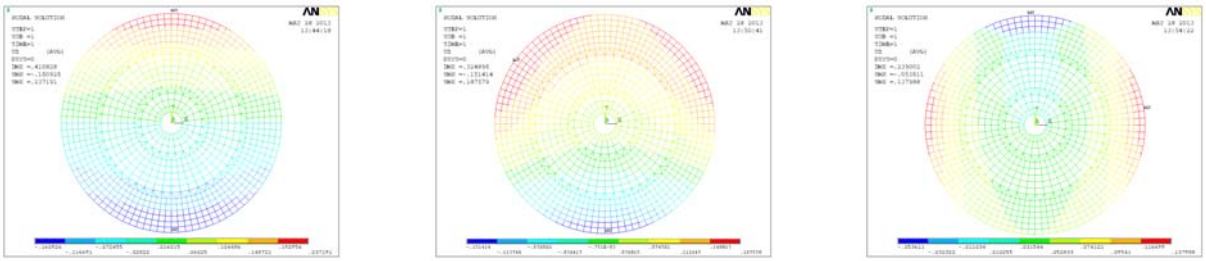

a) 5° b) 30° c) 60°

Figure 40. Extreme Value Distribution of Displacement for Different Kinds of Pitch Angle Models

Table 6. Extreme Response and Wind Vibration Factors of the Structure at Different Pitch Angles

Pitch angle	5°	30°	60°	90°
Maximum displacement	24cm	19cm	14cm	22cm
Maximum stress	158MPa	174MPa	99MPa	152MPa
Whole wind pulse of the displacement	2.37	1.73	1.82	1.92
Whole wind pulse of the stress	1.41	1.54	1.57	2.18

5.3.3 Comment on the nonlinear response of the structure

According to the analysis of the structural extreme response and power spectral, it can be seen that nonlinear response of the all-movable antenna structure is mainly influenced by the upwind attitudes, and vibration factors are different for different models and structural responses. They are embodied specifically in the followings.

(1) Although the all-movable antenna structure belongs to such kind of rigid structure, its reflector part has a large span up to one hundred meters more or less resulting in that the structure becomes more flexible (this can be inferred by self vibration characteristics analysis). So the effect from fluctuating wind could not be neglected in the wind force proofing design and the first four modes of vibration contribute a lot to wind-induced vibration of the whole structure.

(2) From the vibration response results, the whole wind pulse of the displacement is larger than the whole wind pulse of the stress, especially under the pitch angle 5°, because the reflector is almost under the complete upwind state and the top displacement should be focus on. Moreover, although under the pitch angle 5°, the extreme stress is 158MPa larger than 152MPa under the pitch angle 90°, the whole wind pulse of stress is 1.41 smaller than 2.18 under the pitch angle 90°. This can be inferred that under the pitch angle 5°, static wind load contribute more than that under the pitch angle 90°. For the model of pitch angle 90°, because wind direction is vertical to the central axis of the reflector, airflow could be separated on the front edge of the reflector and adhere to the end

edge again. This phenomenon could form the vortex shedding and severe fluctuating pressure leading to the larger wind pulse.

(3) Under the most unfavorable wind angle 0°, the pitch angles for 5° and 90° are two kinds of unfavorable working states because they correspond to the maximal wind pulses of the displacement and the stress respectively. Combined with the wind angle and pitch angle, according to the worst upwind attitude, wind pulses could be determined for the all-movable antenna structure in its whole performance. The whole wind pulse of the displacement could be set as 2.5 and 2.2 could be proper for the stress.

6. STRUCTURAL ANALYSIS UNDER THE DESIGNED WIND LOAD

6.1 Mechanical Analysis under the Survival Wind Speed

Table 7. Static Combination Conditions

	Combination	Gravity coefficient	Snow load coefficient	Wind load coefficient
1	Gravity	1.2x1.0	/	/
2	Gravity+wind load 1	1.2x1.0	/	1.4x1.0
3	Gravity+wind load 2	1.2x1.0	/	1.4x1.0
4	Gravity+wind load 3	1.2x1.0	/	1.4x1.0
5	Gravity+snow load	1.2x1.0	1.4x1.0	/
6	Gravity+snow load+wind load 1	1.2x1.0	1.4x0.7	1.4x1.0
7	Gravity+snow load+wind load 2	1.2x1.0	1.4x0.7	1.4x1.0
8	Gravity+snow load+wind load 3	1.2x1.0	1.4x0.7	1.4x1.0

For the large antenna structure the member should meet the strength requirement and the deformation need to be limited in the allowable range without collapse under the survival wind U=40m/s. Here the 110m antenna structure is selected as a typical object to make the strength and stability analysis under self weight combined with wind load and snow load.

According to the Load Code for the Design of Building Structure combined with the actual environment the antenna structure exists in, the antenna structure is analyzed under the load combination. The load combination is shown in Table 7 and the snow load is considered only for the model of pitch angle 5°. Wind load 1, 2, 3, represent 0°, 90°, 180°respectively and wind pulse is determined according to the table 6 coming from the wind vibration response analysis. Taking the models of pitch angle 5°, 30°, 60°, 90°, strength and stability analysis is carried on according to the procedures shown in Figure 41. Due to the limited space, only the results from the model of pitch angle 5° are given in Figure 42~46 and the results for other models are generalized in Table 8. These achievements show that under all of the load combinations, the whole structure is in the elastic state, the vast majority of members are in the low stress level within 100MPa and the maximum deformation is only 128mm. The value of stress and deformation all meet the relevant specification requirements and the structure is safe.

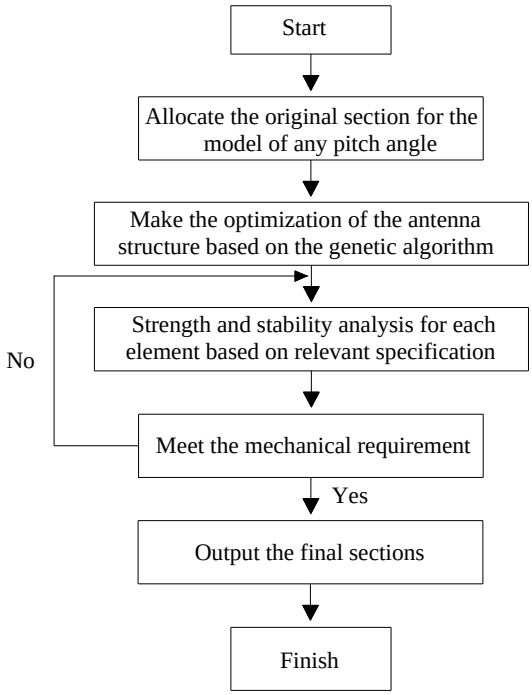

Figure 41. Flowchart of Member Mechanical Performance for the Telescope Structure

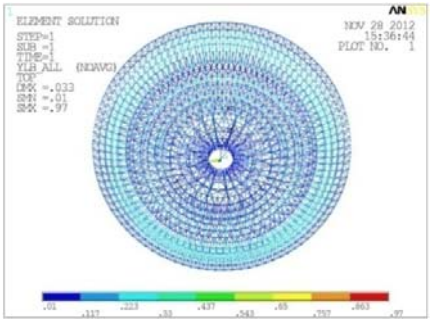

Figure 42. Stress Ratio of Back Frame Structure

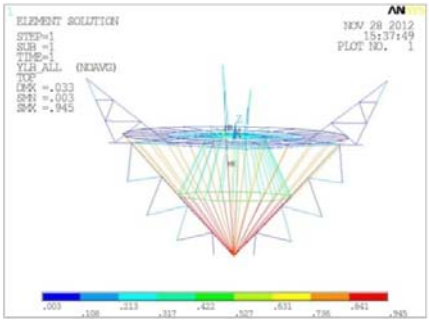

Figure 43. Stress Ratio of Pitch Mechanism

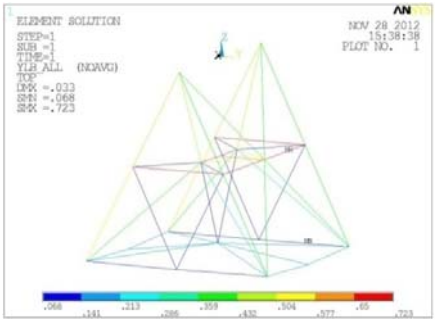

Figure 44. Stress Ratio of Azimuth Holder

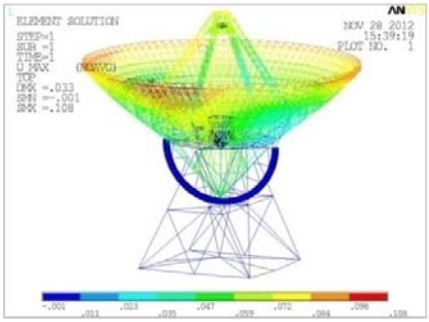

Figure 45. Displacement of the Whole Structure

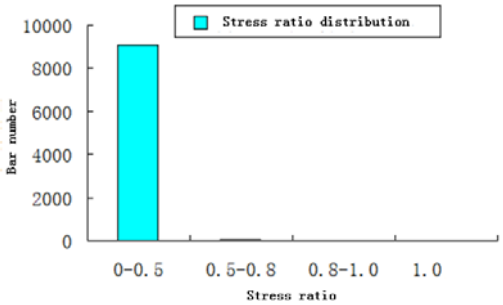

Figure 46. Bar Chart of Stress Ratio for Back Frame Structure

Table 8. Calculating Results of Static Combination Conditions

Pitch angle	Structural response	Back frame	Pitch mechanism	Azimuth mount
	Maximum stress ratio	0.92	0.77	0.75
5°	Overrun component	None	None	None
	Maximum displacement		128mm	
	Maximum stress ratio	0.99	0.97	0.67
30°	Overrun component	None	None	None
	Maximum displacement		120mm	
	Maximum stress ratio	0.96	0.94	0.62
60°	Overrun component	None	None	None
	Maximum displacement		114mm	
	Maximum stress ratio	0.97	0.95	0.72
90°	Overrun component		None	None
	Maximum displacement		108mm	

6.2 Performance Analysis under the Working Wind Speed

The antenna structure is required to have a good performance under the working speed U=20m/s. That is to say the antenna could still trace the celestial objects and complete the observation mission after the wind deformation is adjusted by the actuators. So it is necessary to make the reflector surface precision analysis under the wind load. Taking the wind angle of 0°as the typical example, the Figure 47~48 give the surface precision RMS and the whole structure displacements for different pitch angles. The surface precision under other wind angles are all given in Table 9 only in the form of data.

6.2.1 Reflector surface precision analysis under the wind load

From view of the displacement of the structure, the distribution of the surface deformation is not uniform. For examples, the model of 5° pitch angle, 0°wind angle has the maximum displacement on the top and the minimum displacement at the bottom, and the maximum difference reaches 38mm. The model of 60° pitch angle, 0°wind angle has the maximum displacement at the bottom and the minimum value at the center, and the maximum difference reaches 32mm. For the model of 90° pitch angle, 0°wind angle, the maximum displacement appear in the upwind front and thanks to the reflector geometry, in the center of the reflector the displacement reaches the minimum value. These present results are caused by the reflector structure characteristics. In bearing parts of the reflector structure are similar to that of the cantilever roof. With moving on to the inner ring region, the distance to the support region of the reflector structure is much shorter accompanied by the thicker grid height. So the two factors above result in a better stiffness and the displacement naturally decreases in the region near the center of the reflector. Simultaneously combined with the results in section 2~3, near the edge of the reflector extreme wind pressure often appears and the

pressure gradient is more intense. By contraries, near the center zone of the reflector, the wind pressure gradient is gentler and the stress is naturally more uniform. So in view of the stress condition and the stiffness distribution of the reflector structure, it is inevitable that the reflector surface deforms unevenly and has an undesirable precision.

Table 9. RMS of Reflector Surface under the Wind Load

Pitch angle \ Wind angle	0°	90°	180°
5°	0.362	2.092	0.212
30°	2.206	1.715	0.377
60°	2.102	1.785	0.586
90°	2.096	2.092	2.103

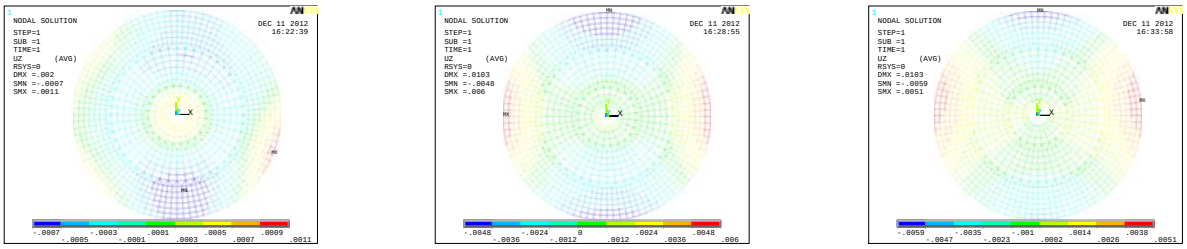

a) 5° b) 60° c) 90°

Figure 47. Half Optical Path Error of Reflector Surface

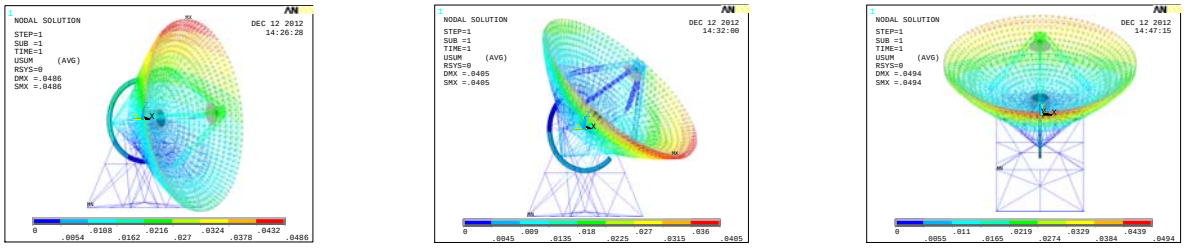

a) 5° b) 60° c) 90°

Figure 48. Whole Displacement of the Structure

6.2.2 Surface precision analysis for different models under different load cases

In the actual operations, it is necessary to calculate the influence of not only single load but also the combination of different loads because the gravity load coexists with the wind load, and pay special attention to the leading factor. Table 10 gives the reflector surface precision under different load cases. Limitations of space allows for the results of 0° wind angle if wind load joins in the combination.

From the table above it is obviously that the wind load has a greater effect than gravity load on the reflector surface precision. On the one hand, the structure is more flexible and sensitive to the wind load with the increase of the aperture diameter. Compared with gravity load wind load has a more serious effect and plays a leading role. On the other hand, in the antenna structure scheme approachment, the lectotype and the optimization mainly consider the gravity load that is to say the back frame structure style is determined and the section of each pipe is optimized under the gravity load effect. So in order to realize a high reflector surface precision the back frame structure obtains a reasonable stiffness distribution in such a scheme determination course. Namely some part has more weights, more stiffness will appear, vice versa. But from the deformation under the wind load

shown in Figure 48, the stress caused by wind load could not fit with the structure stiffness so the deformation heterogeneity caused by wind load is more seriously than that of the gravity load which results in a lower surface precision under the single wind load or the combination the wind load joins in.

Table 10. Surface Precision on Main Reflector under Each Working Condition (RMS)

Gravity effect				
Pitch angle	5°	30°	60°	90°
Surface precision	0.306mm	0.223mm	0.143mm	0.306mm
Wind load effect				
Wind velocity	20m/s			
Pitch angle	5°	30°	60°	90°
Surface precision	0.362mm	2.206mm	2.102mm	2.096mm
Effect of the combination of gravity and wind load				
Wind velocity	20m/s			
Pitch angle	5°	30°	60°	90°
Surface precision	0.175mm	2.265mm	2.342mm	2.259mm

7. CONCLUSIONS

The widely used parabolic reflector (F/D=0.3) is selected as an analysis point of penetration to carry out the numerical simulation for its 22 kinds of gestures. Subsequently, the manometry tests are carried out in the wind tunnel for the working conditions above. The wind tunnel test validates the numerical simulation very well in wind characteristics analysis of parabolic reflector structures by comparisons.

- For most of models with different pitch angles and wind angles, the maximum negative pressure generally appear in the edge region because the incoming flow usually separates significantly at this location. For the model of the same pitch angle at different wind angles, extreme value of the average surface pressure appear at different surface position due to the differences of the separation points position on the wall and the wake effect. In view of the CFD simulation validity for parabolic antenna structure verified by the wind tunnel test, subsequently large scale computations and analysis of different types of reflectors structures are carried out by CFD and the shape factor for each corresponding type of reflector structure under different gestures. This achievement provides abundant wind force proofing design references for those parabolic antennae.
- According to the power spectrum density function it could be seen that the wind induced vibration response of the antenna is a narrow-band course. For the same pitch angle model, the maximum stress power spectrum and displacement power spectrum are highly consistent in the dynamic response of the structure. Although the all-movable antenna structure belongs to such kind of rigid structure, its reflector part has a large span up to one hundred meters more or less resulting in that the structure becomes more flexible. So the effect from fluctuating wind could not be neglected in the wind force proofing design and the first four modes of vibration contribute a lot to wind-induced vibration of the whole structure.
- Under the most unfavorable wind angle 0°, the pitch angles for 5° and 90° are two kinds of unfavorable working states because they correspond to the maximal wind pulses of the displacement and the stress respectively. Combined with the wind angle and pitch angle, according to the worst upwind attitude, wind pulses could be determined for the all-movable antenna structure in its whole performance. The whole wind pulse of the displacement could be set as 2.5 and 2.2 could be proper for the stress.

- Based on the average wind pressure distribution characteristics and the results of wind induced vibration response, the static wind loads and the corresponding wind vibration coefficient of the reflector are obtained. Taking 110m antenna structure (F/D=0.3) as an example, firstly the mechanical analysis under the survival wind speed is carried out and the results show that the whole structure is in the elastic state, the vast majority of members are in the low stress level and all kinds of responses meet the relevant specification requirements. Next, the performance analysis under the working wind speed is carried out. The results show that the antenna structure is more flexible and the wind load takes a leading role on the reflector surface precision.

ACKNOWLEDGEMENTS

This work was financially supported by the National Natural Science Foundation of China (Grant No. 51378149)

REFERENCES

[1] Marco, Quattri,, “Proceedings of the International Society for Optical Engineering”, Boston University Press, Boston, 2002, pp. 459-470.

[2] Hiriart, D., Ochoa, J.L. and Garcia, B., “Wind Power Spectrum Measured at the San pedro Martir Sierra”, Revista Mexicana de Astronomia Astrofisica, 2001, Vol. 37, pp. 213-220.

[3] Solari, G. and Piccardo, G., “Probabilistic 3-D Turbulence Modeling for Gust Buffeting of Structures”, Probabilistic Engineering Mechanics, 2001, Vol. 16, pp. 73-86.

[4] Jia, Y.Q., Sill, B.L. and Reinhold, T.A., “Effects of Surface Roughness Element Spacing on Boundary Layer Velocity Profile Parameters”, Wind Eng. Ind. Aerodyn, 1998, Vol. 73, pp. 215-230.

[5] Irwin, H.P.A.H., “The Design of Spires for Wind Simulation”, Wind Eng. Ind. Aerodyn, 1981, Vol. 8, pp. 361-366.

[6] Balendra, T., Shah, D.A. and Tey, K.L., “Evaluation of Flow Characteristics in the NUS-HDB Wind Tunnel”, Wind Eng. Ind. Aerodyn, 2002, Vol. 90, pp. 675-688.

[7] Meroney, Letchford and Sarkar., “Comparison of Numerical and Wind Tunnel Simulation of Wind Loads on Smooth and Dual Domes Immersed in a boundary Layer”, International Journal of Wind and Structures, 2002, Vol. 5, pp. 347-358.

[8] Uematsu, Y. and Tsuruishi, R., “Wind Load Evaluation System for the Design of Roof Cladding of Spherical Domes”, Journal of Wind Engineering and Industrial Aerodynamics, 2008, Vol. 96, pp. 2054-2066.

[9] Sterling, M., Baker, C.J. and Quinn, A.D., “Pressure and Velocity Fluctuations in the Atmospheric Boundary Layer”, Wind and Structures, 2005, Vol. 8, No. 1, pp. 13-34.

[10] Kho, S., Baker, C. and Hoxey, R., “The 5th Asia-Pacific Conference on Wind Engineering”, Tokyo University Press, Tokyo, 2001, pp. 509-512.

[11] Chen, Y., Kopp, G.A. and Surry, D., “Prediction of Pressure Coefficients on Roofs of Low Buildings Using Artificial Neural Networks”, Wind Eng. Ind. Aerodyn, 2003, Vol. 91, pp. 423-441.

[12] Launder, B.E. and Spalding, D.B., “The Numerical Computation of Turbulent Flows”, Comp. Math. Appl. Mech, 1974, Vol. 3, pp. 35-61.

[13] Canuto, C. Hussaini, M.Y. and Quarterini, A., “Spectral Methods in Fluid Dynamics”, Springer-Verlag, 1987, Vol. 12, No. 4, pp. 1473-1490.

[14] Murakami, S. and Mochida, A., “Development of a New Model for Flow and Pressure Fields Around Bluff Body”, Journal of Wind Engineering and Industrial Aerodynamics, 1997, Vol. 68, pp. 169-182.
[15] Lin, B., “Application of CFD Simulation Technology in the Large Complicated Structure Engineering”, Harbin Institute of Technology, Harbin, 2005, pp. 1-10.
[16] Kato, M. and Launder, B.E., “The 9th Sym. on Turbulent Shear Flow”, Tokyo University Press, Tokyo, 1993, pp. 4-16.
[17] Bremer, M. and Penalver, J., “The 6th FE Model Based Interpretation of Telescope Temperature Variations”, Bonn, Bonn University Press, 2002, pp. 186-195.
[18] Bremer, M. and Greve, A., “Front and Rear Perspective Heated Prototype Panels for the IRAM 15–m Telescopes in 28th ESA Antenna Workshop on Space Antenna Systems and Technologies”, Netherlands Technology Press, Noordwijk, 2005, pp. 943-960.
[19] Chamberlin, R.A., “Temperature Meaurements on the Leighton Telescope”, Surface Memo, 2003, Vol.5, pp. 124-130.

NEW EXPERIMENTAL RESULTS OF THE RESEARCH ON REINFORCED NODE IN SPACE TRUSS

Cleirton A. S. Freitas[1,*], Luciano M. Bezerra[2b], Rafael M. Araújo[1], Emanuel C. Sousa[1], Geverson M. Araújo[1] and Édipo A. Bezerra[1]

[1] Research Group on Structural Engineering in Cariri - GPEEC, Federal University of Cariri
http://www.ufca.edu.br, Av. Tenente Raimundo Rocha S/N, Cidade Universitária, Juazeiro do Norte, 630000 Ceará, Brazil.
[2] Department of Civil and Environmental Engineering, University of Brasília – UnB
http://www.unb.br, Brasília 70910-900, DF, Brazil
**(Corresponding author: E-mail: andrefreitas@cariri.ufc.br)*

Received: 25 August 2015; Revised: 7 January 2016; Accepted: 20 February 2016

ABSTRACT: In the first stage of this research the proposal of the reinforced node used in space truss was presented. Computer simulations and experimental lab tests were performed with small changes on the staking flattened-end connections, such as reinforcement and eccentricity correction. The results showed 68% increase in the truss load carrying capacity when the proposed changes were applied. However, small prototypes measuring 4 m^2 were used for laboratory testing. In this paper, for proposal validation, the same research was developed, this time in prototypes with 54 m^2. The outcome results of this research, confirmed a significant increase in the truss load carrying capacity. It is expected that factories can apply the reinforced node in space truss constructions to come.

Keywords: Space truss, steel connection, steel construction, steel roof

DOI: 10.18057/IJASC.2017.13.1.2

1. INTRODUCTION

Truss structures constitute a special class of structures in which individual straight members are connected at joints. The members are assumed to be connected to the joints in a manner that permit rotation, and thereby it follows from equilibrium considerations, to be detailed in the following, that the individual structural members act as bars, i.e. structural members that can only carry an axial force in either tension or compression [1].

Three-dimensional structures made of steel bars, widely known as space trusses, are frequently use in construction of roofs. These structures consist of steel bars, connected by bolts at nodes. There are several types of connections to attach these members. The choice of a connection system depends on structural layout, types of sections and distribution of bars.

Many patented connection systems are available and new ones continue to be invented but the code of practice does not include specific design rules for these connections. MERO system or bolted jointing system (Figure 1) was the first patented system for space structures [2]. The buckling behavior was observed in Taniguchi's work [3]. Many other patented systems were also developed but designers have frequently used non-patented systems due to their lower cost compared to patented ones [4].

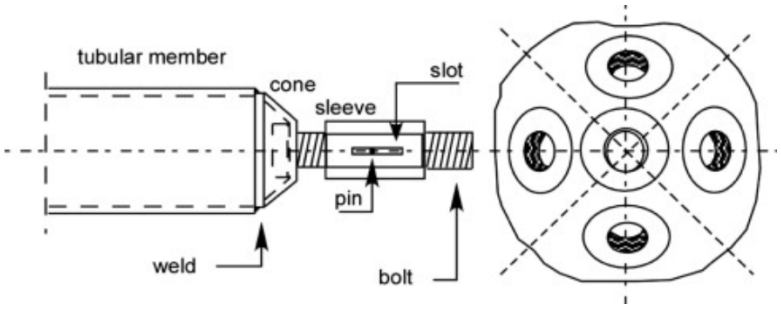

Figure 1. Mero Connection System [2]

One most used non-patented connection in China is the welded joint. It is possible to observe in reference [5] the design of welded tubular connections. Fatigue is an important issue in designing welded joints [6]. That paper presented a fracture mechanics approach to assess the fatigue life of CFCHS T-joints, which involves the determination of initial crack location and size, stress intensity factor and proper crack growth model (Figure 2). In [6], numerical and experimental analyses on welded joints were presented.

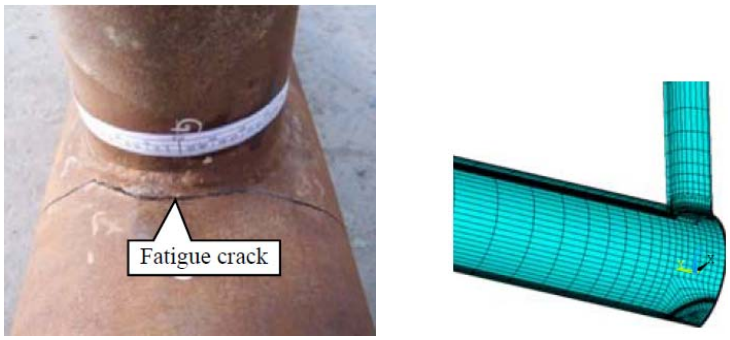

Figure 2. Fatigue Study in Welded Joints [6]

There are systems without a special nodal piece (Figure 3). In this case, the chord bars have flattened ends and can be continuous or not. Diagonal bars are flattened and bent at the ends. In Brazil, the most widely connection utilized in 3D trusses is the staking flattened-end connection (also known as typical connection, Figure 4) and the steel node (Figure 5).

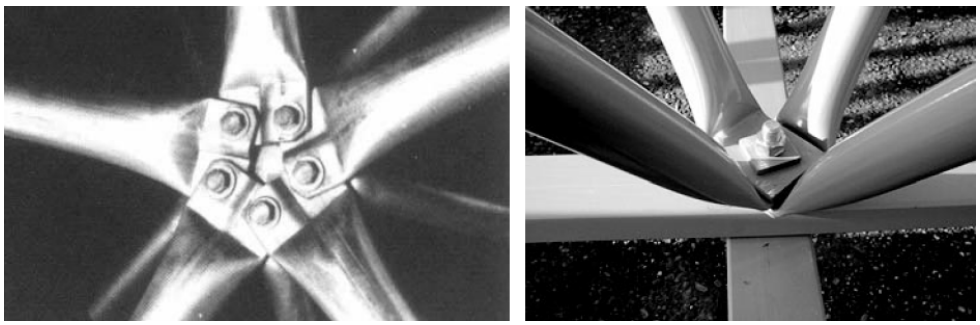

Figure 3. Systems Without a Special Nodal Piece [4]

Vacev's research [7] presented experimental analysis of the steel node. The joint was loaded by spatial set of forces that simulate real condition of the structure. Tested were made in real scale, according to the model originated after FE analysis. The results of a stress-strain FE analysis were presented and comparison of the two analyses was given for the most critical regions of the node.

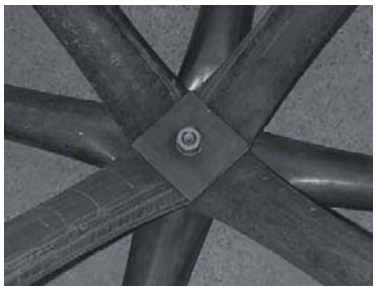

Figure 4. Flattened-end Connection [4]

Figure 5. Steel Node [7]

The advantages of the flattened-end connection (Figure 4) are price and installation time compared to the steel node (Figure 5). However, such connection (Typical Flattened-end) has disadvantages like eccentricities and stiffness weakening of the tubular members. Several accidents in space structures have also been reported in Brazil (Figure 6) [8].

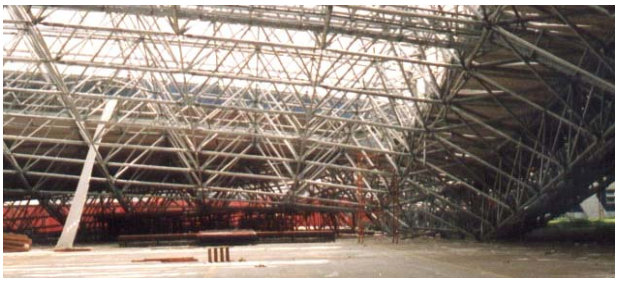

Figure 6. Convention center accident in Manaus [8]

Souza's research [9] presented the results of experimental analyses of space trusses using steel tubular bars with flattened-ends. The connections were formed by overlapped bars connected by single bolt (typical flattened-end). The behavior and collapse modes were determined by experimental analysis on six space trusses with 1.5 m height and spans of 7.5m x 7.5m and 7.5m x 15m (Figure 7). Structures with steel nodes (Figure 5) at the top corners and support points were also tested. The structural collapse was caused by either connection collapse or yielding at the bar ends. Traditional theoretical analysis models (linear truss model) are not suitable for these structures.

The connections failure was the predominant collapse pattern and was caused by plastic strains in the end bars, node rotations and slip among bars in the nodal region (Figure 8). These facts caused an increase in the displacements and the premature structural collapse.

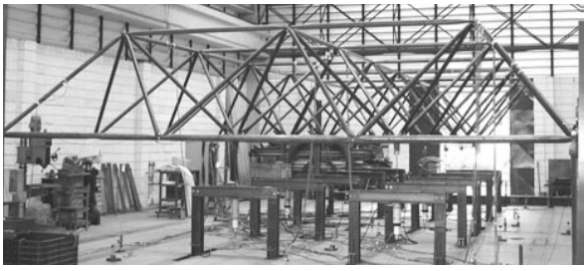

Figure 7. Experimental Tests [9]

Figure 8. Collapse Mode [9]

Nodal eccentricities E_1 and E_2 (Figure 9) are present in the staking flattened-end connection. Nodal eccentricity generates bending moments on the tube ends, and the end-flattening process reduces the stiffness of the tubular sections. Initially on this research it was proposed the correction of the eccentricity E_2 by the application of a spacer between diagonals and parallel chords (Figure 10). The purpose of a spacer is to make the diagonal axis and chord axis meet in the same point (A=B). Equation 1 presents the formula for the calculation of the spacer size (*d*). Taking into account a pyramid unit with its base length (*l*) and height (*H*), the thickness (*t*) of the tube wall (flattened) and the eccentricities E_1 and E_2 [8].

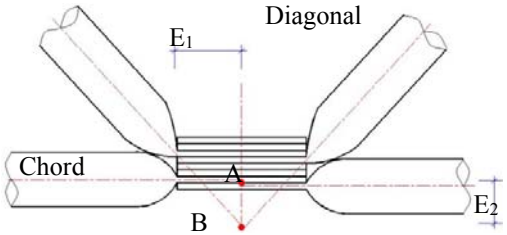

Figure 9. Eccentricities [8]

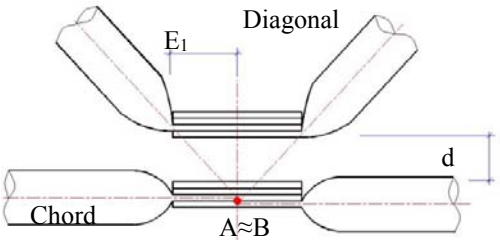

Figure 10. Correcting Eccentricity [8]

$$d = \frac{2HE_1}{l\sqrt{2} - 4E_1} - 8t \tag{1}$$

1.1 Preliminary Steps on the Research

In recente years, the first step on this research were carried out by simple numerical finite element models and experimental investigation with small prototypes [8], [11] and [12]. The typical connection (Figure 11) and the suggested modifications (Figure 12) were compared. In order to do this, it was taken into consideration the prototype trusses (with $4m^2$) made of four pyramidal units connected at nodes (pyramid vertices). Each pyramid has a square base of *l*=1000 mm and height *H*=707 mm (Figure 13).

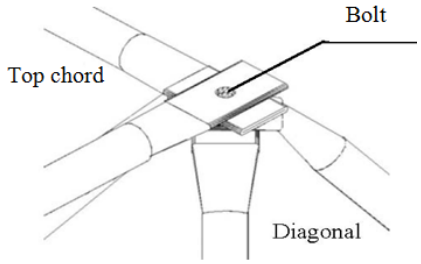

Figure 11. Typical Flattened-end

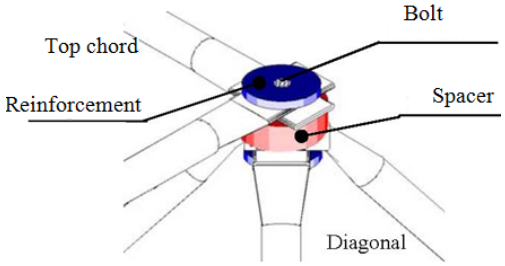

Figure 12. Modified Node

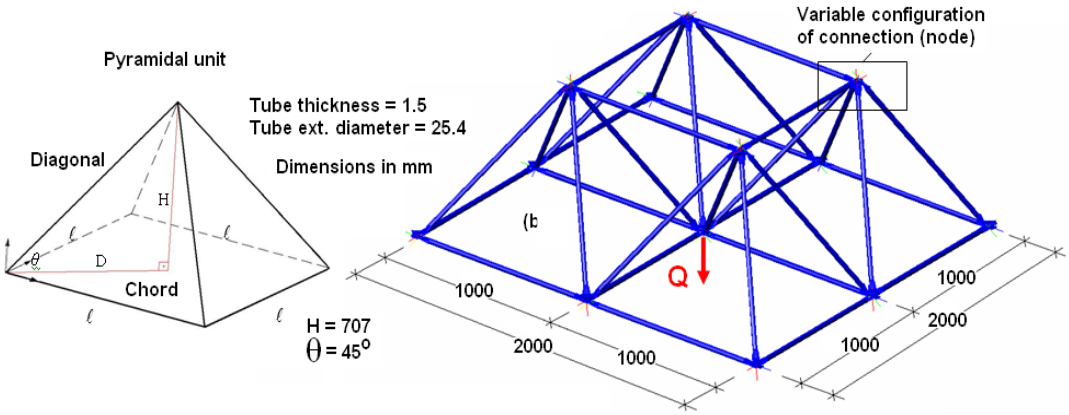

Figure 13. The Prototype Truss Geometry (mm)

1.2 First Numerical Results

The SAP2000 program [10] was used to discretize the 3D standard truss (Figure 14) and to carry only linear analyses. Prototypes were modeled with FRAME elements. The restrictions were applied to nodes 10, 11, 12 and 13. The imposed load of Q = 37 kN was applied to central node 9. The linear analyses showed that the presence of a spacer in the truss produces a significant fall in the bending moment and in the displacement present in the truss with staking flattened-end connections. The bending moment in the modified node model (Figure 16) had a reduction of at least 62% when compared to typical node (Figure 15).

The node displacement in the modified node model (Figure 18) dropped nearly 70% compared to typical node (Figure 17) [11]. Numerical linear analyses satisfactorily show that the spacer substantially reduces bending moments and displacements. It makes the truss stiffer and more resistant as can be seen by laboratory experiments reported in the next section.

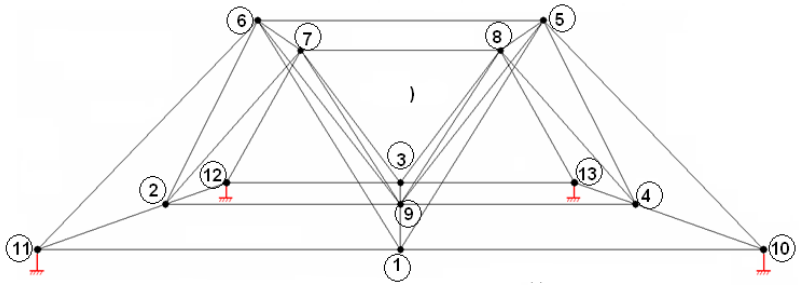

Figure 14. FE Prototype Models

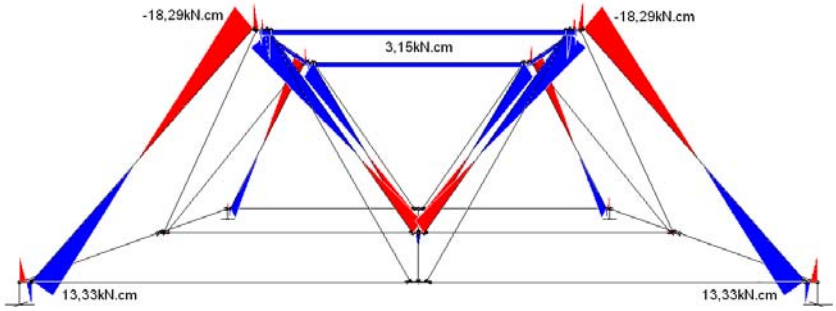

Figure 15. Bending Moment in the Typical Node

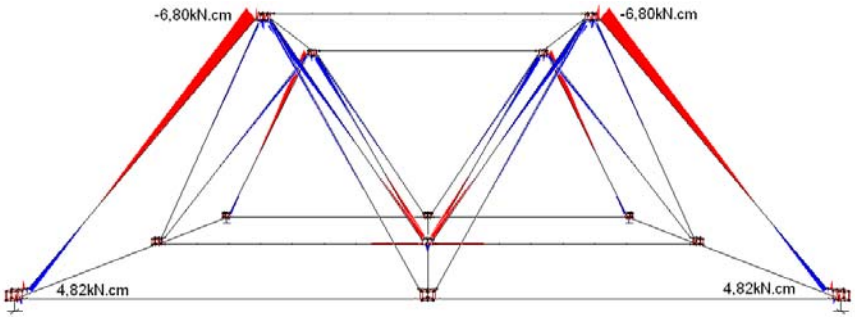

Figure 16. Bending Moment in the Modified Node

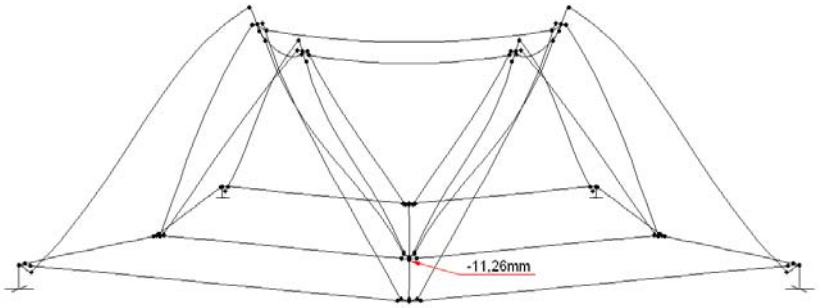

Figure 17. Displacement in the Typical Node

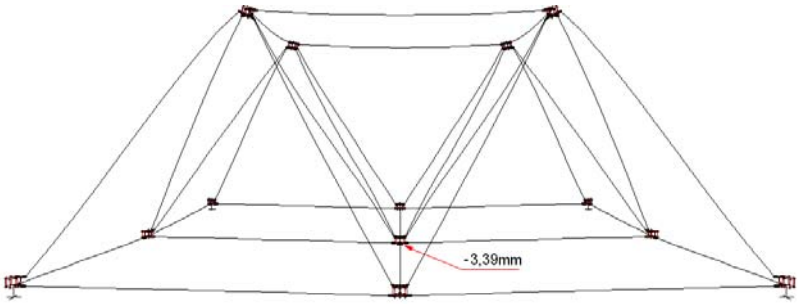

Figure 18. Displacement in the Modified Node

1.3 First Experimental Results

Six prototypes, as described in section 1.1, were tested in the Structural Laboratory at the Department of Civil Engineering in the University of Brasilia (UnB) [8]. Half of the prototypes were with typical flattened-end node and the other half with nodes with spacers and reinforcements (Figure 5 and 6). Spacers will correct eccentricity while reinforcements avoid early local instability in the region of the flattened ends of the tubes. The corners of the prototype trusses were fixed on a very stiff steel base available in the Laboratory. A downward vertical load was applied to the middle node 9 in load-steps of 1.0 kN (Figure 19).

Figure 19. FE Prototype Models

In Figure 20, the model with modified node (point 1 at 42 kN) had an increase of 68% on load capacity compared to typical node (point 2 at 25 kN). In the model with typical node the local collapse was basically characterized by an excessive wrinkling of a node or connection but not necessarily buckling of a member (Figure 21). For the modified model no excessive node deformation was observed when the structural collapse occurred (Figure 22) [12].

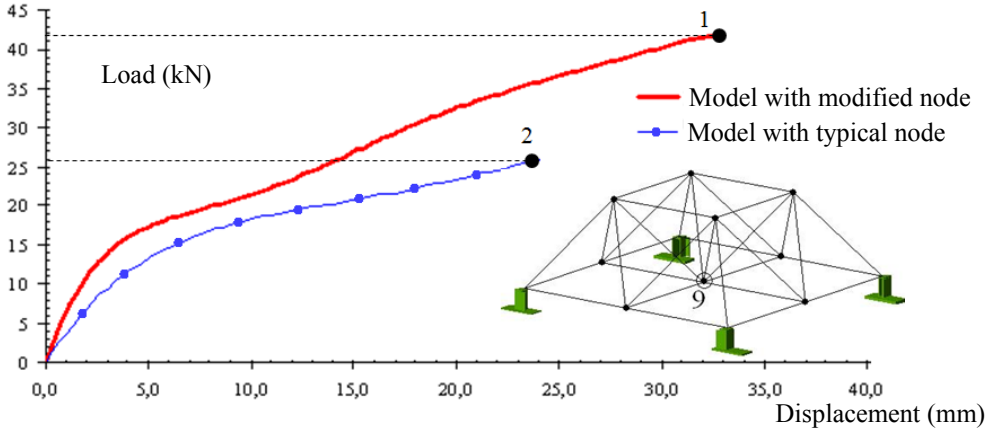

Figure 20. FE Prototype Models

Figure 21. Collapse of the Typical Model (P2 - 25kN)

Figure 22. Collapse of Modified Model (P1 - 42kN)

2. OBJECTIVE AND METHODOLOGY OF THIS RESEARCH

Despite the good results obtained in the preliminary studies [8], [11] and [12], further investigation is necessary before recommending factories to apply the reinforced node in future buildings. That is why the last study was carried out numerically and experimentally on prototypes with small dimensions. Therefore, the aim of the present research paper is to confirm the proposal of reinforcement using new experimental prototypes; but this time covering fifty four square meters. This study was carried out by numerical FE models and experimental investigation of 3D trusses. The performance of typical connection (Figure 11) and the suggested modifications (Figure 12) were again compared.

The prototype truss was made of pyramidal units connected at nodes corresponding to pyramid vertices. Each pyramid has a square base with length of l=1500 mm and height of H=1061 mm (Figure 24). The diagonal inclination angles are, therefore, 45º in respect to the base plane of the pyramid. The truss steel tubes have 38 mm (1½ in) of external diameter and 1.20 mm (0.047 in) of thickness. The tubes are made of Brazilian steel known in industry as MR250 [13] which is equivalent to the ASTM A36 [14]. Standard Samples were tested in lab (accord to Figure 23) and the following properties were observed: Yielding Stress adopted to be 250 MPa (value between 250 and 290 MPa); Modulus of Elasticity, 205000 MPa (value between 200000 and 210000 MPa) and Poisson's ratio 0.3. Taking into account the truss dimensions and tube thickness, the spacer is found to be 21.50 mm (7/8 in) thick. The adopted diameter of the spacer was 76.2 mm (3 in). Reinforcement plates of 4.76 mm (0.18 in) thickness reinforced the node – plates just need to be thicker than the tube thickness. The spacer was made of steel, but in recent study we are trying cheaper material [15].

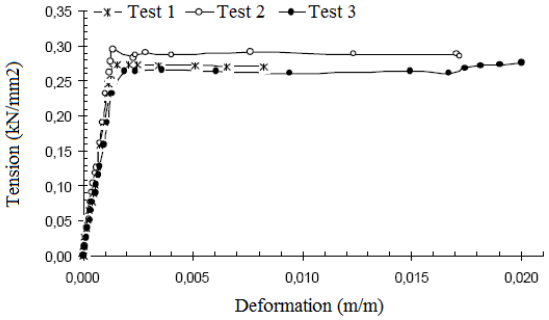

Figure 23. Characterization of Material in Lab

Restrictions for displacement and rotations are applied to nodes on the supports of the truss located on the corners representing the support conditions which are replicated in the experimental tests. See in Figure 25 the nodes where the loads "Q" were concentrated.

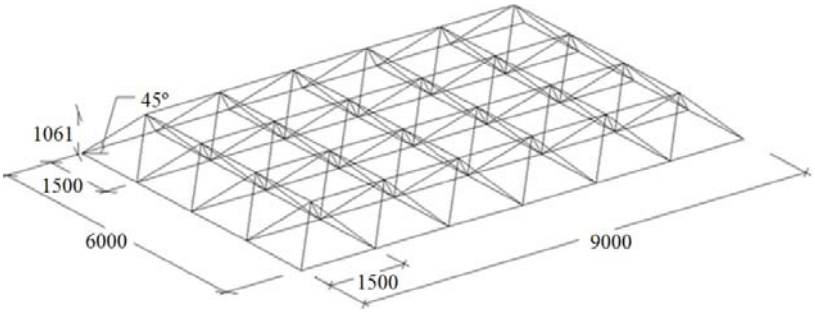

Figure 24. The Current Prototype Truss Geometry (Units in Millimeter)

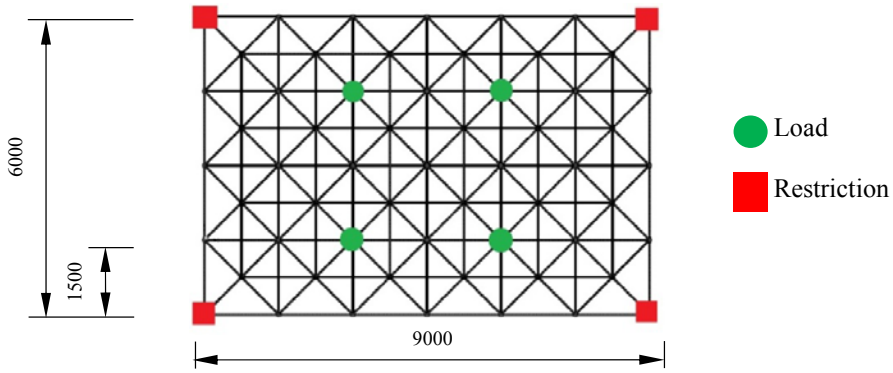

Figure 25. Plan View of the Prototype (Units in Millimeter)

3. NUMERICAL STUDY

3.1 Finite Element Model

SAP2000 [11] is here used to discretize the 3D standard truss. From the 3D view of FE prototype model in Figure 26, it is possible to observe the element members. Restrictions for displacement and rotations are applied to corners. The support conditions were replicated in the experimental tests. Point loads were applied at four nodes, beginning at 10.0 kN and adding up to 40.0 kN. Two types of FE, from the SAP element library, were used for the numerical modeling. The SHELL elements were used to discretize the spacer. The FRAME elements were used to discretize the bars. Two models are discretized: The typical connection (Figure 27) and the suggested modifications (Figure 28). Nodes 1 to 5, at the line in the middle of the truss (Figure 26), were used to compare the vertical displacements of the two models.

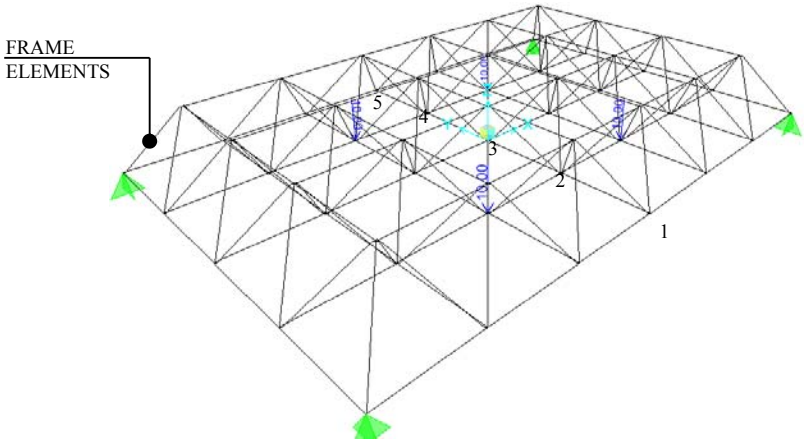

Figure 26. FE Prototype Models

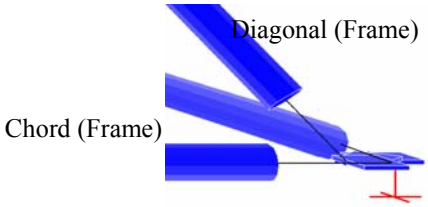

Figure 27. Typical Flattened-end

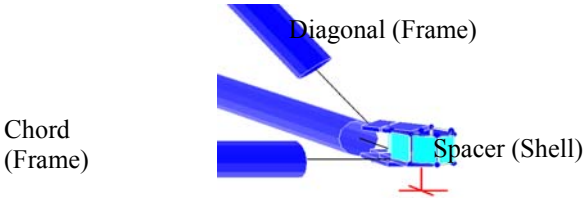

Figure 28. Modified Node

The prototype geometry has symmetry in both axis X and Y. For this reason, the elements stresses were symmetrically distributed. Despite the model was made with all the members, results were analyzed only in a quarter of the model. In Figure 29 it is possible to observe the selected elements that were used for the analyses of the axial forces and bending moments.

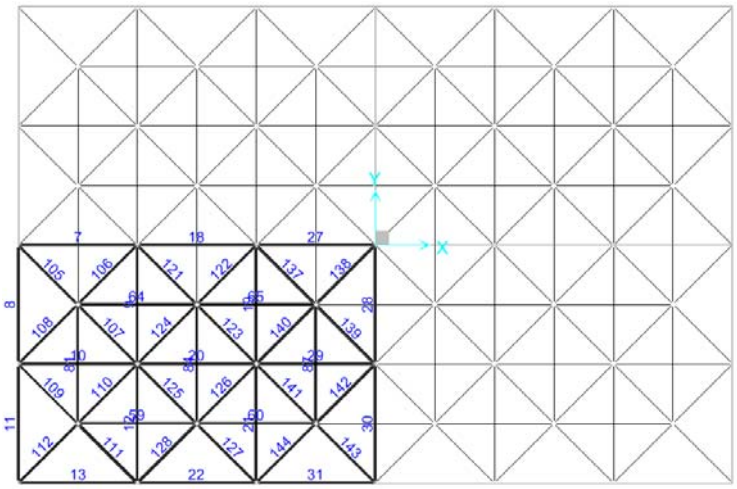

Figure 29. Plan View of FE Prototype Model

3.2 Axial Force

Figure 30 shows the graphs of the axial forces in the element members with modified nodes and typical nodes. With this graph it is possible to observe that the axial forces are almost the same. The numbers of truss elements were also depicted in Figure 29.

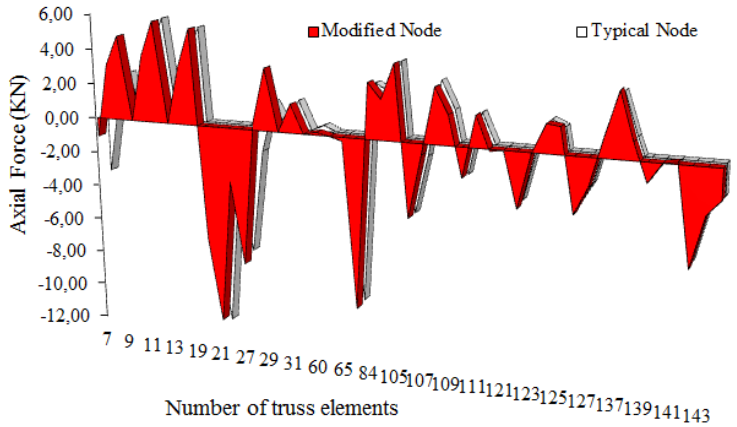

Figure 30. Axial Force Results of the Truss Elements

3.3 Bending Moment

Figure 31 shows the graphs of the bending moments in the element members with modified nodes and typical nodes. The presence of spacers in the modified truss produces a significant fall in the bending moment. The reduction was nearly 52% in all members.

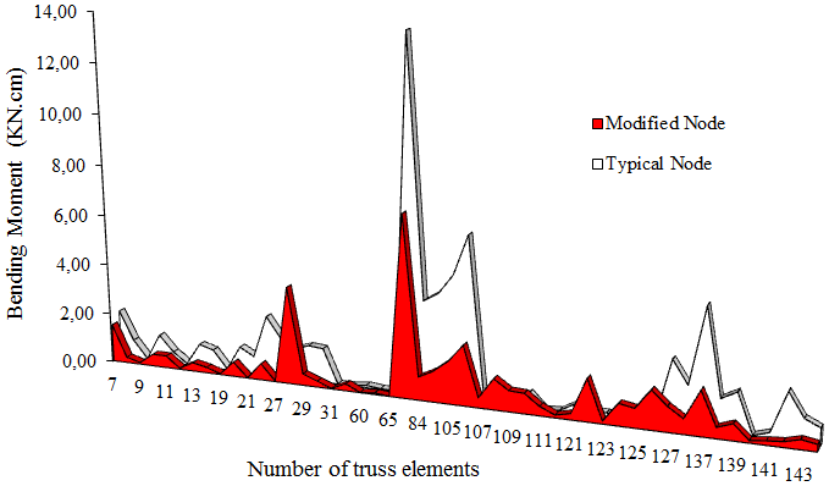

Figure 31. Bending Moment Results of the Truss Elements

3.4 Displacement

Figure 32 shows the graphs of the displacements of the middle nodes (in Figure 26) for trusses with modified nodes and typical nodes. Again, the presence of spacers in the modified truss produces a reduction in the displacement values. The reduction was about 16%.

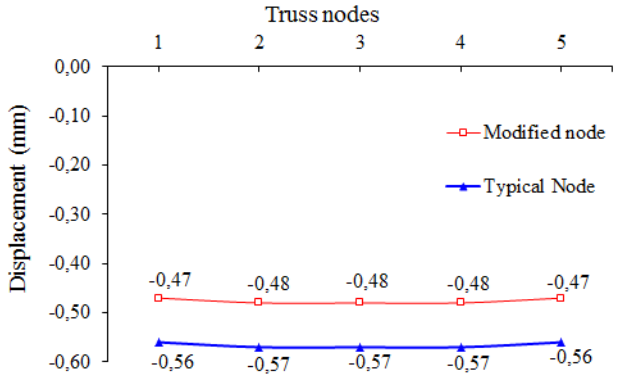

Figure 32. Displacement Results of the Truss Elements

4. EXPERIMENTAL STUDY

4.1 Experimental Program

The experimental program seeks simple quantitative and qualitative information on space trusses, taking into account two different nodal types (Figure 33 and 34). Static tests were carried out on truss prototypes under an increasing vertical load applied to four nodes (Figure 25). Four hydraulic jacks and one hydraulic pump were used (Figure 35).

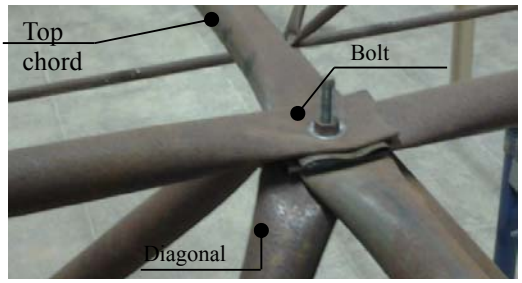

Figure 33. Typical Flattened-end

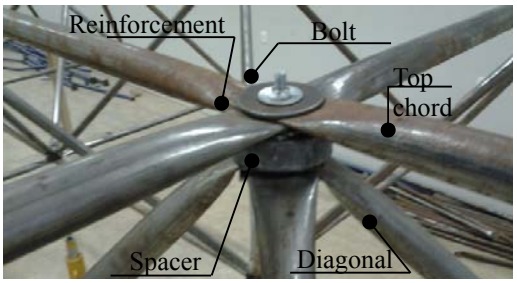

Figure 34. Modified node

Figure 36 shows the hydraulic pump control and their components, such as electric engine, oil compartment box and manual valve control. The measuring system of the displacement and the load were composed by Dial Test Indicator (DTI), DTI Support, Load cell and Reading panel, shown in Figure 37. The load is gradually applied up to the moment truss collapse is reached. For each specific connection system, i.e. nodal types, one experimental truss prototype was built and tested. The prototypes were tested in the Structural Laboratory at the Department of Civil Engineering in the Federal University of Cariri. The corners of the prototype trusses were fixed on a very stiff steel column available in laboratory. Downward vertical loads are applied to the nodes. Figure 38 shows the complete assembly for the lab tests.

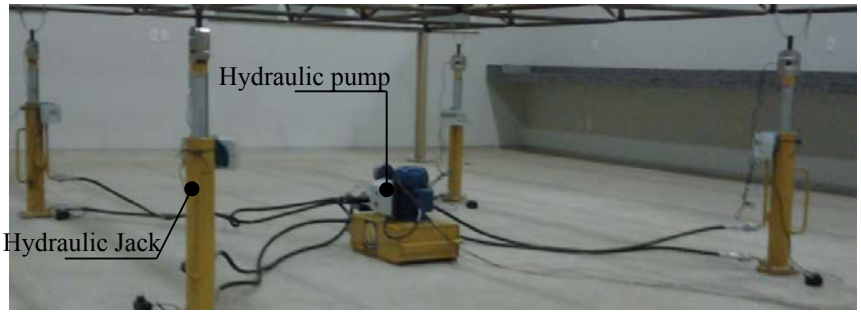

Figure 35. Load System Applied in the Lab

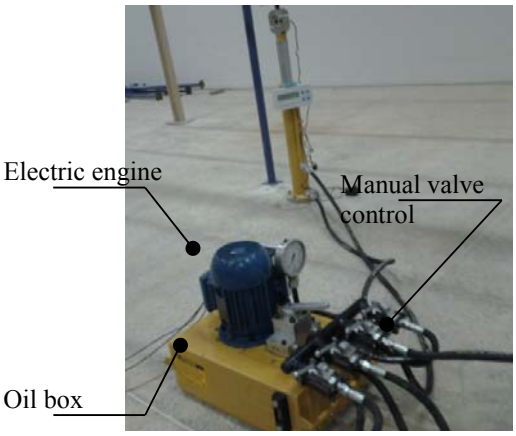

Figure 36. Hydraulic Pump Control

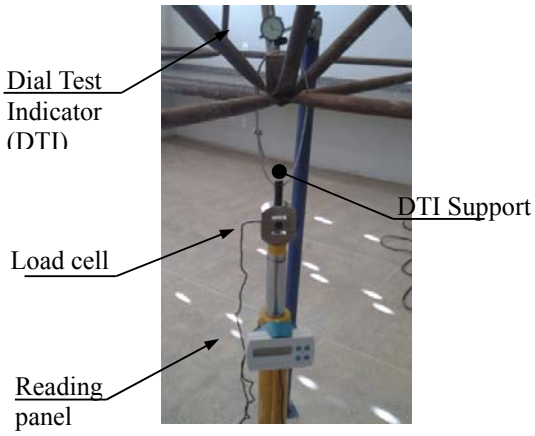

Figure 37. Measuring System

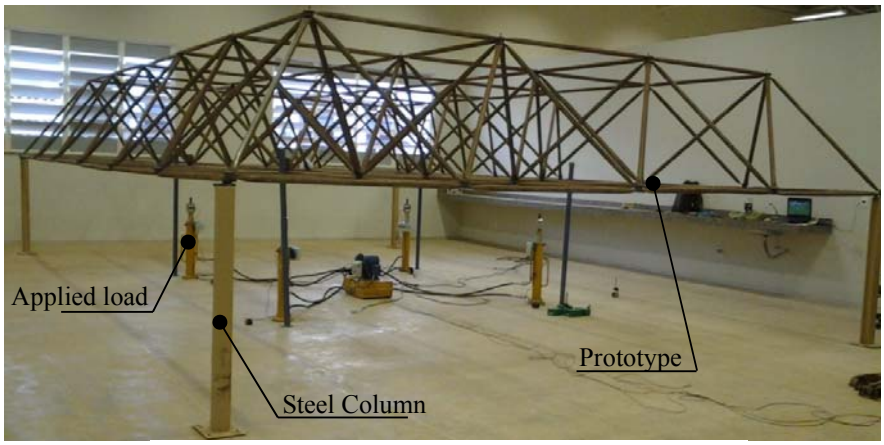

Figure 38. Prototypes in the Laboratory at UFCa

Each prototype has a rectangular base of 6m x 9m wide (54 m^2) and 0.94 m high, with geometry as outlined in Figure 24. Tube dimensions and material properties were specified previously. At the four nodes, (see Figure 25), the pulling load Q is produced by four cables which are attached to hydraulic jacks. Load values are controlled with the load cells. The hydraulic jacks have 160 kN on load capacity and the load cells read up to 100 kN with 0.1 kN precision. The cables pull the prototype downwards in load-steps of 1.0 kN. After every given load step, readings of the total load and displacement were measured at the node where loads were applied.

4.2 Experimental Results

In this research, global collapse is the instant when any small load increment is no longer taken by the probed prototypes. Global collapse is also characterized by the buckling of critical members under compression and bending combined. In Figure 39, the experimental results were plotted with results stating typical prototypes collapse at point 2 where Q = 24 kN and node with reinforcement at point1 where Q =35.1 kN (4x8.78 kN), representing an increase of 46.2% in the collapse load. For the same load level, it was also observed that trusses with typical nodes (staking flattened-end nodes) presented greater displacements than the prototypes with spacers and reinforcements.

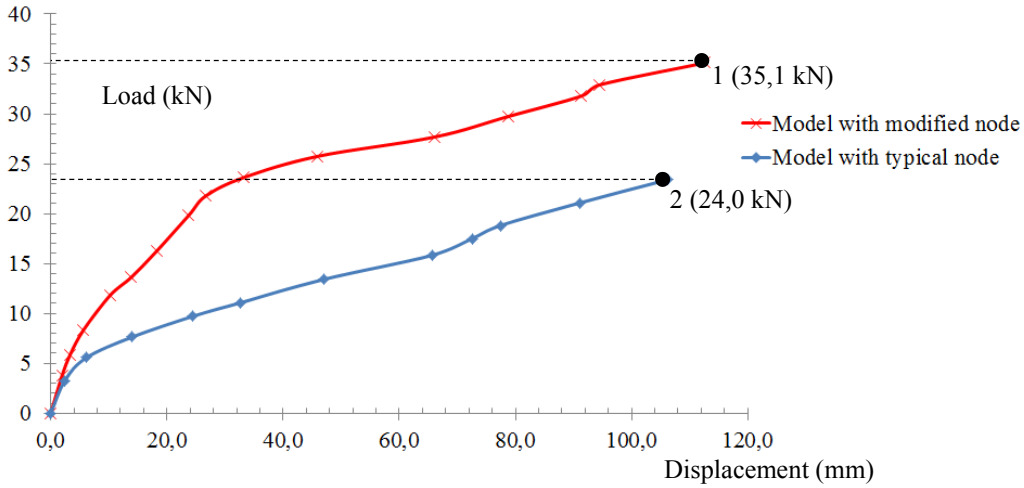

Figure 39. Experimental Results

Figure 40. Collapse in Typical Model (24kN)

Figure 41. Collapse in Modified Model (35.1kN)

In fact, as shown in Figure 40, the corresponding prototypes with typical node showed excessive wrinkling and displacement of about 106 mm with the load of 24kN. For prototypes with spacers and reinforcements no excessive deformation was observed when the applied load Q reached 25 kN with displacement of about 45mm (Figure 41). Therefore, for the same load (24kN) the typical prototypes (with staking flattened-end connections) presented local collapse whereas no local collapse was observed in the modified prototypes.

5. CONCLUSION

The goal of this research was to validate the proposal of correcting staking flattened-end nodes to improve the load carrying capacity of space trusses. Such trusses are commonly used with staking flattened-end nodes, also known as typical nodes. They are cheap and fast to assemble. The flattened-end node shows eccentricities and the flattening process reduce the moment of inertia of the tubes. The eccentricities at the nodes produce bending moments. To increase the load carrying capacity of this type of 3D truss, spacers and reinforcement plates were proposed. Linear numerical analyses satisfactorily show that spacers correct eccentricities and significantly reduce the bending moment at the nodes.

Experimental and numerical studies were realized, with outcome results proving that correcting the connection eccentricities with spacers and reinforcement plates significantly increases the load capacity of 3D trusses. The experimental tests showed that the implementation of spacers and reinforcements increased in 46% the prototypes strength to withstand local collapse. These alternatives can be easily implemented to new truss design or in the upgrade of existing trusses. The next step of this research will be a study considering second-order FE analyses of the space truss members, as done by [16]. Thereby, it will be possible to simulate the displacements of the truss members and compare them to experimental results.

ACKNOWLEDGMENTS

This article is part of an ongoing research at Federal University of Cariri. The authors want to express their gratitude to CNPq, to CAPES, and to FUNCAP for the financial support.

REFERENCES

[1] Krenk, S., Hogsberg, J., “Statics and Mechanics of Structures”, Hardcover, 2013, ISBN:978-94-007-6112-4.

[2] Caglayan, O. and Yuksel, E., “Experimental and Finite Element Investigations on the Collapse of a Mero Space Truss Roof Structure, Case Study”, Engineering Failure Analysis, 2008, Vol. 15, pp. 458–470.

[3] Taniguchi, Y., Saka, T., Shuku, Y., "Buckling Behavior of Space Trusses Constructed by a Bolted Jointing System", Space Structures, 2009, Vol. 4, pp. 89 – 97.

[4] Souza, A. C. and Gonçalves, R.M., "Mechanism of Collapse of Space Trusses with Steel Hollow Circular Bars with Flattened Ends", International Journal of Space Structures, 2005, Vol. 20, pp. 201 – 209.

[5] Marshall, P.W., "Design of Welded Tubular Connections, Basis and Use of AWS Provisions", 1992, Elsevier Science Publishers, Amsterdam.

[6] Gu, M., Tong, L.W., Zhao, X.L. and Zhang, Y.F., "Numerical Analysis of Fatigue Behavior of Welded CFCHS T-joints", Advanced Steel Construction, 2014, Vol. 10, No. 4, pp. ~~pp.~~ 476-497.

[7] Vacev, T., Kisin, S., Ranković, S., "Experimental Analysis of an Original Type of Steel Space Truss Node Joint", Architecture and Civil Engineering, 2009, Vol. 7, pp. 43 – 55.

[8] Freitas, C.A.S., "Estudo Experimental, Numérico e Analítico de Conexões de Estruturas Espaciais em aço com correção e reforço na ligação típica estampada", DSc Thesis (in Portuguese), 2008, Department of Civil Engineering, University of Brasilia.

[9] Souza, A. C. and Gonçalves, R.M., "Behavior of Tubular Space Truss Connections with Stamped End Bars", International Journal of Space Structures, 2002, Vol. 5, pp. 337 – 345.

[10] SAP2000, User's Guide: A Structural Analysis Program for Static of Linear Systems. Educational Version, Computers & Structures Inc., 1999, Berkley, USA.

[11] Bezerra, L. M., Freitas, C. A. S., Matias, W. T., Nagato, Y., "Increasing Load Capacity of Steel Space Trusses with End-flattened Connections", Journal of Constructional Steel Research, 2009, Vol. 65, pp. 2197 - 2206.

[12] Freitas, C. A. S., Bezerra, L.M., Silva, R. S. Y. C., "Numerical and Experimental Study of Steel Space Truss with Stamped Connection", Journal of Civil Engineering and Architecture, 2011, Vol. 5, pp. 494-504.

[13] Associação Brasileira de Normas Técnicas, NBR 8800. "Projeto e execução de estruturas de aço de edifícios: método estados limites". Rio de Janeiro, 2008.

[14] American Institute of Steel Construction AISC – LRFD (1999), "Manual of Steel Construction", Chicago.

[15] Freitas, C.A.S., Nobrega, M.M.S., Bezerra, E. A., Cavalcante, O. R.O., "Polymer Composite with Sisal Fiber Used for Node Reinforce in Space-Truss with Stamped Connection", Applied Mechanics and Materials, 2015, Vol. 719-720, pp. 202-205.

[16] Fong, M., Peng, Y.P. and Chan, S.L., "Second-order Analysis and Experiments of Semi-rigid and Imperfect Domes", Advances in Structural Engineering, 2013, Vol.15, No.9, pp.1549-1558.

INVESTIGATION OF CAPACITY ON THE HOLLOW SECTIONS CONNECTIONS WITH STIFFENING PLATE

Mehmet Fenkli [1,*], İlyas Devran Çelik [2];
Nurettin Alpay Kımıllı[2] and Mustafa Sivri[3]

1 Süleyman Demirel University, Technology Faculty, Department of Civil Engineering, Isparta 32260, Turkey
2 Süleyman Demirel University, Engineering Faculty, Department of Civil Engineering, Isparta 32260, Turkey
3 Süleyman Demirel University, Technical Sciences Vocational School, Department of Construction Technology, Isparta 32260, Turkey
**(Corresponding author: E-mail: mehmetfenkli@sdu.edu.tr)*

Received: 3 September 2015; Revised: 3 April 2016; Accepted: 10 April 2016

ABSTRACT: Buildings behave according to their geometrical types, the profile specifications of static structural elements and the classifications of their materials. This structural behavior is a kind of structural reaction to an earthquake. This reaction may be absorbed by the ductility of the structure. There is an indefinite situation in the description of the level of ductility for a static system in the earthquake occurrence calculation for the moment-shifting steel-frame system that consists of square or circular profile elements.

This objective of this manuscript is to overcome local buckling on welded RHS column/beam assemblies and thereby establish a design algorithm. We conducted experimental analysis under the cyclical loads by added rigidity plate having different dimensional parameters to a RHS at the assembly point. We optimized the design and the dimension of the plate with the expansion of the subject models of the experimental analysis by using the Ansys finite-element program.

Keywords: Turkish Earthquake Code 2007, CHS (Circular Hollow Section), RHS (Rectangular Hollow Section), welded moment resisting connections with rigidity plate, moment resisting steel frame systems, cyclic static loading, moment-rotating relationship, detail of ductility

DOI: 10.18057/IJASC.2017.13.1.3

1. INTRODUCTION

The energy of an earthquake and the reaction of the structure against that energy define the behavior of a structure under the seismic effect. In other words, a construction uses kinetic energy, the energy of elastic creep, viscose absorbing energy and hysteric energy to absorb the energy applied by an earthquake. If the absorbing energy is greater than the energy from the earthquake, it is blocked by absorbing energy. Contrastingly, if the absorbing energy is less than the energy from the earthquake, the difference between absorption and the energy of the earthquake is balanced by hysteric energy. This difference is referred to as the ductility of a structure. The behavior of the structure against an earthquake and the rigidity of its static elements are crucial in the design of a structure against an earthquake as well as in regard to ductility. It is not desired to have decreases in load-bearing capacity and rigidity while the ductility increases. For that reason the greater rotations are awaited in plastic behavior with no decrease in load-bearing capacity. However, the static elements have failed to meet the large plastic rotations to compensate for the earthquake, due to some negative situations such as local buckling, cracking and torsion.

Steel static elements, having different assembly and design geometries, are used in practice. The relationship between profile effect and creep is unique to each system and its particular assembly. This situation affects the structure's ability to absorb energy (ductility). The types of materials of the assembly parts (welds, bolts and strengthening plates) in the system, the application quality and

dimensions are the main factors in the ductility of the steel structure. Therefore, certain details have been developed to prevent brittle breakage in the assembly points at the frame system and to ensure that the assembly points behave in parallel with the ductility of the system. However, the use of measures against the details described in the literature and local creep are for the hot-rolled standard profiles of types I, C, T and L. There are differences in the behavior and creep of the square profiles or static hollow elements commonly used in practice. For that reason it is not possible to consider the square profiles with the details for the standard profiles, nor is it appropriate to conduct analysis according to them.

The local buckling situations described in Euro Code 2003 Section 1-8 and CIDECT Division 3 [7] are shown in Figure 1. Deformations have been reviewed in two parts as axial load and bending effect for the circular profile. They are submitted for comparison in Figure 1.

UNDER THE AXIAL LOAD

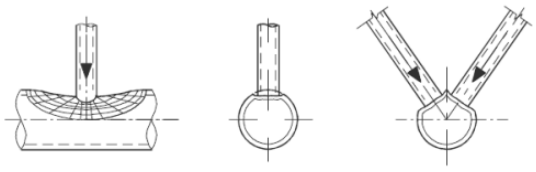

a) The buckling position at the upper head of the column

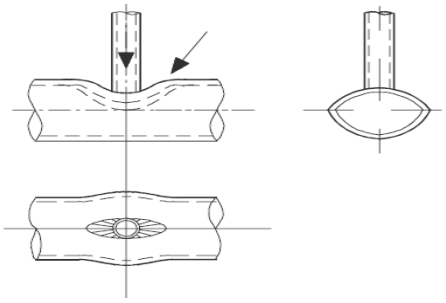

c) The position of local buckling on the body of the column (position of deformation with distention)

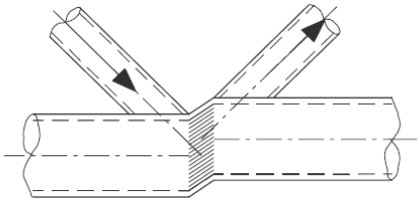

e) The position of deformation at the column panel location

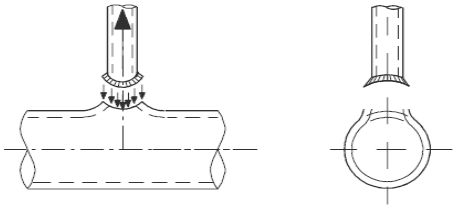

g) The position of rupture depending on tearing at the upper head of the column

UNDER THE MOMENT EFFECT

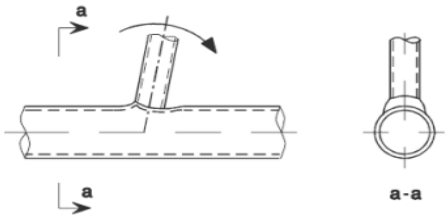

b) The buckling position at the upper head of the column

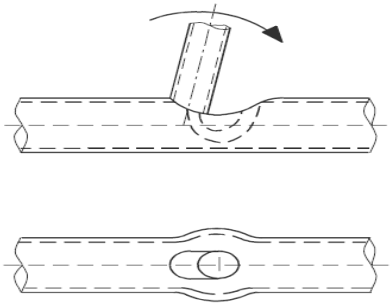

d) The position of local buckling on the body of the column (position of deformation with distention)

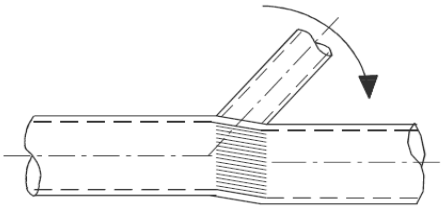

f) The position of deformation at the column panel location

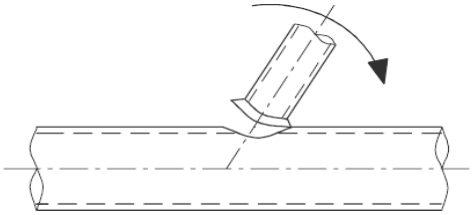

h) The position of rupture depending on tearing at the upper head of the column.

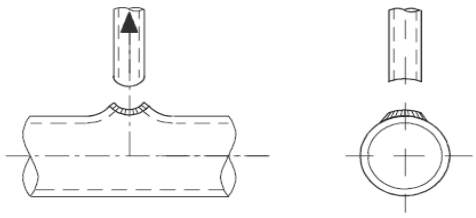

i) The position of rupture at the beam/cross element

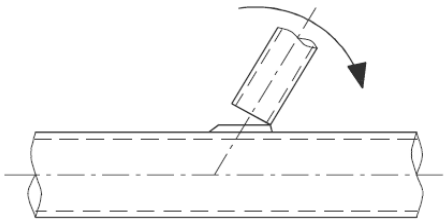

k) The position of rupture at the beam/cross element

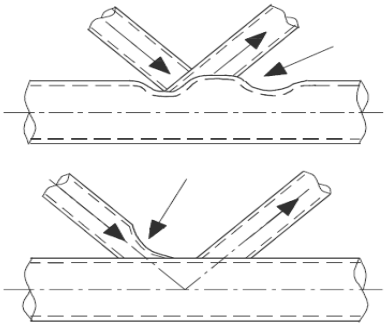

l) The buckling position at the cross element

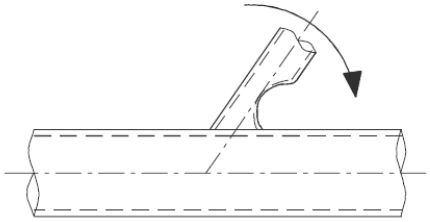

m) The buckling position at the cross element

Figure 1. The Deformation Positions Described for Square-profile Assemblies in EURO Code and CIDECT

The behavior of steel structures under horizontal load is related to the specifications of the material, the geometry of the profile and the details of the assembly. Accordingly, the material and profile specifications are vital in defining the rotational capacity of the assembly. It is preferable not to have brittle breakage at beam-column assembly points, and consequently the assembly points must behave in parallel with the ductility of the system. This ductile behavior at the assembly is one of the most important factors affecting the rotational capacity at the assembly point of the static element. For that reason many studies have been conducted, reviewing the position of creep that could affect the rigidity, ductility and the structural behavior at square-profile assemblies.

The assemblies in node points of the "Vierendeel" system --the first type of shear system to be designed with the use of square profiles-- were used in the studies included in the Design Guide (CIDECT) Euro Code. Moreover, many studies have been conducted in regard to assembly types, representing the rigid and semi-rigid assemblies, including the moment-rotation relationship and strength (Figure 2, Vierendeel-type node point). Rigidity plates have been used to overcome the local bucklings incurred on the profiles. Some examples of the rigidity plates are shown in Figure 2. Moreover, some of the dimensional parameters regarding the plates used for the type-T assembly are covered in this study and included in the Design Guide. Accordingly, it is advised that the t-value of the head plate is equal to or greater than two times the beam thickness involved in the assembly. The limits for the length and width of the plate are defined according to the dimensions of the column or beam included in the assembly.

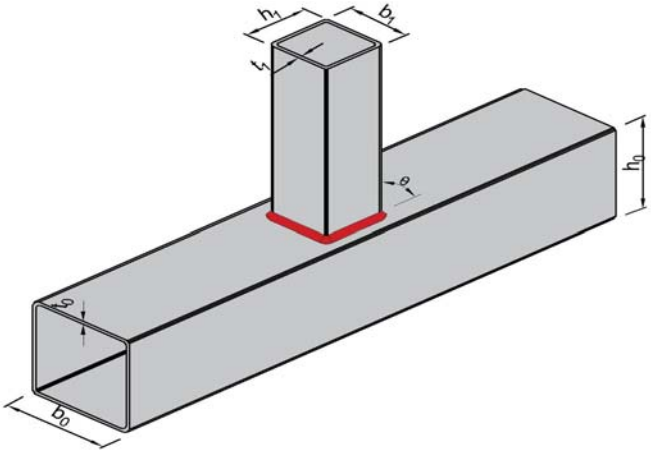

a) The detail of the welded assembly (not reinforced)

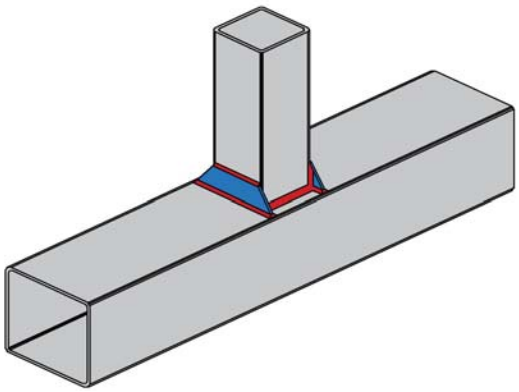

b) The detail of the assembly with reinforcement plate

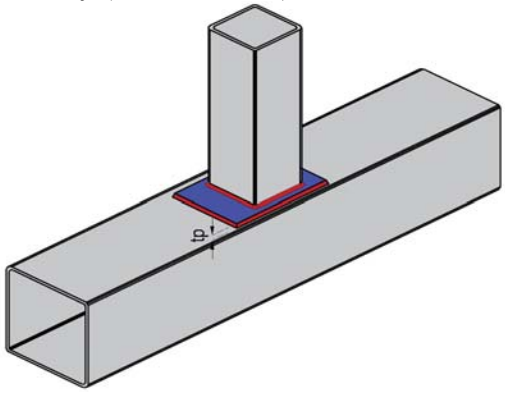

c) The detail of the assembly with head plate

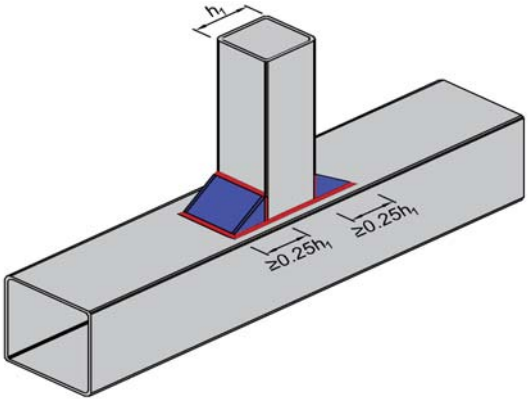

d) The detail of the assembly with amulet element

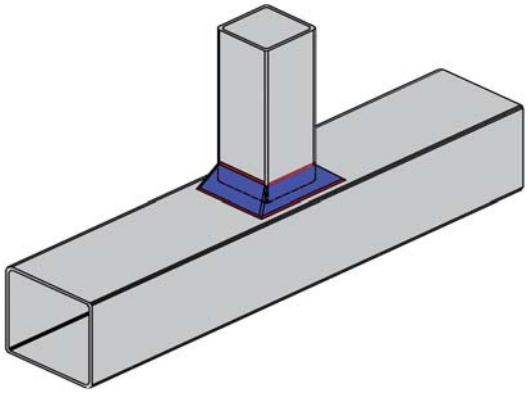

e) The detail of the truncate pyramid assembly

Figure 2. Node Points of Vierendeel Type Rectangular Square Profile (RHS)

Researchers have considered the welded assemblies of square profiles under the effect of moment as rigid and semi-rigid assemblies according to the β (b_1 / b_0) coefficient between the profiles combining the assembly. If β is 1.0, the assembly is rigid, but if β is less than 1.0 the assembly is identified as semi-rigid. In the condition of β<1, it is defined that the rigidity plates are added to the node point to increase the rigidity of the plate according to the details described in Figure 2b, c, d and e. The frame of this subject has not been expanded to cover all types of square profiles of assembles Design Guide 3 [5]. Other than the rigidity description, the deformation limit and

maximum stress values have been described in Zhao [23] study for the type-T node point. It is defined that the deformation value occurring at the head of column could be the maximum strength capacity for the type-T assembly. It is shown that the deformation limit for the square profile with welded assembly is up to the coefficient β, which is described as the ratio of cross/pillar width to the width of the column. Mashiri and Zhao [14], in their study, tied the circular cross/pillar element to the rectangular square profile with the type-T assembly using welds. The profiles used in the assembly of the study are thin-walled, and the wall thickness is equal to 4 mm or less. There has been identified a model for a column having deformation in determining the displacement limit for the resulting capacity of a node point being assembled in that study. Plastic analysis has been conducted for a digital model designed by using the theory of a strain model derived from the study. It has been verified by comparing the resulting tension value obtained through the use of a digital model and the value acquired from the experimental result. Wang et al. [21] tested the assembly of being in the "I" form and circular profile column against horizontal force under a constant axial load affecting the integrity of the cylinder. The assembly is composed of two different combinations like strong column / weak beam and weak column / strong beam. There were eight experiments in that respect, of which five pertained to the strong column/weak beam combination. The column-strengthening process was applied, being covered by a ring through the use of an additional plate. The strengthening method using a ring was conducted for all eight experimental samples. Additionally, five circular profile columns filled with concrete were used in some examples of the strong column / weak beam design. The experimental analysis showed that a weakened beam gave high seismic performance results in terms of the dissemination of tension and the diffusion of energy under the horizontal load for the five weakened beam samples as the strong column / weak beam combination. It was observed that weakened beam, when used at assemblies, played a key role in structural behavior, while the calculation of the resulting load made a vital contribution in defining the formation order of the plastic joint. It was shown that the ring type of rigidity plate prevented the buckling at the column in the study by Hwang et al. [8], and experimental research has been conducted regarding the strength of structure and the form of the dents at the assemblies, consisting of square beam / circular columns constructed in the form of steel scaffolding. Eight experiments were conducted, whereby the use of monotonic loading experiments showed that the circular columns are more rigid than the rectangular columns. The contribution to the rigidity of concrete filling at the assembly of the square beam / circular column was also reviewed. The mode of dent/collapse could be described more accurately, and it proposed more reasonable values for equivalent body width. Also Duff [6], Redwood [17], Cute [3], Mehrotra and Redwood [15], Lazar and Fang [11], Wardenier [22], Mehrotra and Govil [16], Korol and Mansour [9], Korol and Mirza [10], Mang et al. [12], Davies ve PanjehShahi [4], Szlendak and Brodka [18], Brodka and Szlendak [2], Mashiri et al. [13], Szlendak [19], studied these subjects.

2. SPECIMENS

It is aimed to have a design algorithm and prevent local buckling at the assembly of welded square-profile column/beam. In that respect an assembly (β is 0.75) composed of D215, 1/5 mm circular column 150x200x4 mm square beam was tested. Some rigidity plates having different dimensional parameters were added at the assembly point to reach β=1.0. It is aimed to verify the combination of strong column / weak beam and rigid assembly under cyclical loading. Some experimental samples were tested. We endeavored to optimize the design and plate dimensions whereby the models used in the experimental analysis were extrapolated with the Ansys finite-element program [1]. There has been some undesirable local strain at square-profile assembly parts (column, beam, cross-diagonal) under the effect of bending. The placement and formation of strain affect the capacity of node-point ductility and rigidity. We strove to prevent the local stress at the assembly by using rigidity plates having different dimensional parameters or by changing the

location and formation of strain. The welded circular profile (D219, 1/5) column and rectangular (150x200x4 mm) beam were tested under the cyclical horizontal load. The general appearance and dimensional parameters regarding the experimental models are shown in Figure 3. The load was applied to the sample vertically and continuously, and the loading lever and strength conditions of the sample were designed in a hinged manner.

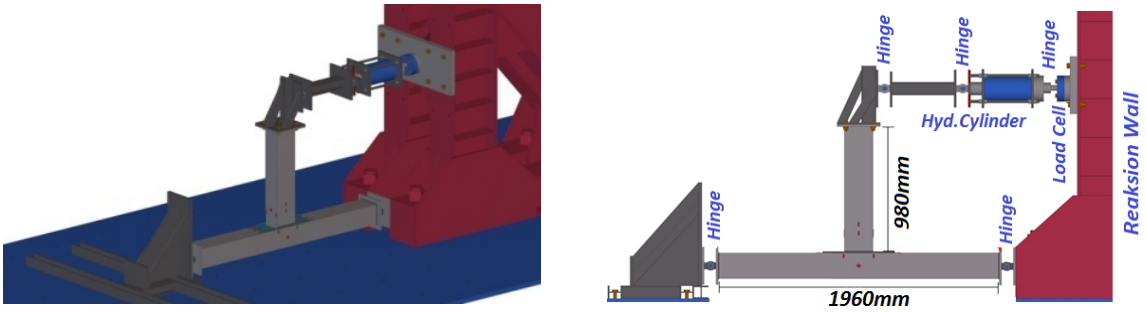

a) Experimental model general view **b)** Dimension of speciment&Loading System view

Figure 3. General view of experiment model

The dimensional parameters of the rigidity plate added to the column upper head at the assembly were based on alterations on length, width and wall thickness. In that respect there were ten experimental samples, including replicate samples and 37 digital models. The assembly of the column beam without a plate was connected by welding at the reference model of the replicate sample. Experimental samples with rigidity plate the thickness of the plate were consistently selected as 8 mm while the width and length values were changed. The number of models was increased in the digital models calibrated according to the experimental samples, each being designed for five different calculations of wall thickness. There are some variables of dimensional parameters for the rigidity plates submitted in Fig. 4.

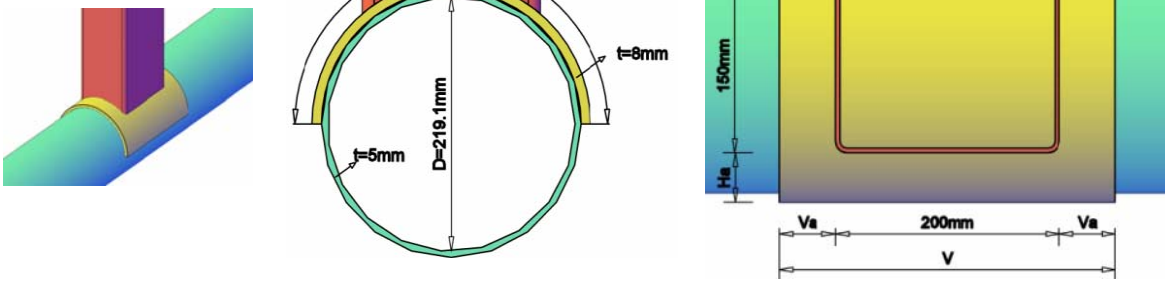

a) Node point general view

b) The view of dimensional parameter profile of the rigidity plate

c) The view of the plan of dimensional parameter for rigidity plate

Figure 4. The dimensional parameter for the of the rigidity plate-rigidity models

The change in length for the plates added to the assembly is identified as (V) and three main groups assigned as 300, 350 and 400 mm. There has been established three sub-parameters more by selecting the width (H) values are 250, 300 and 350 mm in every group below the length V. Experimental analysis has been conducted for 10 experimental models in total (nine are with the rigidity plate, and one is with no plate (replicate sample) for the 8-mm wall thickness. The models having conducted experimental analysis and the dimensional changes used for rigidity plates used at these models are detailed in Table 1.

Table 1. Plate Dimensions, Wall Thickness for Experimental Samples and the Names of Models

Line	Speciment No	Rijidity Plate Parameters				
		Va	Ha	V	H	ta
1	S 0	-	-	-	-	-
2	SP1-1/8	50	25	300	250	8
3	SP1-2/8	50	50	300	300	8
4	SP1-3/8	50	75	300	350	8
5	SP2-1/8	75	25	350	250	8
6	SP2-2/8	75	50	350	300	8
7	SP2-3/8	75	75	350	350	8
8	SP3-1/8	100	25	400	250	8
9	SP3-2/8	100	50	400	300	8
10	SP3-3/8	100	75	400	350	8

We endeavored to optimize the rigidity plate's wall thickness by analyzing the thickness in the limits of 5/6/10 mm in addition to 8 mm in the digital models calibrated according to the results of the experimental samples. The plate dimensions, wall thickness and names of the models used for all experimental and digital models are shown in Table 2.

Table 2. The plate dimensions, wall thickness and the names of the models

Code Name	Plate Size				Model Name		
	P1-1	P2-1	P3-1	t			
M	300/250	350/250	400/250	5	MP1-1/5	MP2-1/5	MP3-1/5
M	300/250	350/250	400/250	6	MP1-1/6	MP2-1/6	MP3-1/6
SM	300/250	350/250	400/250	8	SMP1-1/8	SMP2-1/8	SMP3-1/8
M	300/250	350/250	400/250	10	MP1-1/10	MP2-1/10	MP3-1/10
	P1-2	P2-2	P3-2	t			
M	300/300	350/300	400/300	5	MP1-2/5	MP2-2/5	MP3-2/5
M	300/300	350/300	400/300	6	MP1-2/6	MP2-2/6	MP3-2/6
SM	300/300	350/300	400/300	8	SMP1-2/8	SMP2-2/8	SMP3-2/8
M	300/300	350/300	400/300	10	MP1-2/10	MP2-2/10	MP3-2/10
	P1-2	P2-3	P3-3	t			
M	300/350	350/350	400/350	5	MP1-3/5	MP2-3/5	MP3-3/5
M	300/350	350/350	400/350	6	MP1-3/6	MP2-3/6	MP3-3/6
SM	300/350	350/350	400/350	8	SMP1-3/8	SMP2-3/8	SMP3-3/8
M	300/350	350/350	400/350	10	MP1-3/10	MP2-3/10	MP3-3/10
M (Numerical Model/Ansys), SM (Numerical&Experimental Model)							
Note: The notations in this table are the same as those used for all graphs and figures in the study.							

Analysis Workbench Version 14.0 was used in the analysis of the digital models. The digital models were resized so that the assembly parts (column, beam, rigidity plate) and loading instrument (load lever, strength conditions) could reflect the experimental samples exactly, and these digital models have been divided into their respective finite elements. On one hand, the welded assemblies have been identified as rigid, while on the other hand the connection between the rigidity plate-column upper head has been described as frictional in the context of numerical

analysis. The loading lever and strength points of the samples were modeled as having stable strength and single-way rotational latitude. The identification of model materials for numerical analysis was defined using the result of tensile testing in regard to the examples gathered from the samples. The stress/transformation graphs, obtained after the tensile test and the dimensions of example used in the tensile tests, are shown in Figure 5. (TS EN ISO [20], the "Metal materials, Tensile Test" standards, was used to determine the dimensions of samples for the tensile tests.)

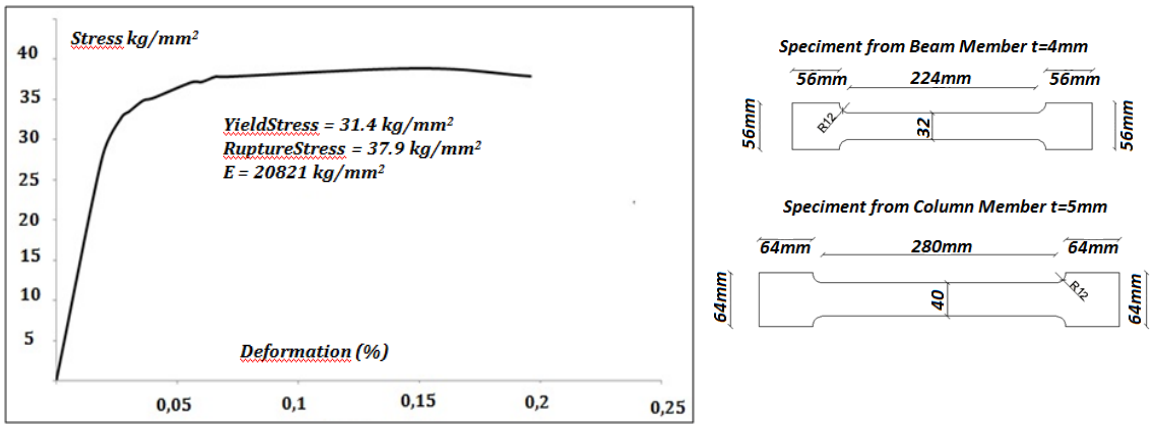

a) Stress/creep graph **b)** Sample dimensions

Figure 5. The results of the tensile test

3. RESULTS OF THE STUDY

The replicate sample (SO) was tested first to see the contribution of the rigidity plate added to the assembly in the study, whereby it could serve as a reference for other analyses. A local buckling occurred at the column upper head of the assembly location of the column/beam at the replicate sample under cyclical loading. The assembly could not have the behavior of the strong column / weak beam combination, and consequently creep occurred at the column first. For that reason no sufficiently rigid hinge or mechanism was found to be applicable to the assembly. Some views regarding the deformations at the replicate sample are shown in Figure 6. based on that figure, some local buckling was observed, originating from the corners of the beam at the column upper head, and the capacity of the system has been dramatically less than the theoretical capacity:

a) Local deformation at column upper head **b)** Local deformation at pressure location

Figure 6. The view of deformation of column upper head at replicate sample

The rigidity plate was used other than the replicate sample to prevent column deformation. It was used to prevent the local deformations that otherwise occurred on the column for all models modified with rigidity plates. Consequently, the rigidity of the node point increased and creep was observed at the beam instead of the column. The deformation under the bending effect at the beam

is a particular kind of mechanism, so the design principle of the strong column / weak beam was met. There are some views, demonstrating appearance after the load application, in Figure 7 regarding the experimental samples having a fixed wall thickness but different dimensional parameters.

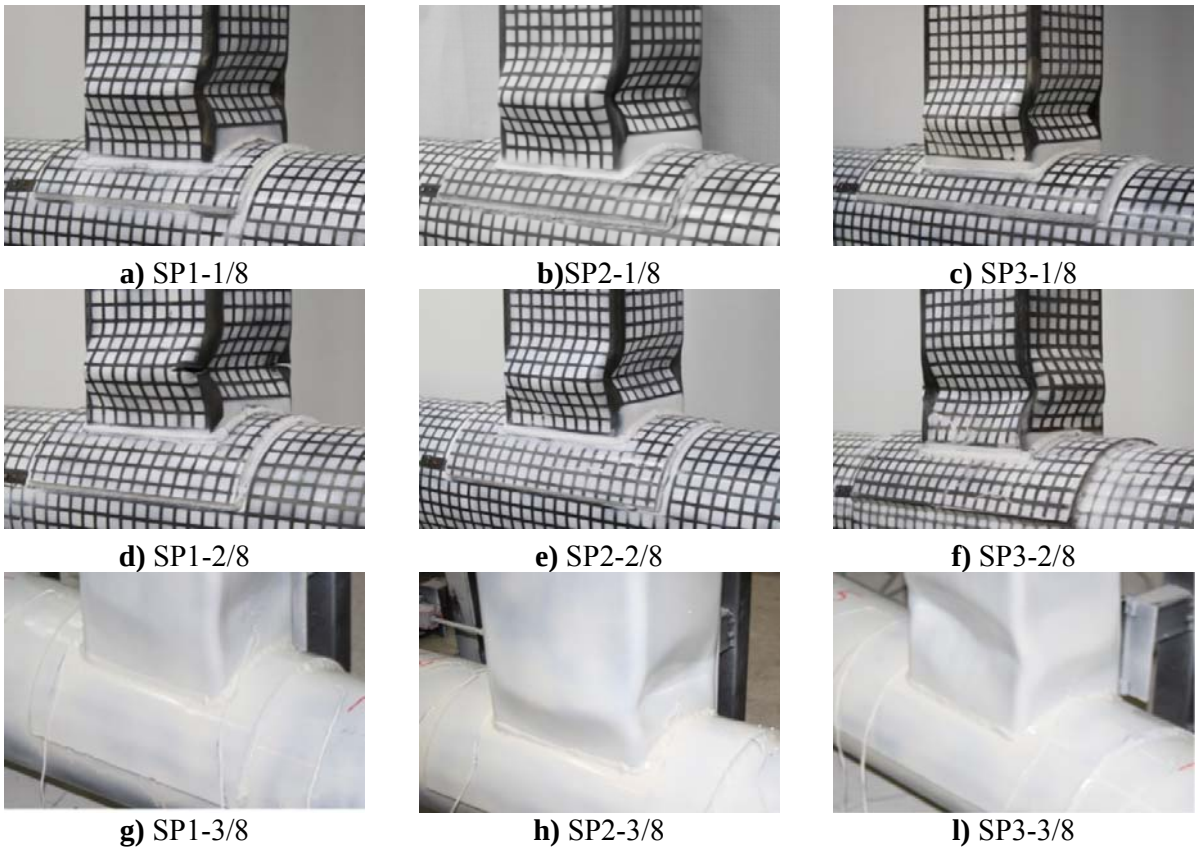

a) SP1-1/8 **b)**SP2-1/8 **c)** SP3-1/8

d) SP1-2/8 **e)** SP2-2/8 **f)** SP3-2/8

g) SP1-3/8 **h)** SP2-3/8 **l)** SP3-3/8

Figure 7. Deformation on the column after loading at some models.

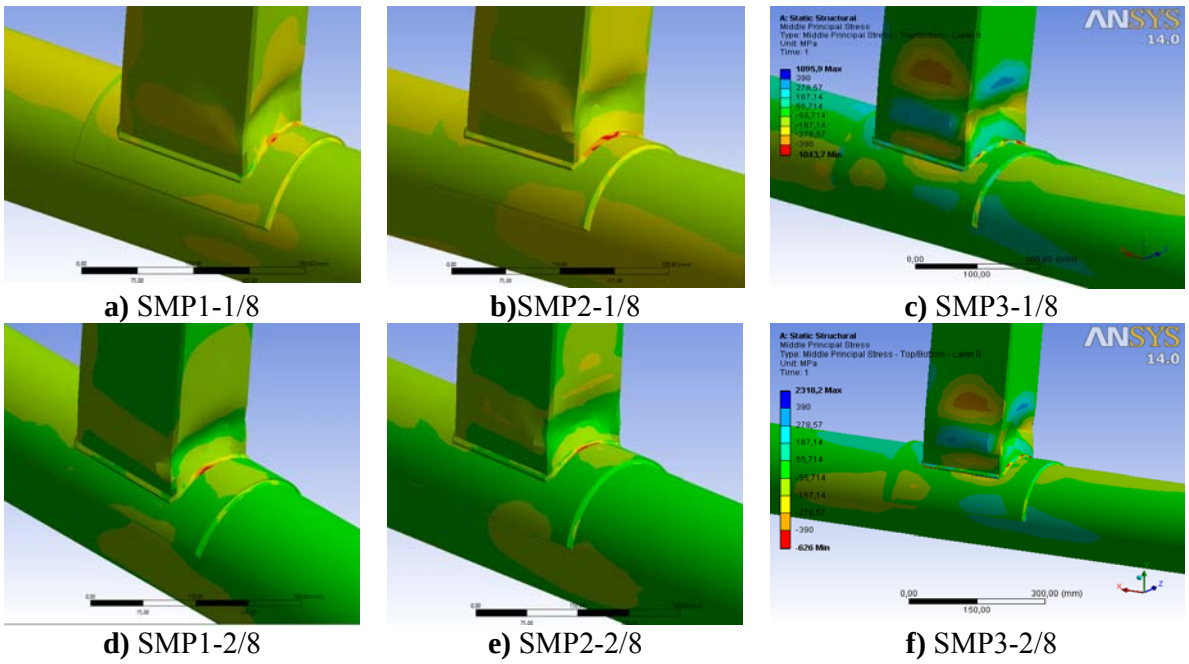

a) SMP1-1/8 **b)**SMP2-1/8 **c)** SMP3-1/8

d) SMP1-2/8 **e)** SMP2-2/8 **f)** SMP3-2/8

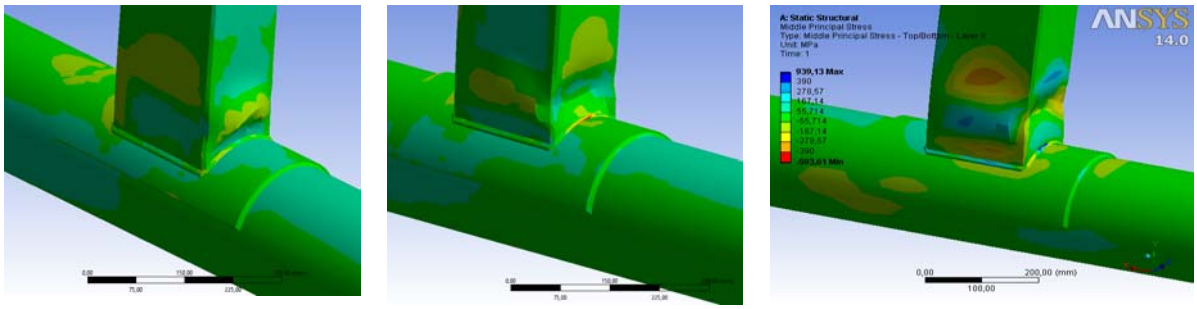

g) SMP1-3/8 **h)** SMP2-3/8 **l)** SMP3-3/8

Figure 8. Deformation on the joint after loading at numerical models.(ANSYS Work Bench)

It could be seen that the increase in the "V" and "H" values affects the formation and the location of the hinge on the beam after the review of the figures. The deformation on the beam at the samples with P1 (1, 2, 3), P2 (1, 2, 3) plates is concave at the head and convex at the body. However, it has been observed that the samples SP3-2/8 and SP3-3/8, having the maximum lengths of "V" and "H," departed from the node point by sliding and that the resulting deformation was convex at the head of the beam but concave at the body. A similar situation was identified in the digital models analyzed for those samples. The situation could be explained whereby the column rigidity increases in parallel to the increase in the length of the plate, causing the stress on the beam to play a more active role in creep.

The load-displacement graphs attained from experimental analysis are submitted in Figure 8. The comparative graphs have been established according to the dimensions of the rigidity plate used with the samples. The width of the plate is 250 mm (fixed), while the length "V" has some alteration values of 300, 350 and 400 mm in the graphs in Figure 8. This fixed-width value is the thinnest among the variations used in this study. It was observed that all the samples achieved a nearly twofold capacity increase, far exceeding the reference value in regard to capacity with rapid change, depending on the mechanism at the beam. It was also identified that while the contribution of the rigidity plates to rigidity and capacity gives very similar results, the model with the shortest plate P1(300/250/8) gave the peak value. The same situation is observed at the graphs in Figure 8b and c. The width of the plate is 300 mm in Figure 8b, and the widest plate (350) is in Figure 8c. The increase in the width of the plate, affecting the wrapping effect surrounding the column, did not contribute to the capacity in any significant degree. While plates P1 and P2 with a wall thickness of 5 mm could reach the others, plate P3 with a 5 mm wall-thickness value gave a dramatically different result in the condition whereby the wall thickness was reviewed together with the length and thickness.

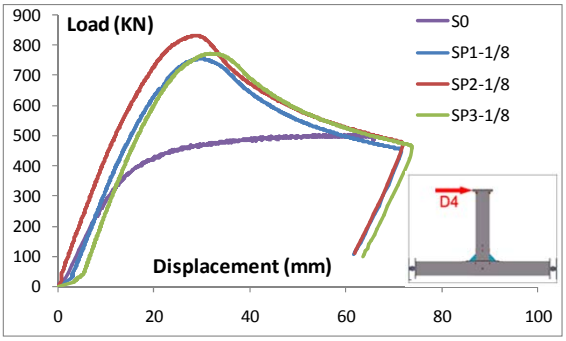

a) SP1, 2, 3-1(8)

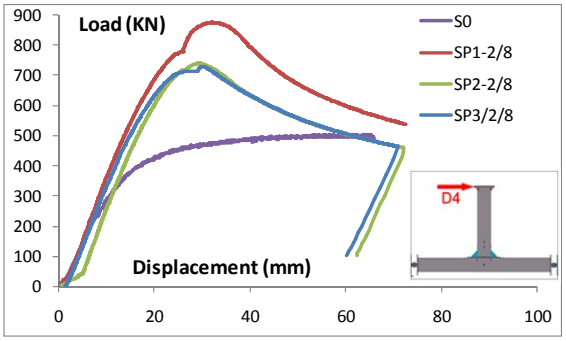

c) SP1, 2, 3-3(8)

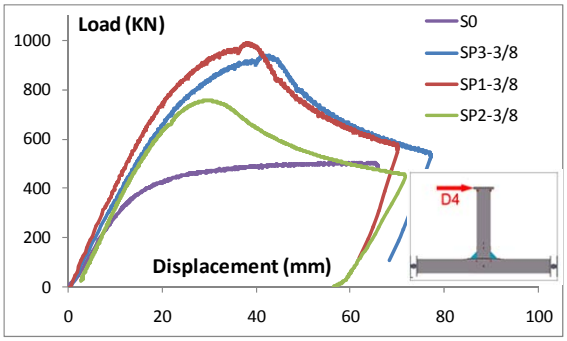

b) SP1, 2, 3 -2(8)

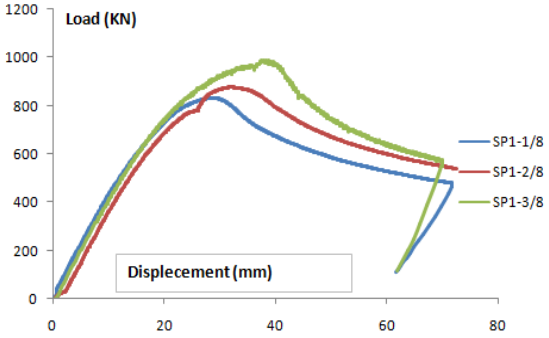

d) SP1-1/2/3(8)

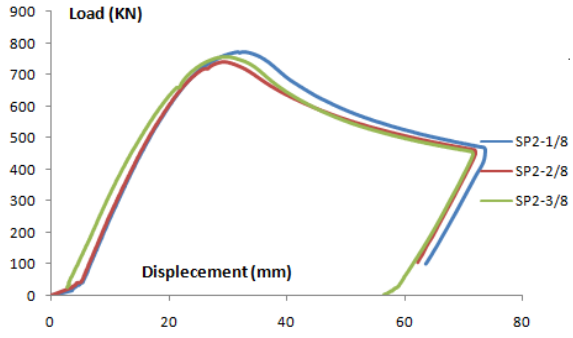

e) SP2-1/2/3(8)

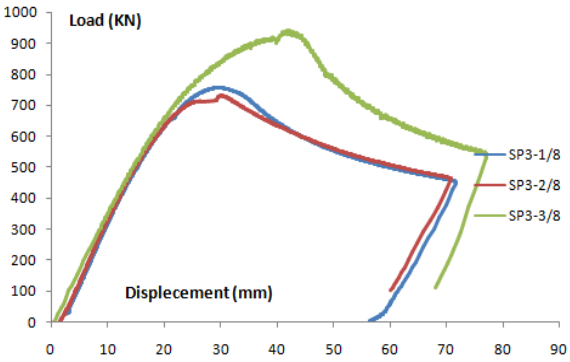

f) SP3-1/2/3(8)

Figure 8. The comparison of capacity graphs regarding the experimental models of groups 1, 2 and 3.

The number of model has been increased and there has been a change only in the wall thickness of the rigidity plate (5/6/8/10 mm) by fixing the dimensional parameters for all models for which experimental analysis was completed. The load-displacement graph derived from the results of analysis is shown in Figure 9. The blue-colored curves (dashed line) denote experimental analysis, the red colored curves (dashed line) denote numerical analysis regarding that experiment. Based on the graph, the data obtained from digital models has conformity with the experimental models. The alterations of wall thickness/capacity for all dimensions and the behaviors of node points were not changed by excluding the dimensions of plates P3-2 and P3-3 from the numerical analysis or experimental analysis. Only the wall thickness of 5/6 mm at plates with the greatest dimensional parameters gives a different result. Even in this situation there has been a mechanism at the beam, and consequently creep has been prevented.

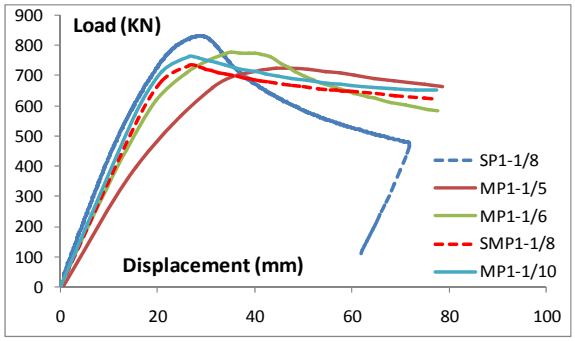

a) P1-1/5-6-8-10

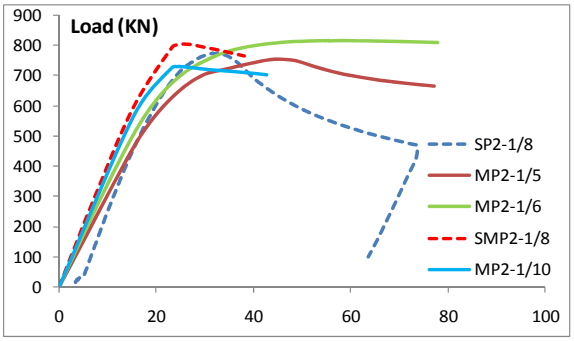

b) P2-1/5-6-8-10

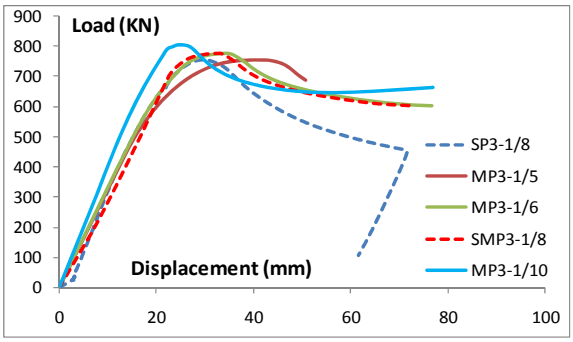

c) P3-1/5-6-8-10

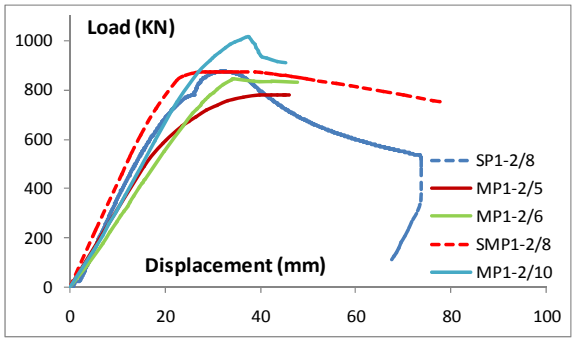

d) P1-2/5-6-8-10

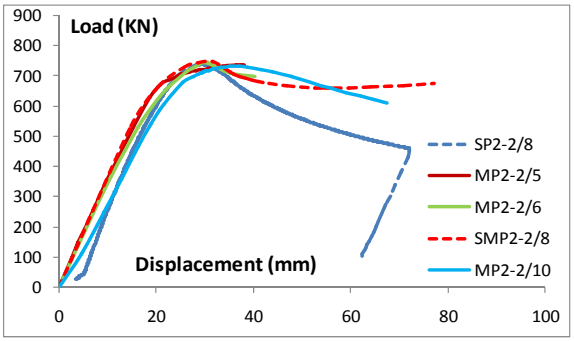

e) P2-2/5-6-8-10

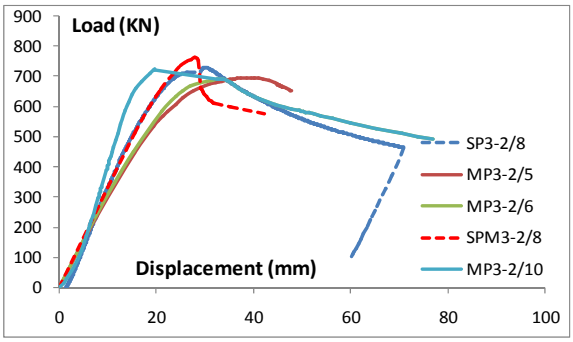

f) P3-2/5-6-8-10

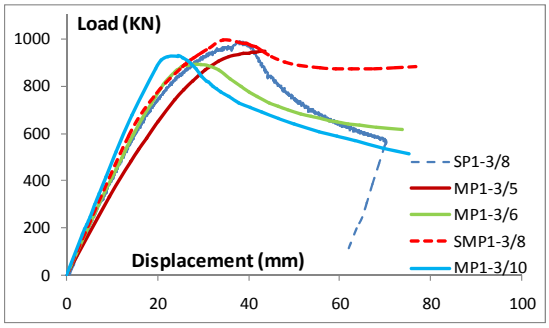

g) P1-3/5-6-8-10

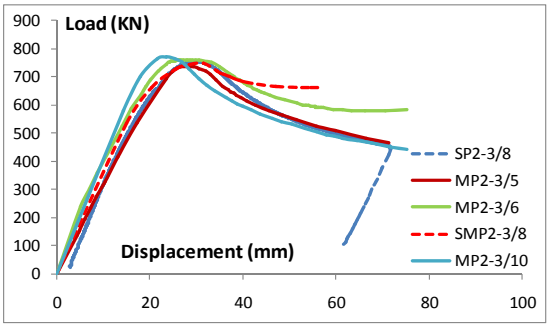

h) P2-3/5-6-8-10

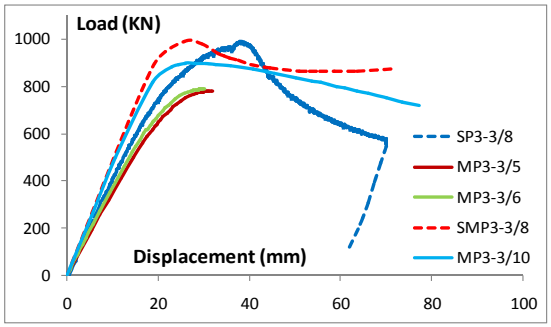

ı) P3-3/5-6-8-10

Figure 9. Comparison of capacity graphs regarding the experimental and digital models of groups 1, 2 and 3

We obtained increases in capacity, ductility and rigidity at the assembly with the addition of a rigidity plate to the assembly. The rigidity alterations of experimental and digital models are shown in Figure 10. There is a comparison of rigidity, depending on the alterations of dimensional and wall thickness of plates P1, P2 and P3 in Figure 10a, b and c. There is also another comparison of rigidity with some alterations in the values of width and the fixed values of the lengths of plates P1, P2 and P3 in Figure 10d, e and f. It is observed that the same rigidity values are obtained with the same wall thickness at plate P1 for the width of 250 and 300 mm, but there is an increase in the rigidity values for the width of 350 mm. The maximum results have been obtained at the narrowest profile of 250 mm at plate P2. However, while the values obtained from 350 mm at plate P3 seem greater, a significant difference was not obtained. Thus, the rigidity changes were stable at the same values for the same wall thickness. The increase in wall thickness, excluding some extraordinary situations, gives results in parallel to this increase in terms of wall thickness. There is a comparison regarding the effect of the length alterations on the rigidity node point for the same width values of plates P1, P2 and P3, as shown in the graphs of Figure 10d, e and f. We found that the deformation in length made a positive contribution to rigidity, as shown in the graphs, and that the width of the rigidity plate has been fixed while varying the length. The rigidity has been increased in parallel with the alteration in wall thickness.

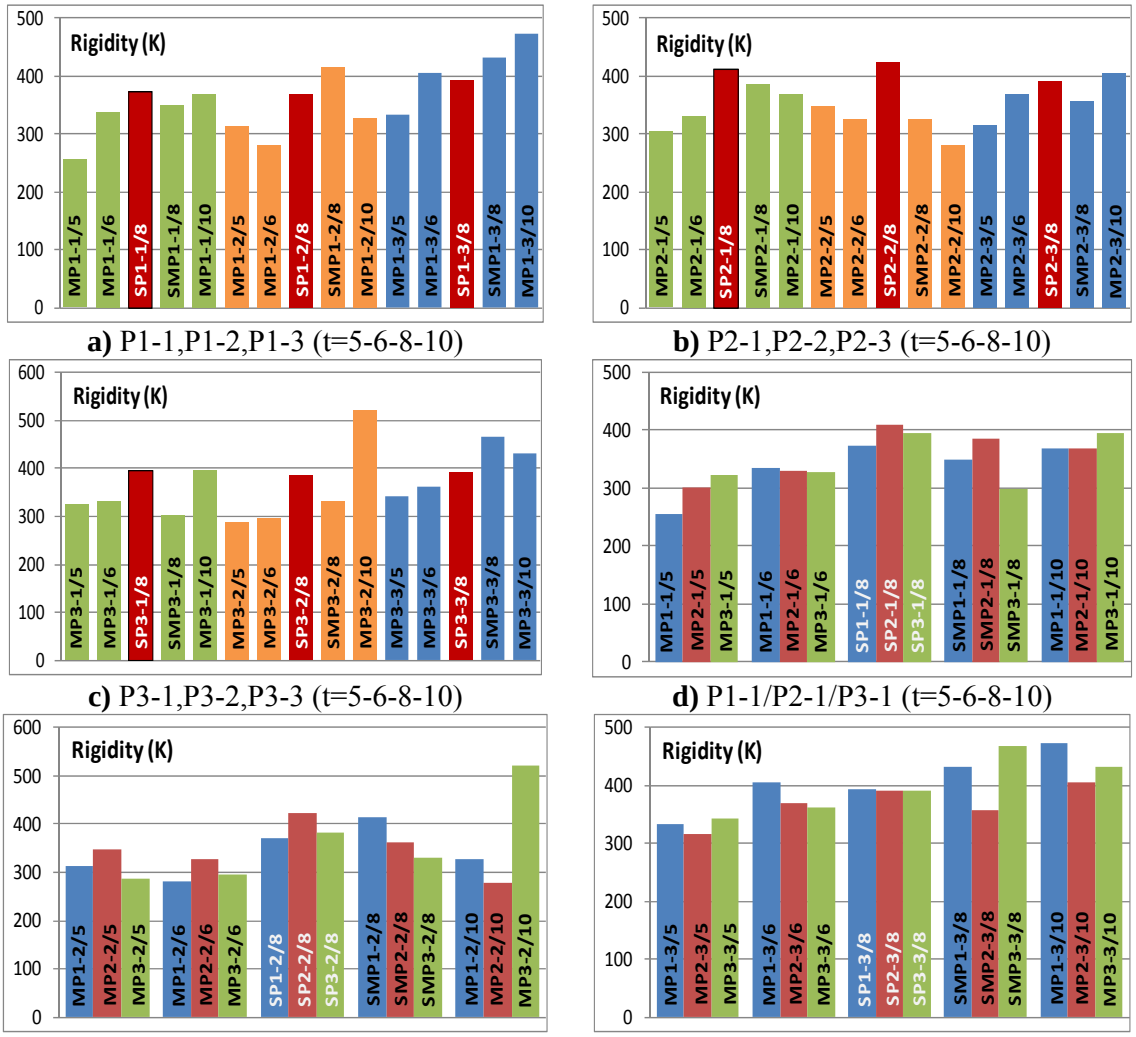

a) P1-1,P1-2,P1-3 (t=5-6-8-10) **b)** P2-1,P2-2,P2-3 (t=5-6-8-10)

c) P3-1,P3-2,P3-3 (t=5-6-8-10) **d)** P1-1/P2-1/P3-1 (t=5-6-8-10)

e) P1-2/P2-2/P3-2 (t=5-6-8-10) **f)** P1-3/P2-3/P3-3 (t=5-6-8-10)

Figure 10. Comparison of rigidities regarding the experimental and digital models of groups 1, 2 and 3.

4. RESULTS AND CONCLUSIONS

The replicate sample and the models with rigidity plates were reviewed from their experimental and numerical aspects. The rigidity plate has been used to prevent the effects of local buckling on the column at this assembly under bending effect. It has been tried to increase the capacity and rigidity of the node point through changes in the dimensions of the plate. The samples, analyzed in that respect, were divided into three main groups in terms of the rigidity plate used, and each group was divided into three sub-models in terms of plate width. Thus there were three models having P1 (Length V=300 mm) H=250/300/350 mm. We analyzed a total of 10 samples experimentally, including the replicate sample. There were three models having P1 (Length V=300 mm) H=250/300/350 mm, three models having P2 (V=350 mm) 250/300/350 mm and three models having P3 (V=400 mm) 250/300/350 mm. All the models were subjected to experimental analysis. The number of models, however, was extended through the use of alterations (t=5/6/8/10 mm) in the width of the plate by fixing the plate dimensions for all models prior to experimental analysis. A parameter was included in the study by reviewing the effect of wall thickness on behavior. The

plate, added to the assembly, was reviewed in terms of length (V), width (H) and wall thickness (t), and the effect of each plate on the capacity and rigidity of the assembly was examined.

It was observed that the rigidity panels added to the assembly made positive contributions to the capacity, as demonstrated by all the capacity graphs obtained through experimental and numerical analyses. The most significant increase in capacity was obtained from plate P1 in Figure 10a, b and c, thereby demonstrating the alteration of capacity according to the fixed width and alterations in length. The rigidity plates were attached to the column by welding across the plate edges. For that reason, while the plates under the bending effect deformed with the column under pressure, the plates were forced to creep apart from the surface of the column. Consequently, the more the plate was extended, the more the potential for deformation increased. The capacity and rigidity were affected in a negative way.

Additionally, the cross-height was used as a parameter to increase the effect of wrapping on the column and to limit this situation in the freedom of deformation. The coverage area on the column was increased by choosing the width values of 250 mm, 300 mm and 350 mm. The change in capacity for the number P3-3 (V=400 mm; H=350 mm) with maximum width was increased 30% in comparison with the models of "H" value (250 and 300 mm) in the situation using the longest plate P3, while the contribution of increase in width to the capacity at plates P1 and P2 did not change significantly. It was identified that the creep (despite not being visible to the naked eye) for the models used plates P1 and P2 with the lengths of 300 and 350 mm by reviewing the figures at the plate edges, thus reaching the plastic area, and that the decline reached a level beyond the linear limit. For that reason the rigidity of the node point decreased and then the increase of capacity reached its limit. However, for the model that used the longest plate in terms of height and width, the situation of expanding the stresses on the column to the larger area helped keep the stresses within the linear limits. In that respect, the loss of capacity and the rigidity were not experienced and the mechanism on the beam was identified as an alteration of capacity.

Another reason for the increase in capacity is that the circular profile column’s reaction to the reversible loads was equal and continuous, depending on the specifications of the column profile. However, the variable behavior of the plate added to the assembly under the effect of pressure and tensile strength changed the reaction of the column. Thus the increase of the wrapping effect on the column of the plate limited the deformation and stress on the plate and the column under the reversible loads and helped keep the stress within the linear limits by using the advantages derived from the profile geometry of the circular column.

Additionally, the increase in the wrapping effect of the plate identified the location of hinge on the beam. For some conditions in which plates P1, P2 and P3-1/2 were used, the distance from the hinge to the node point was 40, 50 or 60 mm. The increase in capacity can be explained by the value of 90 mm for plate P3-3.

Numerical analysis revealed the effect of wall thickness on the capacity of the node point, rigidity and behavior. The increase in the rigidity of the column was accomplished, resulting in a mechanism at the beam for all the models under cyclical loading (i.e., the models to be prepared for all plate dimensions). When certain results are excluded, the capacity values are in parallel. The loss of capacity on the beam with t-values of 8 mm and 10 mm resulted in the rapid loss of load, as shown in the graphs. However, in some analyses in which the t-values were 5 and 6 mm, the curve gave greater absorption and smooth results. The capacity alterations of the models having wall thickness of 5 or 6 mm at P3-3 are different from the others. It has been observed that a wall thickness of 5 mm or 6 mm has not been sufficient in comparison with the others in the situation with the plate length (400 mm) at the assembly modified through the use of a plate.

Rigidity plate that are used in preventing the local buckling in column member. In literature dimentional parameters of this plate are defined in terms of width and wall thickness that are related with dimentional of connection members. Such as According to design codes; width of plate sholud be equal to twice diameter of column and also thicnes of plate should be equal to twice web thicnes of beam. As shown the parameters are connected to one value. In this study; accordıng to the results; parameters were defined based on a range rather than a single value . our range of dimentional parameters are shwed as follows.

If it is preferable to overcome the local deformations using rigidity plate at this type of assembly, in light of the data gathered through experimental and numerical analysis:

- The length V_b for the plate should be at the interval of $0{,}25V_b \le V_p \le 0{,}5V_b$;
- If V_p length is $0{,}25V_b \le V_p \le 0{,}375V_b$ then wall thickness is tc ≤ t ≤tb, The width of the plate H should be selected from the interval of 2r≤H≤πr (r is radius for the column); and
- If the length V_p of plate $V_p = 0{,}5V_b$ then it is offered that the wall thickness is t ≥ 2tb and H value (the width of the plate) is H=πr.

REFERENCES

[1] ANSYS 14.0 Workbench [Computer software]. Canonsburg, PA, Ansys.

[2] Brodka, J. and Szlendak, J., “Strength of Cross Joints in Rectangular Hollow Sections”, In XXVI Scientific Conference of the Civil and Hydraulic Engineering Section of the Polish Academy of Science and of the Science Division of PZITB, 1980.

[3] Cute, D., Camo, S. and Rumpf, J.L., “Welded Connections for Square and Rectangular Structural Steel Tubing” In Research Report No. 292-10, 1968, Drexel Institute of Technology Philadelphia, PA.

[4] Davies, G. and Panjehshahi, E., “Tee Joints in Rectangular Hollow Sections (RHS) under Combined Axial Loading and Bending” In 7th International Symposium on Steel Structures, 1984.

[5] Design Guide 3, For Rectangular Hollow Section (Rhs) Joints Under Predominantly Static Loading. Comité International Pour Le Développement Et L’étude De La Construction Tubulaire, 2009.

[6] Duff, G., “Joint Behaviour of a Welded Beam-column Connection in Rectangular Hollow Sections” (Doctoral dissertation, The College of Aeronautics Cranfield, UK), 1963.

[7] Eurocode 3, Design of Steel Structures - Part 1-8: Design of Joints, European Committee for Standardization, Brussels, 2003.

[8] Hwang, W. S., Kim, Y. P. and Yoon, T. Y., “Central Angle Effect on Connection Behavior of Steel Box Beam-to-circular Column” Structural Engıneerıng and Mechanıcs, 2009, Vol. 32, No. 4, pp. 531-547.

[9] Korol, R. M. and Mansour, M. H., “Theoretical Analysis of Haunch-reinforced T-joints in Square Hollow Sections” Canadian Journal of Civil Engineering, 1979, Vol. 6, No. 4, pp. 601-609.

[10] Korol, R. M. and Mirza, F. A., “Finite Element Analysis of RHS T-joints” Journal of the Structural Division, 1982, Vol. 108, No. 9, pp. 2081-2098.

[11] Lazar, B. E. and Fang, P. J., “T-type Moment Connections between Rectangular Tubular Sections” In Research Report, Sir George Williams University Montreal, 1971.

[12] Mang, F., Bucak, O. and Wolfmuller, F., “The Development of Recommendations for the Design of Welded Joints between Steel Structural Hollow Sections (T-and X-type joints).”

In Report on ECSC Agreement 7210 SA/109 and CIDECT Program 5AD Final Report. University of Karlsruhe Federal Republic of Germany, 1983.

[13] Mashiri, F.R., Zhao, X. L. and Grundy P., "Stress Concentration Factors and Fatigue Behavior of Welded Thin - Walled CHS-SHS T-Joints Under In-Plane Bending." Engineering Structural 2005, Vol. 26, pp. 1861-1875.

[14] Mashiri, F.R. and Zhao, X. L., "Plastic Mechanism Analysis of Welded Thin-Walled T-Joints Made Up Of Circular Braces And Square Chords Under In-Plane Bending." Thin-Walled Structures, 2004, Vol. 42, pp. 759–783.

[15] Mehrotra, B. L. and Redwood, R. G., "Load Transfer through Connections between Box Sections", Canadian Eng. Instn., C-70-BR and Str, 10, 1970.

[16] Mehrotra, B. L. and Govil, A. K., "Shear Lag Analysis of Rectangular Full-Width Tube Junctions" Journal of the Structural Division, 1972, Vol. 98, No. 1, pp. 287-305.

[17] Redwood, R. G., "The Behaviour of Joints between Rectangular Hollow Structural Members" Civil Engineering and Public Works Review, 1965, Vol. 60, No. 711, pp. 1463-1469.

[18] Szlendak, J. and Brodka, J., "Technıcal Note. Strengthening Of T Moment Of RHS Joints" In ICE Proceedings, Thomas Telford, 1985, Vol. 79, No. 4, pp. 717-727.

[19] Szlendak, J., "Beam-column Welded RHS Connections", Thin-walled Structures, 1991, Vol. 12, No. 1, pp. 63-80.

[20] TS EN ISO 6892-1, "Metallic Materials – Tensile Test – Volume 1 : Test Method at ambient Temperature", The Turkish Standards Institution, 2010.

[21] Wang, W. D., Han, L. H. and Uy, B., "Experimental Behaviour of Steel Reduced Beam Section to Concrete-filled Circular Hollow Section Column Connections", Journal of Constructional Steel Research, 2008, Vol. 64, No. 5, pp. 493-504.

[22] Wardenier, J., "Hollow Section Joints" (Doctoral dissertation, TU Delft, Delft University of Technology), 1982.

[23] Zhao, X. L., "Deformation Limit And Ultimate Strength Of Welded T-Joints In Cold-Formed RHS Sections", Journal of Constructional Steel Research, 2000, Vol. 53, pp. 149–165.

EXPERIMENTAL EVALUATION OF TIE BAR EFFECTS ON STRUCTURAL BEHAVIOR OF SUSPENDED SCAFFOLDING SYSTEMS

Barış Sevim *, Serkan Bekiroglu and Güray Arslan

Yıldız Technical University, Department of Civil Engineering, 34220, İstanbul, Turkey
**(Corresponding author: E-mail: basevim@yildiz.edu.tr)*

Received: 11 November 2015; Revised: 23 March 2016; Accepted: 26 March 2016

ABSTRACT: The collapse of scaffolds can bring about substantial damage and economic loss. In recent years, over hundreds of people died and an even greater number have been injured because of inadequate scaffolding system designs. In this study, the effects of truss height and number of tie bars on the structural behavior of suspended scaffolding systems were experimentally investigated. Three full-scale scaffolding systems with truss heights of 30, 45, and 60 cm were tested in the laboratory. Each system included a wooden floor, steel purlins and trusses. The number of steel tie bars connected to the systems was also varied. A load transmission system was placed in these experimental systems to distribute single loads to the center of a specific area in a step-by-step manner using a load jack. After each load increment, the displacement was measured by means of linear variable differential transducers placed at critical points of the wooden floor, purlins, and trusses. This test was repeated for all systems and under all system conditions. The test results revealed that displacement increased exponentially in scaffolds with truss heights of 30, 45, and 60 cm without tie bars. Under the same load, systems with truss heights of 60, 45, and 30 cm revealed displacements of 8.8, 12.1, and 23.3 cm, respectively. The results of this work demonstrate that the number of tie bars and truss height considerably affect the structural behavior of scaffolding systems. Our findings further suggest that a scaffolding system with 60 cm-high truss and two tie bars presents optimal safety and cost-savings.

Keywords: Laboratory model, Load-displacement curve, Load transmission platform, Suspended scaffolding system, Tie bar effects, Truss height

DOI: 10.18057/IJASC.2017.13.1.4

1. INTRODUCTION

Recent developments in technology have allowed possible the construction of various structural systems such as bridges, dams, tunnels, and multi-story buildings. To complete the construction of these systems, workers, building materials, work instruments, and other devices must be carried from the ground to higher levels. Scaffolding systems are temporary structures erected around a construction site to provide a safe working environment to workers and carry tools upward from the ground level. Several scaffolding types have been developed according to a number of site requirements. The most common scaffolds include supported platform systems, adjustable scaffolding systems, and suspended scaffolding systems. Supported scaffolding systems are made of wood and metal structures supported by poles and frames fixed to ground. Adjustable scaffolding systems are raised and lowered using pulleys. Suspended scaffolding systems are platforms suspended from the top of a building using ropes (Url-1). When choosing a scaffolding type, several factors such as the condition of the ground over which the scaffold will be erected and the project design, budget, and schedule must be considered. For example, if the ground around the construction site is unstable or if the scaffold to be erected will prohibit access to other parts of the structure being built, a suspended scaffolding system may be best. A suspended scaffold is relatively safer than a platform that is dozens of stories high (Figure 1 (Url-1a-g [1]). A supported platform scaffold can provide excellent flexibility for tall buildings, Url-2 [2]).

Figure 1. Practical Uses of Suspended Scaffolding Systems (Url-1a-g [1])

Scaffolding systems are mainly made of wood and metal. The wood is obtained from trees such as pine, poplar, and willow, and the metal elements usually include aluminum, galvanized steel, and composite materials. The metal components of scaffolds are generally formed as frames or tubes. These elements are manufactured according to the desired length and connected or tied to each other to construct to scaffold. Scaffolds also require couplers and planks; the couplers connect the elements and the planks make up the working platform. These planks can be made of wood or metal (Url-3 [3]).

Damage to property, personal injury, and death may result from poorly designed scaffolds or non-observance of routine precautions. For example, according to a report by the United States Bureau of Labor Statistics, in 2007, 88 fatalities occurred from scaffolds. A recent study found that 72% of the injuries suffered in scaffold accidents could be traced back to the support giving way or the worker slipping through the scaffold frame or being struck by a falling object. In the United Kingdom, about 50 people die each year because of scaffold collapse and over 4,500 workers have been injured by faulty or defective scaffolds. (Collins et al. [4]; Url-4 [5]). Thus, the structural safety of scaffolding systems must be investigated and precautions must be taken during the construction and operation of these systems.

The importance of scaffold safety was highlighted in previous studies, such as those of Peng et al. [6-7]. In their first study, these authors focused on the development of a computer model based on actual construction practices to provide a description of the likely causes of scaffold support system collapse during construction. An examination of the effect of the combination of wooden shores with modular steel scaffolds on the performance of temporary support structures then followed. In their second study, the authors presented a simplified structural analysis procedure for high-clearance scaffolding systems based on a “set” concept. The validity of this simplified procedure was then confirmed by comparing results with the more refined computer model developed in their first study. Figure 2 shows the aftermath of the collapse of suspended scaffolding systems (Url-5a-g [8]).

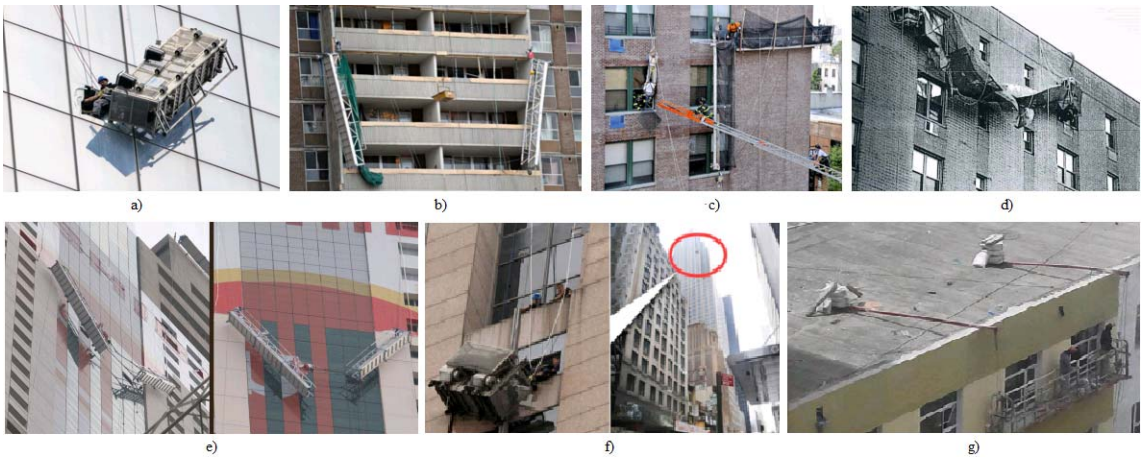

Figure 2. Collapse of Suspended Scaffolding Systems (Url-5a-g [8])

Recent years have shown an increase in research on scaffolding safety (Khudeira [9]; Pishes et al. [10]). Hill et al. [11]) studied the design of suspended-scaffold structural support elements and lifeline anchorages according to federal OSHA requirements. Chuyang and Luli [12] researched the finite element model of a scaffolding system to determine the influence of joint stiffness on the overall stiffness of the scaffold and load distribution at the bottom of bowl scaffolds. Romera et al. [13] observed that many construction accidents are caused by deficiencies in the project design phase. Beale [14] published a review of scaffolding and falsework structures performed over the last 40 years; this review also discussed the finite element modeling and testing procedures of scaffolds and provided recommendations for modeling connections and different loads on scaffolding systems. Kim and Teizer [15] developed a rule-based system that could automatically plan scaffolding systems for pro-active management in building information modeling.

Studies related to the analysis and design of scaffolding systems have been performed by many researchers. Peng et al. [16] analyzed the structures and models of scaffolding systems used in construction. Prabhakaran [17] performed nonlinear analysis of scaffolds with semi-rigid connections. Son and Park [18] investigated the structural behavior of steel-pipe scaffoldings based on the tightening strength of clamps using MIDAS structural analysis software. Chandrangsu [19] performed an advanced analysis and probabilistic-based design of support scaffolding systems. Chandrangsu and Rasmussen [20] developed three-dimensional advanced analysis models to determine the behavior of support scaffolding systems; this study also described the methods for modeling spigot joints, semi-rigid upright-to-beam connections, and base-plate eccentricities. Prabhakaran et al. [21] developed an algorithm to model scaffold behavior and study the full moment-rotation curve including nonlinear loading and unloading behavior; here, different approximations of the moment–rotation curves were presented and applied to simple frames. Yue and Yuan [22] developed design methods of integral-lift tubular steel scaffolds for high-rise building construction; in this study, dead loads, live construction loads, and wind loads for integral-lift scaffolds were presented. Zhang and Rasmussen [23] investigated the behavior of steel scaffold structures using advanced analytical tools by considering system-based designs. Experimental studies have also been performed by several researchers (Chandrangsu and Rasmussen [24]; Liu et al. [25]; Peng et al. [26]; Andre et al. [27]; Peng et al. [28].

Considering the importance of scaffold safety and the lack of literature to describe it, more experimental studies must be done to investigate the structural behavior of scaffolding systems to decrease the risk of accidents caused by design deficiencies. The present study evaluates the structural behavior of scaffolding systems subjected to several loading tests. First, the general requirements to design and construct scaffoldings are provided. Then, the test procedure and

scaffolding systems constructed in the laboratory are described. Afterward, loading tests are performed on suspended scaffolding systems with different numbers of tie bars at three different truss heights, and the results of these tests are reported. Finally, this paper summarizes the considerable effects of number of tie bars and truss height on the structural behavior of scaffolding systems.

2. GENERAL REQUIREMENTS FOR SUSPENDED SCAFFOLDING SYSTEMS

The United States Occupational Safety and Health Administration (OSHA3150 [29]) has provided general requirements and guidelines for constructing suspended scaffolding systems. According to OSHA3150, each suspended scaffold and scaffold component must support its own weight and at least four times the maximum intended load applied or transmitted to it without failure. Also, scaffolds and scaffold components must not be loaded in excess of their maximum intended load or rated capacity, whichever is less. Load-carrying timber members should be a minimum of 10.34 kN/m^2 construction-grade lumber, and, during construction, each platform must be planked and decked as completely as possible with a space between the platform and uprights of not more than 2.5 cm wide. This space must not exceed 24.1 cm when side brackets or odd-shaped structures result in a wider opening between the platform and the uprights, and the platform deck must not deflect by more than 1/60 of the span when loaded.

Suspended scaffolding systems contain one or more platforms suspended by ropes or other non-rigid means from an overhead structure; some examples of these scaffolds include the single-point, multipoint, multi-level, and two-point adjustable scaffolds. In these systems, all of the support devices must rest on surfaces capable of supporting at least four times the load imposed on them. When scaffold platforms are more than 61 cm above or below a point of access, ladders, ramps, walkways, or similar surfaces must be used. When lanyards are connected to horizontal lifelines or structural members on single-point or two-point adjustable scaffolds, the scaffold must have additional independent support lines equal in number and strength to the suspension lines, and these support lines must have automatic locking devices. Counterweights used to balance adjustable suspension scaffolds must be able to resist at least four times the tipping moment imposed by the scaffold operating at either the rated load of the hoist or one and a half (minimum) times the tipping moment imposed by the scaffold operating at the stall load of the hoist, whichever is greater. A single tieback must be installed perpendicular to the face of the building or structure. Two tiebacks installed at opposing angles are required when a perpendicular tieback cannot be installed. The suspension ropes must be long enough to allow the scaffold to be lowered to the level below without the rope passing through the hoist, and the end of the rope must be configured to prevent the end from passing through the hoist. Suspension ropes supporting adjustable suspension scaffolds must be of a diameter large enough to provide a surface area sufficient for installing brake and hoist mechanisms (OSHA3150 [29]).

3. EXPERIMENTAL TESTS OF THE SUSPENDED SCAFFOLDING SYSTEMS

3.1 Description of the Scaffolding Systems

The effects of different tie bar numbers on the structural behavior of suspended scaffolding systems were experimentally determined. Three full-scale 3D steel pipe-rack suspended scaffolding systems with different truss heights were constructed in our laboratory for this test. Each scaffold was built with two plane trusses impended on two plane frame systems (Figure 3). The height of the trusses of the first, second, and third scaffold was 30, 45, and 60 cm, respectively. These systems were named

T30, T45, and T60, respectively. The plane trusses of all three scaffolds were connected with purlins over which a wooden board was placed. The frame systems of these scaffold were not fixed to the soil, but the beam and column elements of these frames featured rigid connections. The purlins were connected to the plane trusses via pins; trusses were also connected to the frame system via pins. The connections of the system were provided by 48/48 swivel couplers and girder gravlock clamps. The wooden boards were placed on the purlins without fixing. The span width and length of the scaffoldings were 1.6 and 6 m, respectively, and the outer diameter and pipe thickness of the trusses were 48.3 and 3.2 mm, respectively.

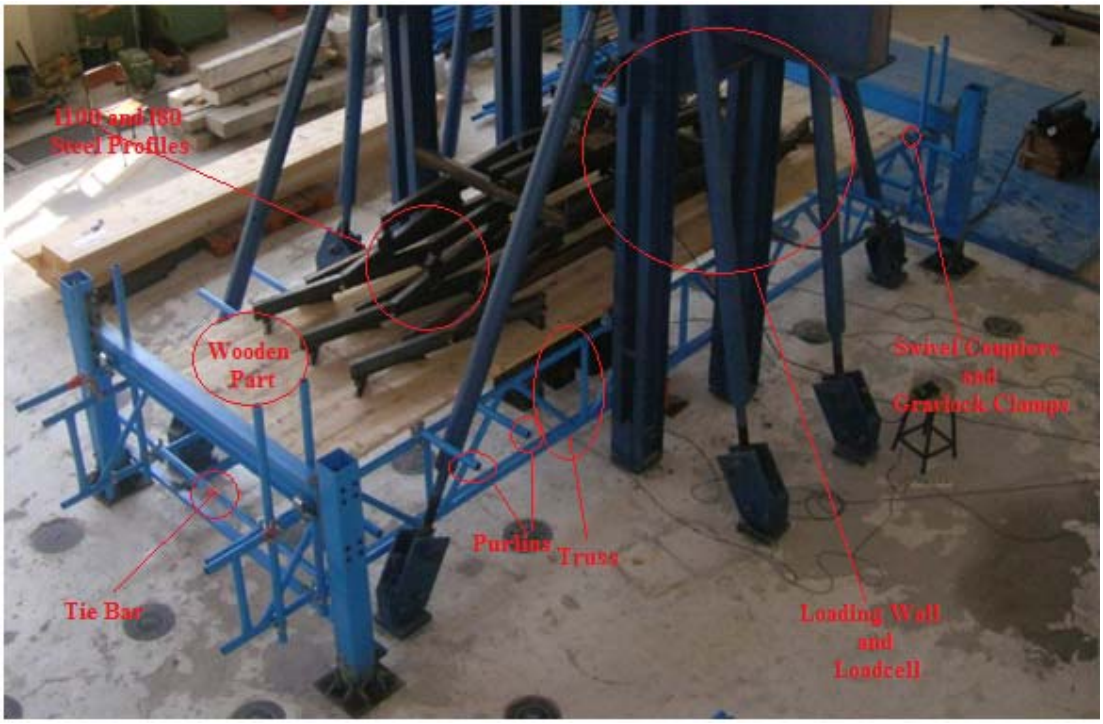

Figure 3. Full-scale 3D Steel Pipe-rack Suspended Scaffolding System

In this study, scaffolds with different system connections were subjected to five loading tests to determine their structural performance. In the tests, a single load from a vertical hydraulic jack with 100 kN capacity was applied to the wooden floor (6 m × 1.6 m) of the scaffolds. A platform was developed to transmit single loads to the specified area. The load transmission platform was constructed with five levels using I100 and I80 steel profiles, which were selected according to the loads to be applied, the transmission distances, and rigidity of the systems. In the tests, the single load via transmission platform is distributed to scaffolding wooden floor, then the loads are carried by purlins and is transmitted to plane trusses, lastly the loads are taken from plane frames (See Figure 4).

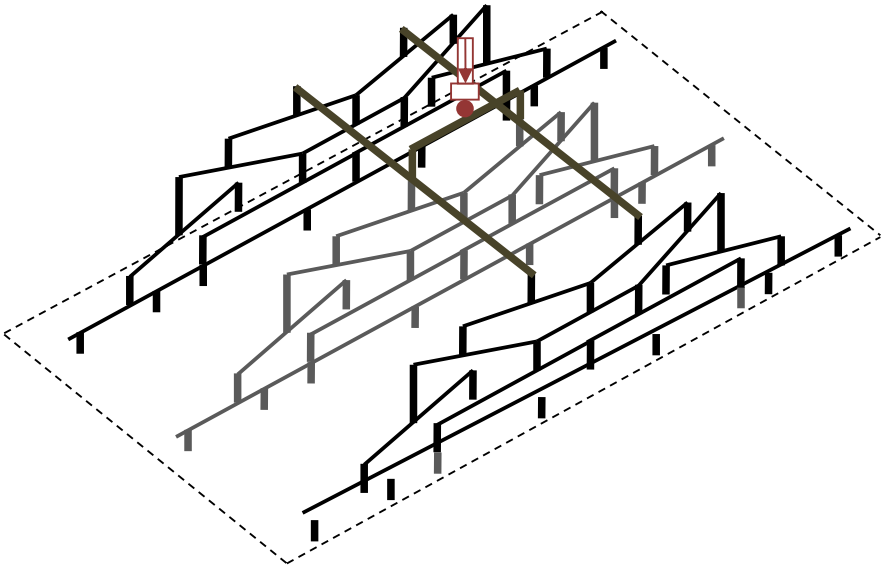

Figure 4. Schematic View of the Developed Load Transmission Platform

3.2 Experimental Tests

The loading tests were performed under five system conditions to evaluate the effects of the number of tie bars on the structural performance of the suspended scaffolds. The means of system conditions is the numbers of the tie bars, which are used to connect the plane trusses at the bottom level (Figure 5). Figure 5 also illustrates the plane trusses and purlins of the scaffolding systems. The systems are prefixed T to reflect the height of the truss, and the system conditions are identified as numbers of tie bars. The names of the scaffolds are provided below:

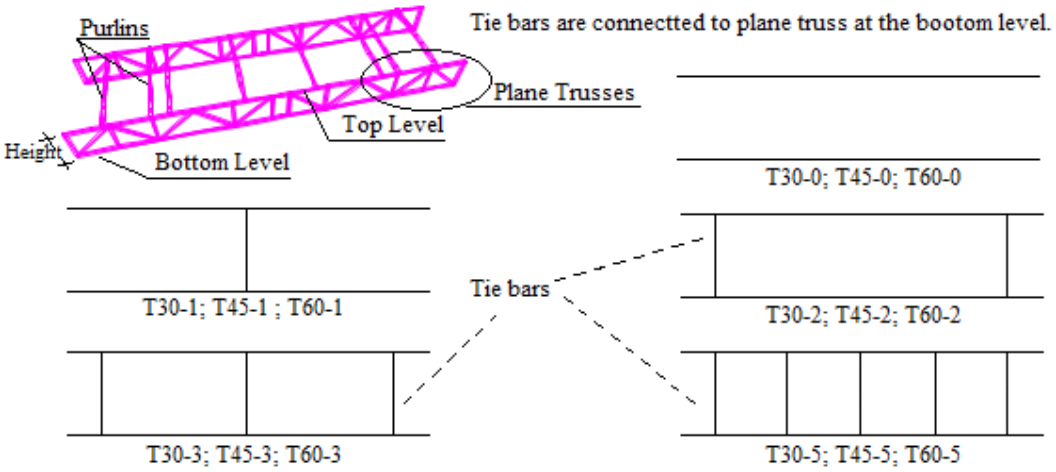

Figure 5. Truss Systems and System Conditions of the Scaffolds Used in the Loading Tests

System names:

- **T30:** The height of the truss is 30 cm
- **T45**: The height of the truss is 45 cm
- **T60:** The height of the truss is 60 cm

System conditions:

- **T30-0:** No tie bar in the system
- **T30-1:** One tie bar at the middle of the plane truss
- **T30-2:** Two tie bars at the beginning and end of the plane truss
- **T30-3:** Three tie bars at the beginning, middle, and end of the plane truss
- **T30-5:** Five tie bars placed at equal distances from the beginning to end of the plane truss
- **T45-0:** No tie bar in the system
- **T45-1:** One tie bar at the middle of the plane truss
- **T45-2:** Two tie bars at the beginning and end of the plane truss
- **T45-3:** Three tie bars at the beginning, middle, and end of the plane truss
- **T45-5:** Five tie bars placed at equal distances from the beginning to end of the plane truss
- **T60-0:** No tie bar in the system
- **T60-1:** One tie bar at the middle of the plane truss
- **T60-2:** Two tie bars at the beginning and end of the plane truss
- **T60-3:** Three tie bars at the beginning, middle, and end of the plane truss
- **T60-5:** Five tie bars placed at equal distances from the beginning to end of the plane truss

A vertical hydraulic jack placed loads at the center of the transmission platform of each system described above. After each test, the system was unloaded, the system was brought into the startup, and the tie bars were reconnected to achieve other system conditions. While excess loads were not applied to the scaffolds, the structures were loaded by as much as their steel profiles and connection rigidities would allow. The load–displacement curves of each test were determined from five critical points of the scaffolding systems using linear variable differential transducers (LVDTs) (Figure 6). The first critical point was the midspan of the scaffold; the LVDT for this point was placed on the wooden floor. The second and third critical points were at the midspans of the purlins, and the fourth and fifth critical points were the midspans of the plane trusses. Photographs taken during the loading tests are shown in Figure 7. While the systems were not loaded until collapse, several scaffolds demonstrated some degree of deformation under certain loads. Figure 8 shows the deformations of T30-0, T45-0, and T60-0.

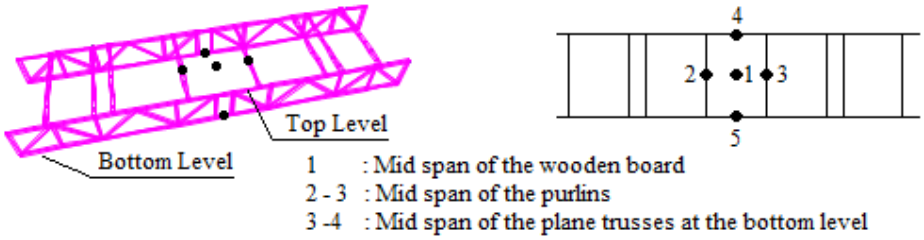

Figure 6. Locations of Linear Variable Differential Transducers on the Scaffolds during the Loading Tests

Figure 7. Photographs of the Loading Tests

Figure 8. Deformation of some scaffolding systems during the loading tests

3.3 Load–Displacement Curves

The load-displacement curves obtained from critical points of systems without tie bars (Point 1, average of displacements on Point 2-3 and average of displacements on Point 4-5, See Figure 6) are illustrated in Figure 9. Under the same load, the T30 systems showed the highest displacements among the systems studied. Displacements showed an increasing trend with increasing load. The displacements of the wooden boards and purlins (Points 1 and 2–3) of the T45 and T60 systems were similar. However, under the same load, the T60 systems showed the minimum truss displacements (Points 4–5) among the systems studied.

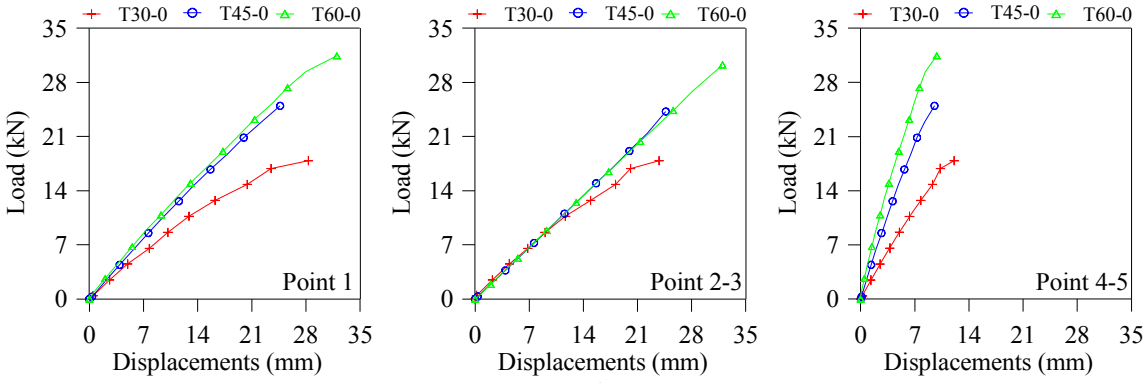

Figure 9. Load–displacement Curves obtained from Critical Points of Scaffolds without Tie Bars: (a) Point 1 (b) Point 2–3 and (c) Points 4–5

The load–displacement curves obtained from critical points of systems with one tie bar are demonstrated in Figure 10. The displacements obtained at critical points of the T30 systems were nearly two times larger than those of the T45 and T60 systems. In addition, the displacement change trends of the wooden boards and purlins of the T45 and T60 systems were similar. However, the displacements of the trusses of the T60 scaffolds were smaller than those of the T30 and T45 scaffolds.

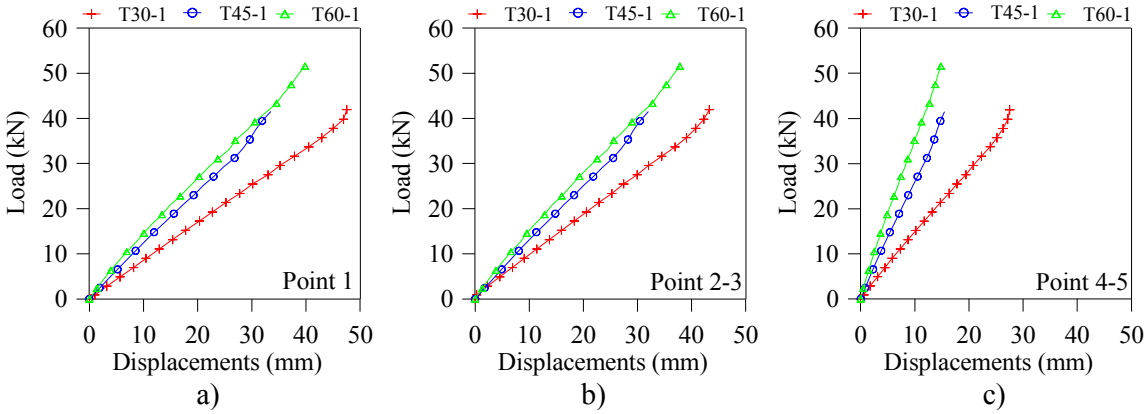

Figure 10. Load-displacement Curves obtained from Critical Points of Scaffolds with One Tie Bar: (a) Point 1 (b) Points 2–3 and (c) Points 4–5

The load–displacement curves obtained from critical points of systems with two, three, and five tie bars are shown in Figures 11, 12, and 13, respectively. The displacement results of these systems are similar to those indicated in Figs. 9 and 10, which means the displacements obtained at critical points of T30 are larger than those obtained at critical points of T45 and T60. Thus, the T45 and T60 systems can be inferred to be more rigid than the T30 systems.

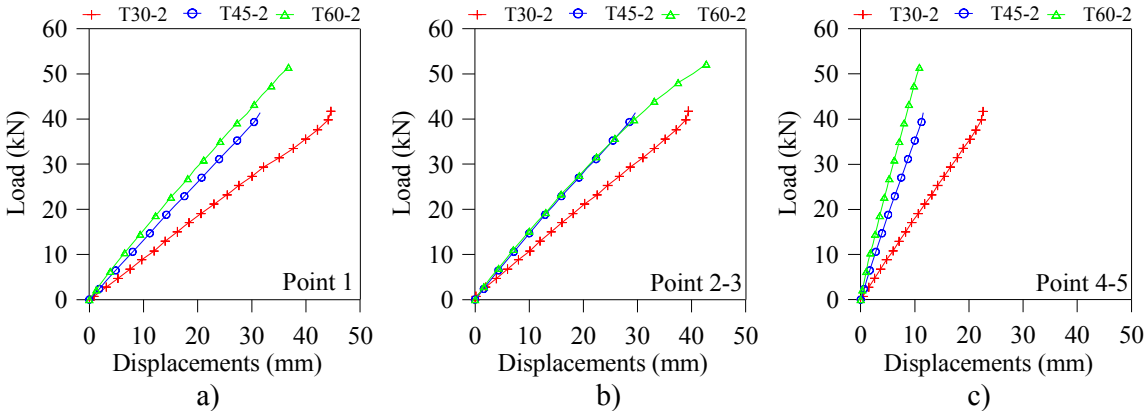

Figure 11. Load–displacement Curves obtained from Critical Points of Scaffolds with Two Tie Bars: (a) Point 1 (b) Points 2–3 and (c) Points 4–5

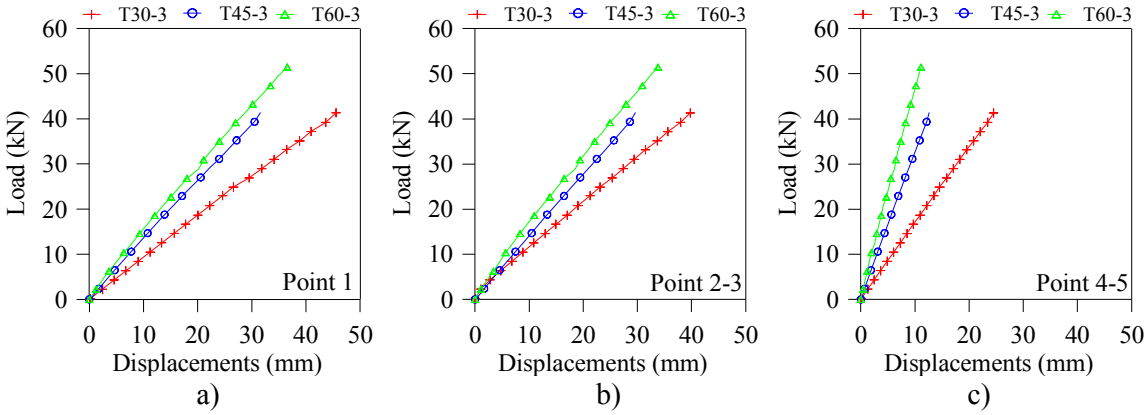

Figure 12. Load–displacement Curves obtained from Critical Points of Scaffolds with Three Tie Bars: (a) Point 1 (b) Points 2–3 and (c) Points 4–5

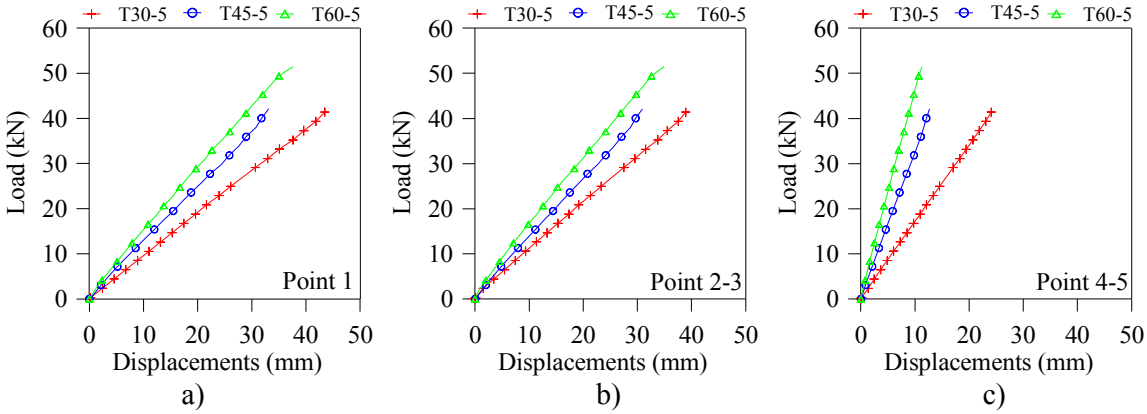

Figure 13. Load–displacement Curves obtained from Critical Points of Scaffolds with One Five Bars: (a) Point 1 (b) Points 2–3 and (c) Points 4–5

Figures 9–13 demonstrate that displacements of the wooden floor were slightly larger than those of the purlins under all system conditions tested. However, the displacements obtained from the trusses under all system conditions studied were only about one-fourth of those observed in wooden floors and purlins. Truss displacements decreased from T30 to T45 and from T45 to T60.

The load–displacement curves obtained from critical points of the T30 systems are illustrated in Figure 14. T30-0 and T30-1, which have no and one tie bar, respectively, showed larger displacements than other systems under the same load conditions. T30-2, T30-3, and T30-5 showed similar load–displacement curves. The displacements of the trusses (Points 4–5) were smaller than those of the purlins (Points 2–3) and wooden boards (Point 1). T30-0 behaved nonlinearly as its load increased. The maximum displacement of T30-1 (47.6 mm) occurred under a load of 41.9 kN at Point 1 (wooden board).

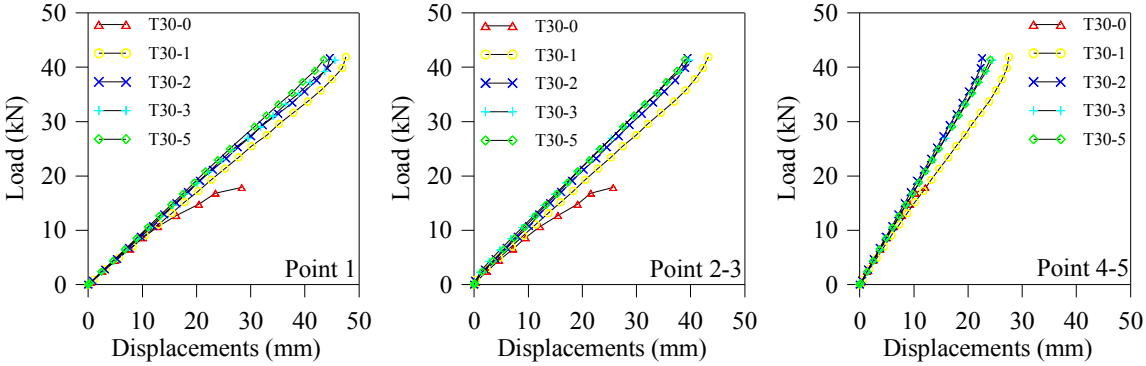

Figure 14. Load-displacement Curves obtained from the Critical Points of T30 Systems: (a) Point 1 (b) Points 2–3 and (c) Points 4–5

The load–displacement curves obtained from critical points of the T45 and T60 systems are illustrated in Figures 15 and 16, respectively. Displacements obtained at critical points of systems with no and only one tie bar are larger than those of other system s. T60-2 showed the lowest displacement among the scaffolds studied.

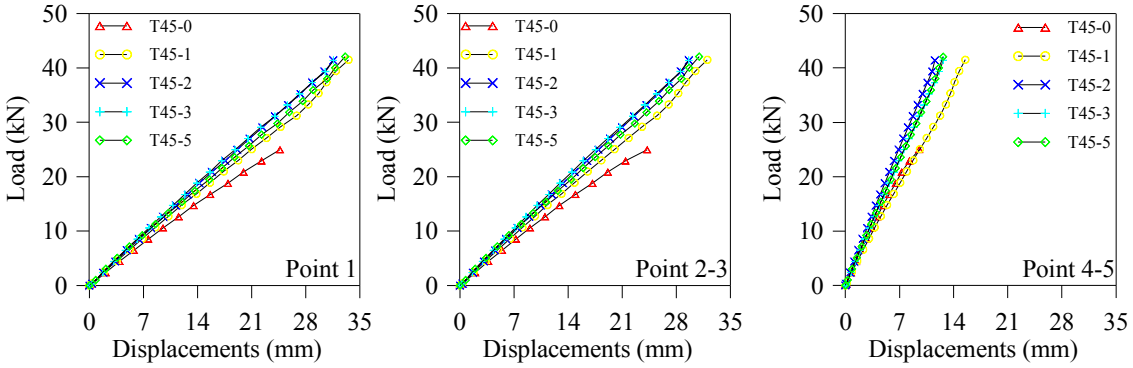

Figure 15. Load-displacement Curves of the T45 Scaffold Measures from Various Critical Points: (a) Point 1 (b) Points 2–3 and (c) Points 4–5

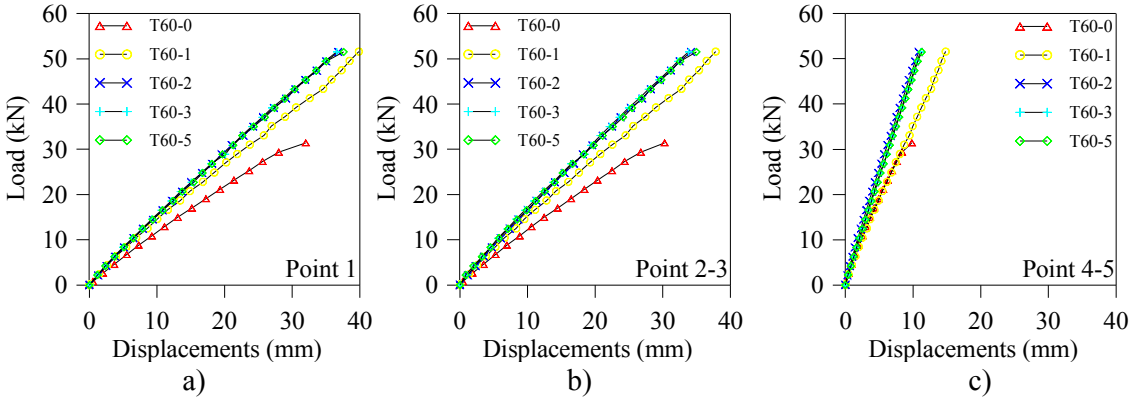

Figure 16. Load-displacement Curves of the T60 Scaffold Measured from Various Critical Points: (a) Point 1 (b) Points 2–3 and (c) Points 4–5

Table 1 shows the maximum displacements of all of the scaffolds under a maximum load. Table 2 is presented to understand the responses of the systems more clearly. In Table 2, displacements obtained from the critical points of all systems, except T30-0, T45-0, and T60-0, were calculated using the linear elasticity approach, under a constant loading 40 kN for all systems T30-0, T45-0, and T60-0, which present no tie bars, were excluded from these calculations because these scaffolds behaved nonlinearly after application of loads of 17, 25, and 30 kN, respectively. Table 2 clearly indicates that scaffolds with two and three tie bars present good behavior, thereby indicating sound structural safety. A bar chart is given in Figure 17 to show the differences of the data listed in Table 2. Figure 17 shows the displacements of all systems under 40 kN load obtained from critical points

Table 1. Displacements of All Systems under a Maximum Load

		L (kN)	D (mm)	L (kN)	D (mm)	L (kN)	D (mm)	L (kN)	D (mm)	L (kN)	D (mm)
		Number of Tie Bars									
		0		1		2		3		5	
T30	Point 1	17.9	28.3	41.9	47.6	41.7	44.6	41.3	45.6	41.4	43.5
	Point 2-3	17.9	23.8	41.9	43.3	41.7	39.4	41.3	39.7	41.4	38.9
	Point 4-5	17.9	12.1	41.9	27.5	41.7	22.6	41.3	24.5	41.4	24.1

T45	Point 1	25.0	24.7	41.5	33.5	41.4	31.6	41.4	31.6	42.1	33.1
	Point 2-3	25.0	24.7	41.5	32.0	41.4	29.6	41.4	29.6	42.1	30.9
	Point 4-5	25.0	9.5	41.5	15.5	41.4	11.6	41.4	12.6	42.1	12.7
T60	Point 1	31.4	32.0	51.6	39.9	51.5	36.8	51.5	36.6	51.5	37.6
	Point 2-3	31.4	32.0	51.6	37.8	51.5	33.5	51.5	33.8	51.5	35.0
	Point 4-5	31.4	9.8	51.6	14.8	51.5	10.8	51.5	11.1	51.5	11.3

Table 2. Displacements of All Systems under 40 kN Load

		L (kN)	D (mm)	L (kN)	D (mm)	L (kN)	D (mm)	L (kN)	D (mm)	L (kN)	D (mm)
		Number of Tie Bars									
		0		1		2		3		5	
T30	Point 1	40.0	-	40.0	45.4	40.0	42.8	40.0	44.2	40.0	42.0
	Point 2-3	40.0	-	40.0	41.3	40.0	37.8	40.0	38.5	40.0	37.6
	Point 4-5	40.0	-	40.0	26.3	40.0	21.7	40.0	23.7	40.0	23.3
T45	Point 1	40.0	-	40.0	32.3	40.0	30.5	40.0	30.5	40.0	31.5
	Point 2-3	40.0	-	40.0	30.8	40.0	28.6	40.0	28.6	40.0	29.4
	Point 4-5	40.0	-	40.0	14.9	40.0	11.2	40.0	12.2	40.0	12.1
T60	Point 1	40.0	-	40.0	30.9	40.0	28.6	40.0	28.4	40.0	29.2
	Point 2-3	40.0	-	40.0	29.3	40.0	26.0	40.0	26.3	40.0	27.2
	Point 4-5	40.0	-	40.0	11.5	40.0	8.4	40.0	8.6	40.0	8.8

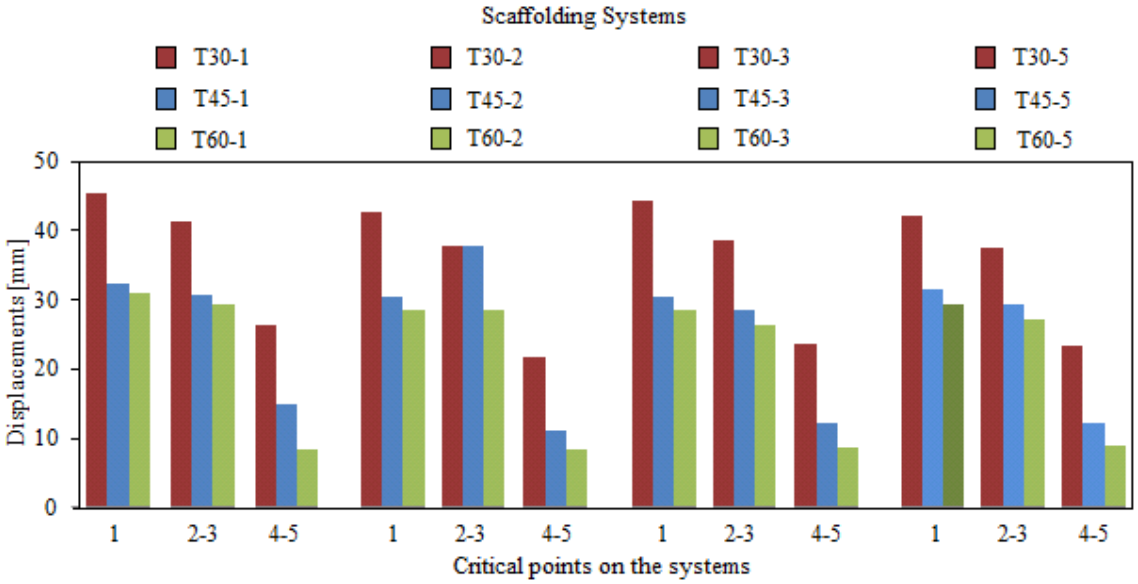

Figure 17. Displacements of All Systems under 40 kN Load obtained from Critical Points

4. CONCLUSIONS

This study experimentally evaluated the effects of number of tie bars on the structural behavior of suspended scaffolding systems. Fifteen suspended scaffolding systems with different truss heights and tie bar connections were constructed and loaded. Load–displacement curves were obtained and compared to determine the optimal suspended scaffolding system from the viewpoint of safety and cost-savings. The following conclusions were obtained:

- Among the systems studied, the T30 scaffolds with no and one tie bar showed the maximum displacements. T30-2, T30-3, and T30-5 showed smaller displacements than did T30-0 and T30-1. T30-0 behaved nonlinearly under a 17 kN load.
- The displacement change trends of the T45 and T60 systems were similar to those of the T30 systems, which means scaffolds with the same truss height show maximum displacements when they include no or only one tie bar. Scaffolds with two, three, and five tie bars showed minimal displacements. Scaffolds with no tie bar (i.e., T45-0 and T60-0) behaved nonlinearly under 25–30 kN loads.
- Displacements of the wooden floor were larger than those of the purlins, which, in turn, were larger than those of the trusses at all system conditions studied. The mechanism of load transfer appears to involve loads moving from the wooden floor to the purlins and then to the trusses, which are the main structural elements of scaffolds. Thus, the displacement results were consistent for all systems studied.
- The displacements of the T30 systems were much larger than those of the T45-and T60 systems. All of these systems, the T60 systems showed the minimum displacements.
- At the same truss height, scaffolds with two tie bars showed smaller displacements than scaffolds with no or only one tie bar. The displacements of these scaffolds were also nearly equal to or smaller than those of scaffolds with three and five tie bars.
- T60-2 showed the lowest displacements among the scaffolds studied under a 40 kN load.
- Considering the displacement responses of all scaffolds studied in this work, T60-2 showed the best rigidity and structural responses. While both T60-3 and T60-5 can satisfy safety requirements, the T60-2 system is recommended when safety and cost-savings are primary considerations.

REFERENCES

[1] Url-1a) http://www.wisegeek.org/what-are-different-types-of-scaffold.htm, 23.02.2016.
Url-1b) http://gzleaderlift.en.alibaba.com/product/518880765-800409624/ Suspended_Scaffolding_System_H_frame_scaffolding.html, 23.02.2016.
Url-1c) http://www.superiorscaffold.com/products/suspended-scaffold/,23.02.2016.
Url-1d) http://www.bigcityaccess.com/products_suspended_platforms.php, 23.02.2016.
Url-1e) https://www.youtube.com/watch?v=imK7i6Vk61g, 23.02.2016.
Url-1f) http://www.scafit.co.nz/suspended-scaffolding, 23.02.2016.
Url-1g) http://www.spiderstaging.com/blog/,23.02.2016.

[2] Url-2. http://www.wisegeek.com/how-should-i-choose-the-best-scaffolding-system.htm. 13.09.2015.

[3] Url-3. http://www.universalscaffold.com/scaffolding/#sthash.BCO28tIs.dpuf. 13.09.2015.

[4] Collins, R., Zhang, S., Kim, K. and Teizer, J., “Integration of Safety Risk Factors in BIM for Scaffolding Construction”, Computing In Civil and Building Engineering 2014, ASCE, doi: 10.1061/9780784413616.039, 2014, pp. 307-314.

[5] Url-4, http://www.chemicalplantsafety.net/construction-safety/scaffold-accident-statistic-the-unspoken-warning/. 13.09.2015.

[6] Peng, J.L., Pan, A.D., Rosowsky, D.V., Chen, W.F., Yen, T. and Chan, S.L., "High Clearance Scaffold Systems during Construction I. Structural Modelling and Modes of Failure", Engineering Structures, 1996, Vol. 18, No. 3, pp. 247-257.

[7] Peng, J.L., Pan, A.D., Rosowsky, D.V., Chen, W.F., Yen, T. and Chan, S.L., "High Clearance Scaffold Systems during Construction II. Structural Analysis and Development of Design Guidelines", Engineering Structures, 1996, Vol. 18, No. 3, pp. 258-267.

[8] Url-5a) http://www.nytimes.com/2014/11/13/nyregion/1-world-trade-center-window-washers.html?_r=0, 23.02.2016.
Url-5b) http://www.thestar.com/news/crime/2012/07/13/scaffold_deaths_construction_company_owner_fined_342500.html, 23.02.2016.
Url-5c) http://www.nytimes.com/2009/08/19/nyregion/19scaffold.html , 23.02.2016.
Url-5d) http://www.greatbasinsafety.com/DDD%20Scaffolding.htm, 23.02.2016.
Url-5e) http://koratfart.com/thailand-news/three-die-in-69th-storey-plunge/, 23.02.2016.
Url-5f) http://www.nydailynews.com/new-york/firefighters-rescue-2-window-washers-fromscaffold-article-1.1112094, 23.02.2016.
Url-5g) https://www.reddit.com/r/OSHA/comments/37twrx/suspended_scaffolding_in_mongolia/, 23.02.2016.

[9] Khudeira, S., "Scaffolding: Safety, Design, and Construction Issues", Practice Periodical on Structural Design and Construction, ASCE, 2008, Vol. 13, pp. 109-110.

[10] Pisheh, Y.P., Shafiei, H.R. and Hatambeigi, M., "A Case Study of Failure due to Inappropriate Usage of Forming Scaffold System", Forensic Engineering 2009: Pathology of the Built Environment, ASCE, doi:http://dx.doi.org/10.1061/41082(362)55), 2009, pp. 536-545.

[11] Hill, H.J., Searer, G.R., Dethlefs, R.A., Lewis, J.E. and Paret, T.F., "Designing Suspended Scaffold Structural Support Elements and Lifeline Anchorages in Conformance with Federal OSHA Requirements", Practice Periodical on Structural Design and Construction, ASCE, 2010, Vol. 15, pp. 186-193.

[12] Lu, C.Y. and Lu, J.L., "Effect of Joint Stiffness on Behavior of Bowl-Scaffold Used in Shanghai-Nanjing High Speed Railway Overpass" ICTE 2011, ASCE, doi:10.1061/41184(419)315, 2011, pp. 1910-1914.

[13] Rubio-Romero J.C., Rubio, M.C. and García-Hernández, C., "Analysis of Construction Equipment Safety in Temporary Work at Height", Journal of Construction Engineering and Management, ASCE, 2013, pp. 139, 9-14.

[14] Beale, R.G., "Scaffold research-A Review", Journal of Constructional Steel Research, 2014, Vol. 98, pp. 188-200.

[15] Kim, K. and Teizer, J., "Automatic Design and Planning of Scaffolding Systems Using Building Information Modeling", Advanced Engineering Informatics, 2014, Vol. 28, pp. 66–80.

[16] Peng, J.L., Yen, T., Kuo, C.C. and Chan, S.L., "Structural Analysis and Modelling of System Scaffolds used in Construction", Proceedings of the Sixth International Conference on Advances in Steel Structures, Hong Kong, 2009, pp. 1099–108.

[17] Prabhakaran, U., "Nonlinear Analysis of Scaffolds with Semirigid Connections", PhD Thesis, UK: Oxford Brookes University, 2009.

[18] Son, K.S. and Park, J.J., "Structural Analysis of Steel Pipe Scaffolding based on the Tightening Strength of Clamps", J. Asian Archit. Build Eng., 2009, Vol. 9, No. 2, pp. 479–85.

[19] Chandrangsu, T., "Advanced Analysis and Probabilistic-based Design of Support Scaffold Systems", PhD Thesis, Australia: Sydney University, 2010.

[20] Chandrangsu, T. and Rasmussen, K.J.R., "Structural Modelling of Support Scaffold Systems", Journal of Constructional Steel Research, 2011, Vol. 67, No. 5, pp. 866–875.

[21] Prabhakaran, U., Beale, R.G. and Godley, M.H.R., "Analysis of Scaffolds with Connections Containing Looseness", Computer and Structures, 2011. Vol. 89, No. 21–22, pp. 1944–55.

[22] Yue, F. and Yuan, Y., "Design Methods of Integral-lift Tubular Steel Scaffolds for High-rise Building Construction", Struct. Des. Tall Spec. Build, 2012, Vol. 21, No. 1, pp. 46–56.

[23] Zhang, H. and Rasmussen, K.J.R., "System-based Design for Steel Scaffold Structures using Advanced Analysis", J. Constr. Steel Res. 2013, Vol. 89, pp. 1–8.

[24] Chandrangsu, T. and Rasmussen, K.J.R., "Full-scale Tests and Advanced Structural Analysis of Formwork Assemblies", Proceedings of the Sixth International Conference on Advances in Steel Structures, Hong Kong, 2009, pp. 1083–90.

[25] Liu, H., Zhao, Q., Wang, X., Zhou, T., Wang, D., Liu, J. and Chen, Z., "Experimental and Analytical Studies on the Stability of Structural Steel Tube and Coupler Scaffolds without X-bracing", Eng. Struct., 2010, Vol. 32, pp. 1003–15.

[26] Peng, J.L,, Wang, P.L., Huang, Y.H. and Tsai, T.C., "Experimental Studies of Load Capacities of Double-layer Shoring Systems", Adv. Steel Constr. 2010, Vol. 6, No. 2, pp. 698–721.

[27] André, J., Beale, R.G. and Baptista, A.M., "Experimental Investigation of Bridge Falsework Cuplok Joints", VIII Congresso de Construção Metálica e Mista, Guimaráes, Portugal, 2011, pp. II795–804.

[28] Peng, J.L., Wang, P.L., Chan, S.L. and Huang, C.H., "Load Capacities of Single-layer Shoring Systems — An Experimental Study", Adv. Struct. Eng., 2012, Vol. 15 No. 8, pp. 1389–410.

[29] OSHA3150, "A Guide to Scaffold Use in the Construction Industry", Small Business Safety Management Series, U.S. Department of Labor, 2002.

RESIDUAL STRESS MEASUREMENT ON WELDED Q345GJ STEEL H-SECTIONS BY SECTIONING METHOD AND METHOD IMPROVEMENT

Bo Yang[1, 2], Shidong Nie[1, 2], Shao-Bo Kang[1, 2], Gang Xiong[1, 2, *], Ying Hu[1, 2], Jubo Bai[1, 2], Weifu Zhang[1, 2] and Guoxin Dai[1, 2]

[1] *Key Laboratory of New Technology for Construction of Cities in Mountain Area (Chongqing University), Ministry of Education, Chongqing 400045, China*
[2] *School of Civil Engineering, Chongqing University, Chongqing 400045, China*
**(Corresponding author: E-mail:* 195704148@qq.com*)*

Received: 7 December2015; Revised: 13 April 2016; Accepted: 1 May 2016

ABSTRACT: High-performance structural steel has attracted a lot of attention in the past decade and been widely used in many landmark building structures, such as the National Olympic Stadium, the new CCTV Headquarters, and the Canton Tower in China. However, their structural performance has not been fully studied yet. Among all parameters, residual stress is one of the most important mechanical imperfections, which can reduce the stability resistance of steel structures. This paper presents an experimental investigation on the residual stress in welded H-sections made of high-performance steel Q345GJ by using sectioning method. Besides, a simple yet accurate method was proposed for determining the residual stress of curved strips. Comparisons between residual stress profiles obtained by different methods suggested that the proposed method was in good agreement with other ones. Test results showed that the magnitudes of residual stress in welded Q345GJ H-sections was significantly different from that predicted by existing models. Finally, suggestions were made for welded Q345GJ steel H-sections in accordance with experimental results.

Keywords: Q345GJ steel, Welded H-sections, Residual stress, Sectioning method, Curve correction, Straightening method

DOI: 10.18057/IJASC.2017.13.1.5

1. INTRODUCTION

Since this century, the number of large-span and high-rise buildings is increasing rapidly worldwide. In these types of structures, high performance structural steel has been extensively used due to high levels of vertical and horizontal loads. As a typical high-performance steel, high-strength steel with tensile strength of 460 MPa to 1000 MPa has been employed in construction practices in Japan [1], Europe [2], the USA [3] and Australia [4]. However, with increasing steel strength, material properties such as the reduction of plastic deformation capacity, poor weldability and low impact toughness become more critical which may lead to brittle failure [5]. Therefore, merely increasing tensile strength of steel may not meet the requirements for the design of steel structures, in particular for large-span or super high-rise buildings.

To overcome the main weaknesses of high-strength steel, high-performance SN structural steel has been developed and incorporated in Japanese standard since 1994 [6]. More stringent requirements are specified for SN steel than normal one to ensure full plastic deformation of steel structures under strong earthquakes. In addition, lower carbon equivalent ($\leq$0.46) in SN steel enables it to achieve better weldability. In the USA, American structural steel A992 [7] shows similar performance to SN steel and it has been widely used in building structures, especially in the areas with high seismic intensity [8, 9]. In China, another type of high-performance structural steel, designated as GJ, has been included in the national standard of "Steel plates for building structure"

(GB/T19879-2005) [10]. Compared with conventional steel in the standards of "Carbon structural steels" [11] and "High-strength low-alloy structural steels" [12], this type of structural steel is more appropriate for use in large-span or high-rise structures due to its lower content of harmful non-metallic elements like sulphur and phosphorus, smaller yield-to-tensile strength ratio, less scatter of yield strength, lower thickness effect on yield strength and better weldability [13]. High-performance GJ steel, mainly Q345GJ, has been utilised in many landmark projects, such as the National Olympic Stadium (the Bird Nest Stadium) [14], the CCTV Headquarters in Beijing [15], and the Canton Tower [16]. However, the same design methods and design values as that for conventional steel are recommended for GJ steel [17]. Indeed, there can be significant differences between GJ and conventional steels in terms of the stability resistance, and thus, the advantages of GJ steel over conventional steel have not been fully taken in current design due to the lack of test data.

Among all parameters, residual stress is one of the most important mechanical imperfections, which can reduce the stability resistance of steel structures. Besides, it can also affect the machining accuracy of weldment and result in stress corrosion cracking [18]. In order to provide fundamental experimental data for further study on the stability resistance of welded GJ steel H-beams under vertical load, it is necessary to quantify the residual stress distribution in the sections through experimental tests.

This paper presents an experimental study on the residual stress in welded Q345GJ steel H-sections. In the experimental programme, sectioning method was used to quantify the residual stress distribution in four welded Q345GJ H-sections. Comparisons were made among different methods for curve corrections. Besides, a new method was proposed for curved strips whereby correction process can be greatly simplified. Experimental results suggested that the residual stress distribution model in welded Q345GJ H-sections was different from that in conventional steel sections. This study serves as the basis of further experimental and numerical investigations on the stability resistance of Q345GJ steel beams subject to vertical loads.

2. SECTIONING METHOD FOR RESIDUAL STRESS MEASUREMENT

Several methods can be used to determine the residual stress in steel sections, namely, sectioning method, hole-drilling method, X-ray method and ultrasonic method [19].Among all the methods, the sectioning method is easy and simple for use due to its good operability and high accuracy. It can also be used to verify the accuracy of other measuring methods [20, 21].

In the sectioning method, internal residual stresses on a section are released by cutting the section into a number of small strips. By measuring the change in the strip length before and after cutting, the average residual stress along a specific length of the section can be quantified in accordance with Hook's Law. Accordingly, the residual strain can be calculated from the following equation.

$$\varepsilon_r = \varepsilon_1 - \varepsilon_{T1} = \frac{L_f - L_i}{L_i} - \frac{L_{Tf} - L_{Ti}}{L_{Ti}} \quad (1)$$

where ε_r is the average residual strain over a specific length; ε_1 is the total strain due to relaxation and temperature change; ε_{T1} is the strain induced by temperature change; L_i is the initial gauge length before cutting; L_f is the final gauge length after cutting; L_{Ti} is the initial gauge length of reference strip; and L_{Tf} is the final gauge length of reference strip.

Thus, the residual stress can be quantified from Eq. 2.

$$\sigma_r = -E\varepsilon_r \quad (2)$$

where σ_r is the average residual stress and E is the elastic modulus.

By means of the sectioning method, a large number of experimental studies have been conducted on the residual stresses in different types of steel. As for conventional steel, Alpsten and Tall [22] experimentally investigated the residual stress in welded sections of different dimensions and welding processes and analysed the effects of various parameters on the residual stress. Similar tests were also conducted by Tebedge et al. [20]. Besides, Wang et al. [21] proposed a simplified residual stress distribution model based on test results For high-strength steel, Rasmussen and Hancock [23, 24] quantified the residual stress of welded H and cruciform sections of 690 MPa steel by using the sectioning method. Wang et al. [25, 26] and Ban et al. [27-29] determined the residual stress distributions in various type of welded sections made of high-strength steel, such as H and box sections. In accordance with the experimental results, a new set of residual stress distribution models was proposed for steel sections with different dimensions. For high-performance structural steel, experimental investigations were conducted by Spoorenberg et al. [30] on the residual stress in wide flange quenching and self-tempering 460 MPa steel sections. However, limited test data are available for welded GJ steel sections to date. Therefore, experimental tests are needed to determine the residual stress distribution model in welded GJ steel sections.

3. EXPERIMENTAL PROGRAMME

3.1 Specimen Design and Manufacture

In the experimental programme, four welded Q345GJ steel H-sections with different dimensions were tested by using the sectioning method, as shown in Figure 1. Table 1 summarises the details of specimens. Specimens with fillet welds between steel plates were fabricated by flame-cut plates and submerged arc welding. The four specimens were classified into two categories. One category contained two doubly-symmetric sections with blind holes drilled on the outer surface only, whereas the other included one doubly-symmetric section and one singly-symmetric section with through holes on both outer and inner surfaces.

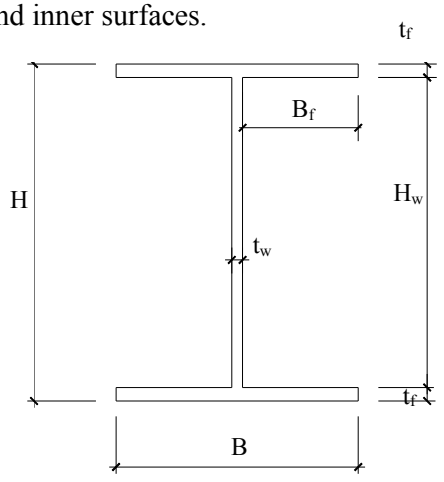

Figure 1. Schematic of sectional dimensions

Table 1. Welded H-sections of Q345GJ steel

Hole type	Specimen	Sectional dimension	H (mm)	B (mm)	t_w (mm)	t_f (mm)	H/B	B_f/t_f	H_w/t_w
Blind hole	H1	300*200*8*10	300	200	8	10	1.5	9.6	35
	H2	400*200*8*10	400	200	8	10	2.0	9.6	47.5
Through hole	H3	400*200*8*10	400	200	8	10	2.0	9.6	47.5
	H4	350*220(180)*8*10(8)	350	220/180	8	10/8	1.59/1.94	13.25/10.75	41.5

3.2 Material Properties

Prior to testing, tensile coupons were cut per Chinese standard GB/T GB2975-1998 [31] and tested in accordance with GB/T 228.1-2010 [32]. Figure 2 shows the dimensions of the coupons. Table 2 includes the material properties of steel, including Young's modulus E, yield strength R_{eH} and ultimate tensile strength R_m.

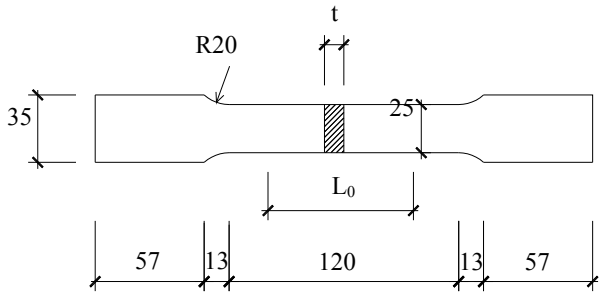

Figure 2. Geometry of tensile coupons

Table 2. Material properties of Q345GJ

Thickness of plates t (mm)	R_{eH} (MPa)	R_m (MPa)	E (GPa)
10	397.6	539.9	209.2
8	457.8	600.8	204.8

3.3 Sectioning Process

Sectioning of welded Q345GJ H-sections was conducted following the procedure recommended by Ziemian [19] and Alpsten and Tall [22]. The selected section for residual stress measurement was at least 1.5 times the section depth away from both ends in order to eliminate the end effect. Considering both accuracy and efficiency, the width of strips in the flanges and at the edges of the web was about 10 mm, while the width was adjusted to 15 mm in the middle of the web. Two gauge holes with a distance of 250 mm (Whitttemore strain gauge length) were drilled along the centre line of each strip. Figure 3 shows the details of blind and through holes. The specimens were

sectioned into small strips with specific length and widths by using wire electrical discharge machining, as shown in Figure 4, which released little heat during sectioning. The distance between the two holes on each strip was measured by using Whitttemore strain gauge with an accuracy of 0.001 mm before and after sectioning. Meanwhile, a reference strip with the same material and dimensions was measured to eliminate the temperature effect. To minimise the errors, each strip was measured for three times. For curved strips, the offset of steel strips from the original axis was measured for curve corrections on a high-precision measuring table.

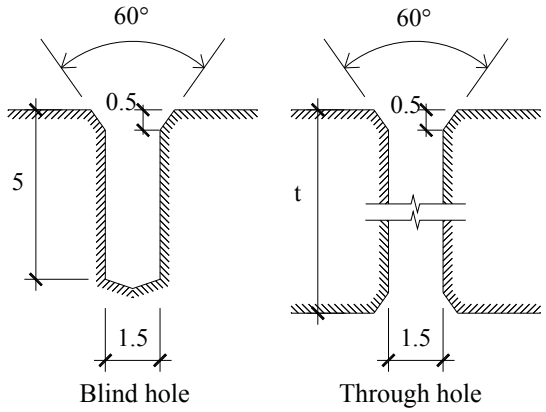

Figure 3. Dimension of gauge holes

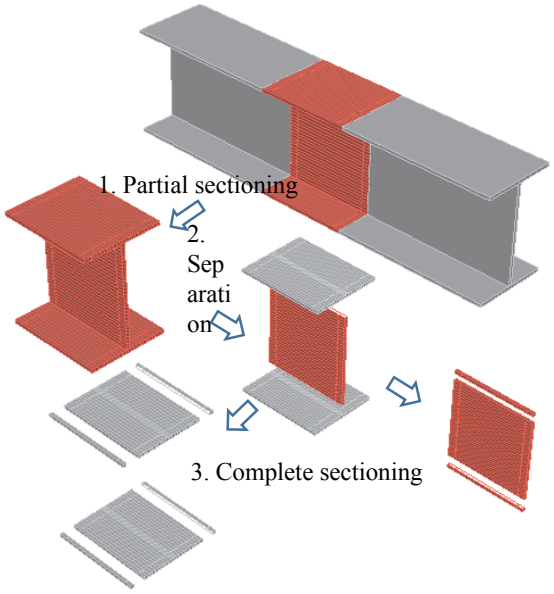

Figure 4. Procedure for sectioning

4. CORRECTION OF RESIDUAL STRESS

After sectioning, steel strips near the flame-cut edges and welds showed significant out-of-plane curvature. On this condition, the measured strip length was only the chord length rather than arc length, as shown in Figure 5. Thus, corrections had to be made in calculating the strain. Several correction methods have been proposed to take account of the curvature.

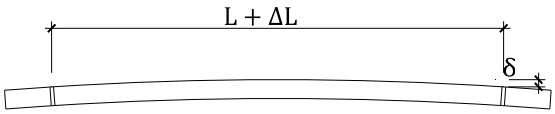

Figure 5. Geometry of curved strips

4.1 Curve correction Method

In accordance with test results, Tebedge and Tall [22] suggested a correction equation, as expressed in Eq. 3, and pointed out that the axial stress was the average value of top and bottom stresses.

$$\Delta\varepsilon = \frac{(\delta/L)^2}{6(\delta/L)^4 + 1} \tag{3}$$

where L is the gauge length of steel strips and δ is the offset to gauge length (see Figure 5). The equation has been widely used for calculating residual stresses in steel sections [33, 34].

Besides, Cui [35] assumed a parabolic curve and derived a correction equation, as expressed in Eq. 4.

$$\Delta\varepsilon = \left[40\left(\frac{\delta}{L}\right)^2 - 96\left(\frac{\delta}{L}\right)^4\right]/15 \tag{4}$$

However, Sherman [36] suggested that, for a long prismatic member, the residual stress did not vary along its length and the curve was a portion of a circular curve in the residual stress measurement in tubular members. In order to obtain the strain relaxation at the middle-thickness layer of a strip, three corrections were required, including the final measurement along the chord instead of the arc ε_s, the misalignment of the conical extensometer point and gauge hole axis ε_h, and the difference between the outer surface and middle-thickness layer ε_t. Moreover, another correction ε_n due to lateral bending was introduced by the Structure Stability Research Council [37]. Therefore, four corrections had to be considered in residual stress calculations as follows.

$$\varepsilon_s = \frac{8}{3}\left(\frac{\delta}{L}\right)^2 \tag{5}$$

$$\varepsilon_h = \frac{4d\delta}{L^2}\tan\frac{\alpha}{2} \tag{6}$$

$$\varepsilon_t = \frac{4t\delta}{L^2} \tag{7}$$

$$\varepsilon_n = \frac{8}{3}\left(\frac{\delta_1}{L}\right)^2 \tag{8}$$

where δ_1 is the tortuosity sagittal height of lateral bending, d is the diameter of the contact edge hole, α is the internal angle of the extensometer gauge point, and t is the strip thickness.

The first two correction methods only consider the difference between chord and arc. Comparatively, more influential parameters are taken into account in the circular correction method proposed by Sherman [36]. If only the difference between chord and arc is taken into account, Eqs. 3, 4 and 5 provide substantially different results. Figure 6 shows the comparison of calculated

values from the equations. Among the three equations, Eq. 3 gives the smallest values, as shown in Figure 6, whereas the values obtained from Eqs. 4 and 5 are nearly identical. Furthermore, the discrepancy between Eqs. 3 and 4 or 5 increases with increasing δ/L. For instance, the difference is less than 5 MPa when δ/L is 1/250. However, the value reaches up to 90 MPa, if δ/L is equal to 4/250.

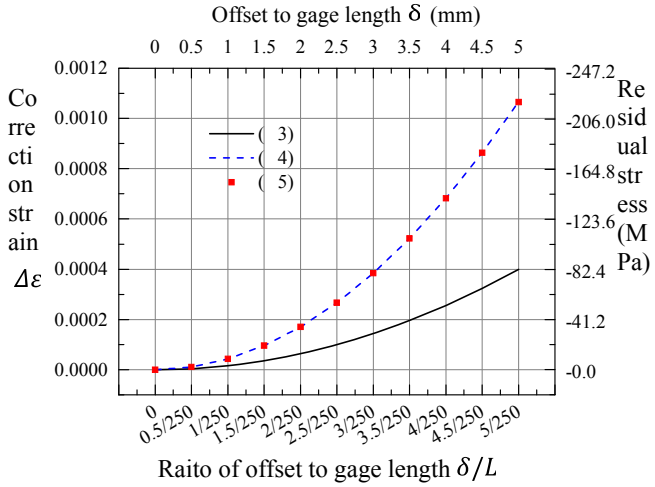

Figure 6. Comparison between different correction methods

Besides, in Sherman's circular curve correction method, the residual stress at the middle-thickness layer can be calculated from the measurement on one surface. Thus, this correction method is particular useful for closed sections like box and circular sections, as measurements on the inner surface cannot be easily made. Total circular curve correction is the combination of Eqs. 5, 6, 7 and 8. When a convex surface is measured, the total correction can be determined from Eq. 9.

$$\Delta\varepsilon = \varepsilon_s + \varepsilon_n - \varepsilon_h - \varepsilon_t \quad (6)$$

However, for a concave surface, the total circular curve correction becomes

$$\Delta\varepsilon = \varepsilon_s + \varepsilon_n + \varepsilon_h + \varepsilon_t \quad (7)$$

Calculations suggest that ε_t is the most critical parameter in determining $\Delta\varepsilon$. Besides, the calculated ε_t from Eq. 6 is largely dependent on the measurements of strip thickness t and arc offset δ. However, the offset cannot be easily measured in experimental tests. Therefore, it is preferred to measure on both surfaces of strips and calculate the average stress if possible.

4.2 Residual Stress Results

Figure 7 shows the calculated residual stressed. For specimens H1 and H2, measurements were only made on the out surface through blind holes and corresponding residual stress at the middle-thickness layer was calculated by using the circular curve correction method, as shown in Figures 7(a) and (b). However, through holes were prepared for specimens H3 and H4 and the circular curve correction method was used for both surfaces. The residual stress at the middle-thickness layer could be approximated by the average value of stresses on the outer and inner surfaces, as shown in Figures 7(c) and (d). It is noteworthy that the residual stresses on the outer and inner surfaces of flanges were quite different from each other. High compressive stresses

were obtained on the outer surface near the flange tip, whereas tensile stresses were on the inner surface. This was mainly attributed to the bending of these strips after sectioning. However, the residual stresses at the middle-thickness layer, obtained from the outer surface, inner surface and their average values, were close to one another. It indicates that results of specimens H1 and H2 could still be reliable, even though they were only calculated from the measurements on the outer surface.

5. STRAIGHTENING METHOD

When subject to pure bending, fibres of a slender beam are shortened on one surface and elongated on the other. At the neutral layer, the fibre length remains unchanged. As a result, the final length of a curved strip can be determined by straightening and the residual stress at the middle-thickness layer can be directly measured without any curve corrections.

Figure 8 shows the apparatus for straightening curved strips. By using a customised L-shaped marble table board with a flatness of 0.01 mm, the curve strip was placed at the re-entrant corner of the board, and then was straightened when two orthogonal surfaces of the strip clung tightly to the standard planes by using several G-clamps. Finally, the total length of the middle-thickness layer could be measured. Figure 9 shows the comparisons between residual stresses by straightening and the circular curve correction. Reasonably good agreement is obtained in terms of the residual stress distribution and magnitudes.

Residual stresses on each section should be self-equilibrated and the closing error of the stresses should be zero. Therefore, to evaluate the accuracy of the measured residual stresses, a closing error index σ_{err} is defined as follows.

$$\sigma_{err} = \left[\sum_{i=1}^{n} A_i \cdot \sigma_{ri}\right] / \sum_{i=1}^{n} A_i \tag{8}$$

where A_i is the cross-sectional area of a strip, σ_{ri} is the value of residual stress along the strip, and n reprents the number of strips.

Figure 10 shows the closing error indexes of residual stresses obtained from the two methods including the circular curve correction and straightening methods. The stress error indexes of the four sections were around zero and the maximum value was only 12.5 MPa, about 3.6% of the nominal yield strength. It indicates that both the circular curve correction and straightening methods yield good accuracy on residual stresses. Hence, in the following section, the mean value of residual stresses obtained from these two methods are used for determining the residual stress profile.

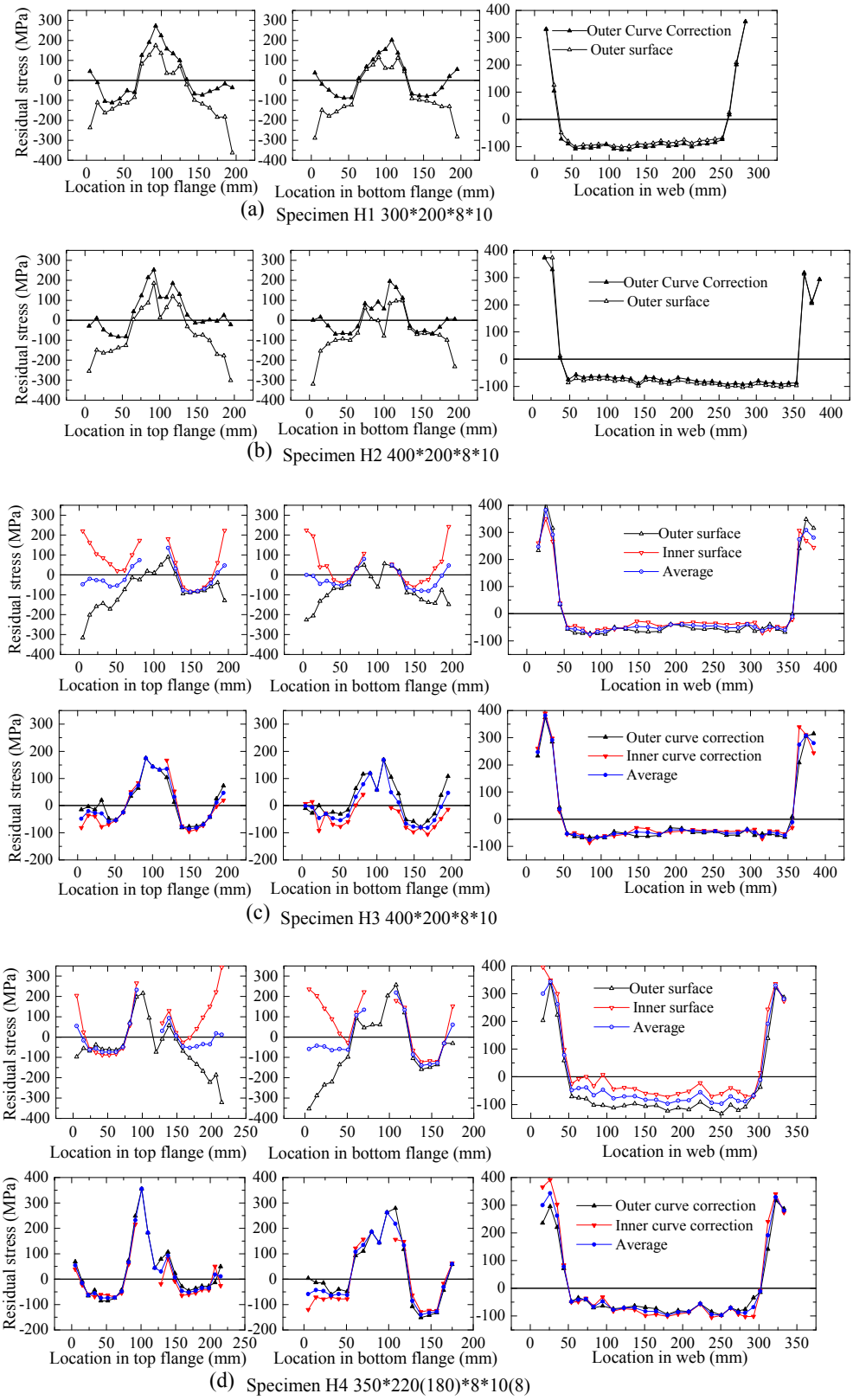

Figure 7. Residual stress distributions

Figure 8. Setup for straightening curved strips

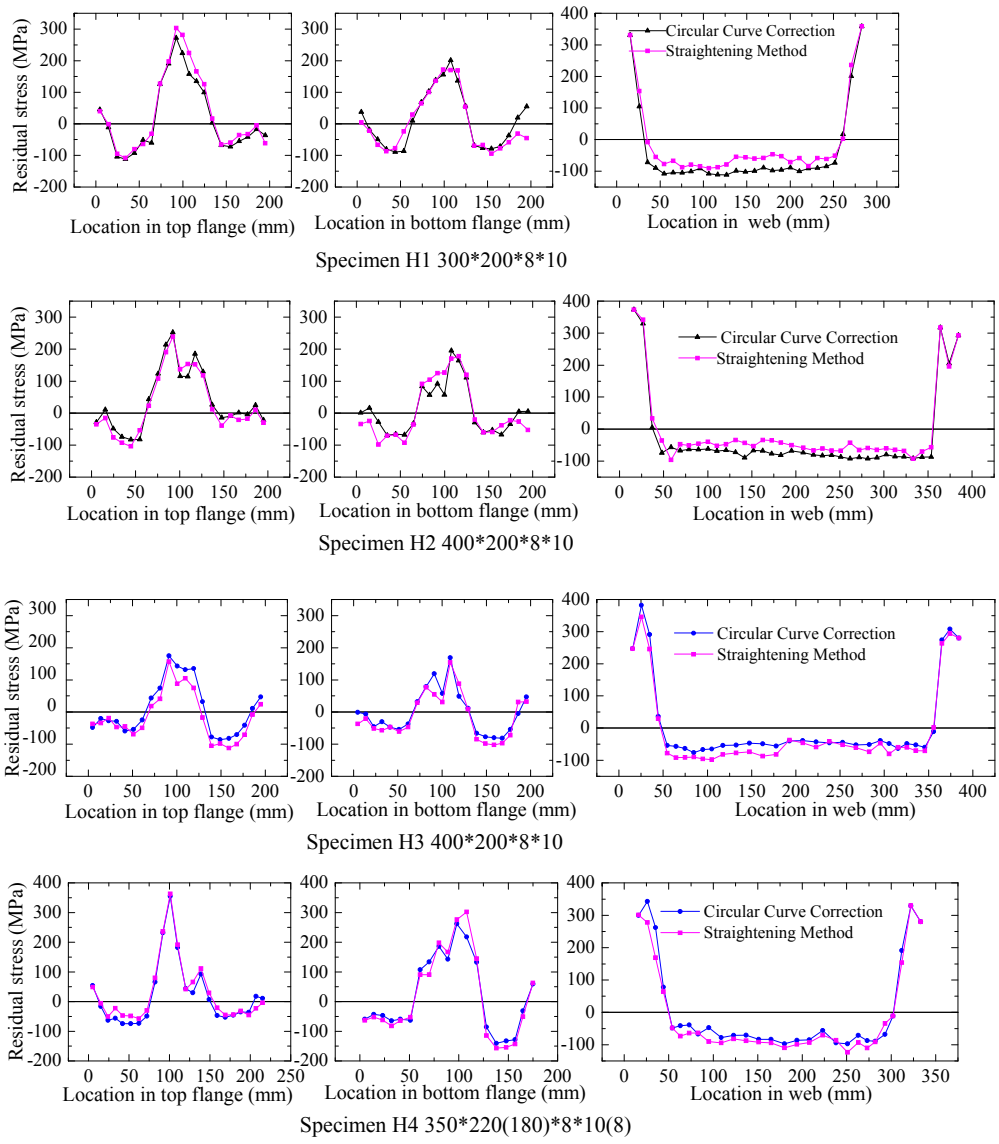

Figure 9. Comparison between residual stresses by correction

6. RESIDUAL STRESS PROFILE

The residual stress profile of welded Q345GJ steel sections is similar to that of conventional steel sections, as shown in Figure 9. The main characteristics of residual stresses are discussed as follows.

(1) A W-shaped bond stress profile was observed in the flange. In most cases, the flange tip was under tension with limited tensile stresses. In the middle of the flange were high tensile residual stresses, with the maximum value less than the nominal yield strength, except for the top flange of specimen H4. Compressive residual stresses were distributed at other regions of the flange, with the maximum value of about 100 MPa. Due to considerable bending of strips near the flange tip, residual stresses on the outer and inner surfaces were significantly different from each other.

(2) Tensile residual stresses with large gradient were measured near both ends of the web, but the maximum value was still less than the nominal yield strength. Compressive residual stresses with a peak value of 80 MPa were stable in the middle portion of the web.

Table 3 summarises the residual stresses at specific locations of welded H-sections. In the table, σ_{ft1}, σ_{ft2}, σ_{ft3} and σ_{ft4} denote the tensile residual stresses at the flange tips; σ_{fc1}, σ_{fc2}, σ_{fc3} and σ_{fc4} signify the maximum compressive values in the flanges; σ_{fwt1} and σ_{fwt2} represent the maximum tensile residual stresses in the flanges near the welds; σ_{wt1} and σ_{wt2} denote the maximum tensile stresses at the edges of the web; and σ_{wc} represents the average compressive stress in the middle of the web.

Table 4 lists the characteristic values of residual stresses in welded H-sections, which represent the average values of peak residual stresses. For example, σ_{ft} denotes the average value of four peak residual stresses at the four flange tips of H-sections. With these values, the effect of cross section on the residual stresses in the web and flanges can be studied. Specimens H1 and H2 had the same dimensions except for the web height, 280 mm and 380 mm, respectively. Almost the same characteristic tensile residual stresses were obtained in the web and flanges near the welds. However, the characteristic compressive stress (82.6 MPa) in the web of H1 was 23.5% greater than that (66.9 MPa) of H2. Besides, the characteristic compressive stress (86.7 MPa) at the flanges of H1 was 41.4% greater than that (61.3 MPa) of H2. The results indicate that during the cooling stage after welding, the section with higher web had a larger area to equilibrate shrinking stresses, which resulted in smaller compressive residual stresses. Therefore, the web and flanges were affected by each other, which is different from the assumption in many existing residual stress distribution models.

As a singly-symmetric section, H4 showed obvious asymmetry of residual stresses in the flanges, as included in Table 3. The maximum tensile residual stress in the top flange was 359.0 MPa, around 33.6% larger than that (268.8 MPa) in the bottom flange. Besides, the average peak compressive residual stress in the bottom flange was around 2 times the value in the top flange.

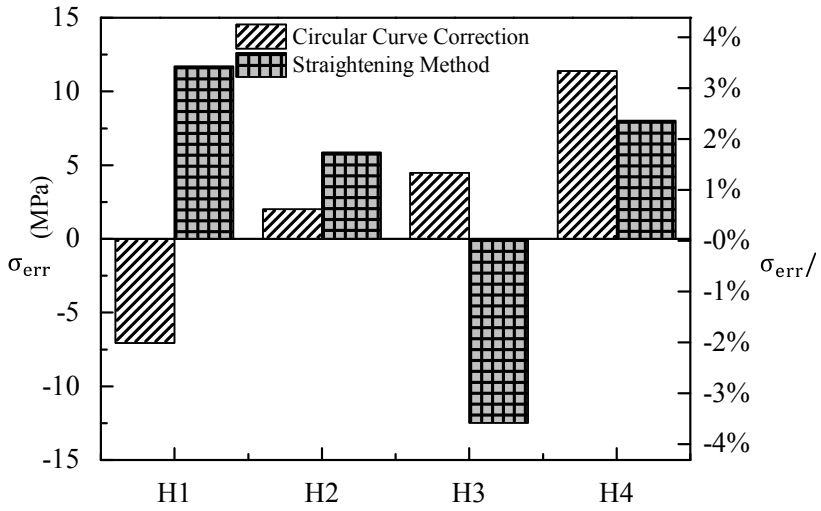

Figure 10. Residual stress closing error indexes of different methods

Table 3. Residual stresses at specific locations of welded H-sections

Specimen	In the flange (MPa)										In the web (MPa)		
	σ_{ft1}	σ_{ft2}	σ_{ft3}	σ_{ft4}	σ_{fwt1}	σ_{fwt2}	σ_{fc1}	σ_{fc2}	σ_{fc3}	σ_{fc4}	σ_{wt1}	σ_{wt2}	σ_{wc}
H1	42.3	-48.8	20.6	4.8	287.6	185.6	-109.9	-66.7	-83.5	-86.8	330.9	358.4	-82.6
H2	-32.0	-26.1	-16.7	-23.8	245.6	182.8	-93.5	-11.2	-80.3	-60.3	373.4	292.6	-66.9
H3	-42.3	35.4	-18.8	39.4	166.3	161.3	-61.1	-97.0	-57.4	-90.9	364.0	301.3	-61.8
H4	51.5	3.7	-60.8	61.7	359.0	268.8	-65.0	-48.9	-73.7	-148.8	310.5	329.5	-85.7

Table 4. Characteristic residual stresses at specific locations of welded H-sections

Specimen	In the flange (MPa)			In the web (MPa)	
	σ_{ft}	σ_{fwt}	σ_{fc}	σ_{wt}	σ_{wc}
H1	4.7	236.6	-86.7	344.6	-82.6
H2	-24.6	214.2	-61.3	333.0	-66.9
H3	3.4	163.8	-76.6	332.6	-61.8
H4	14.0	313.9	-84.1	320.0	-85.7

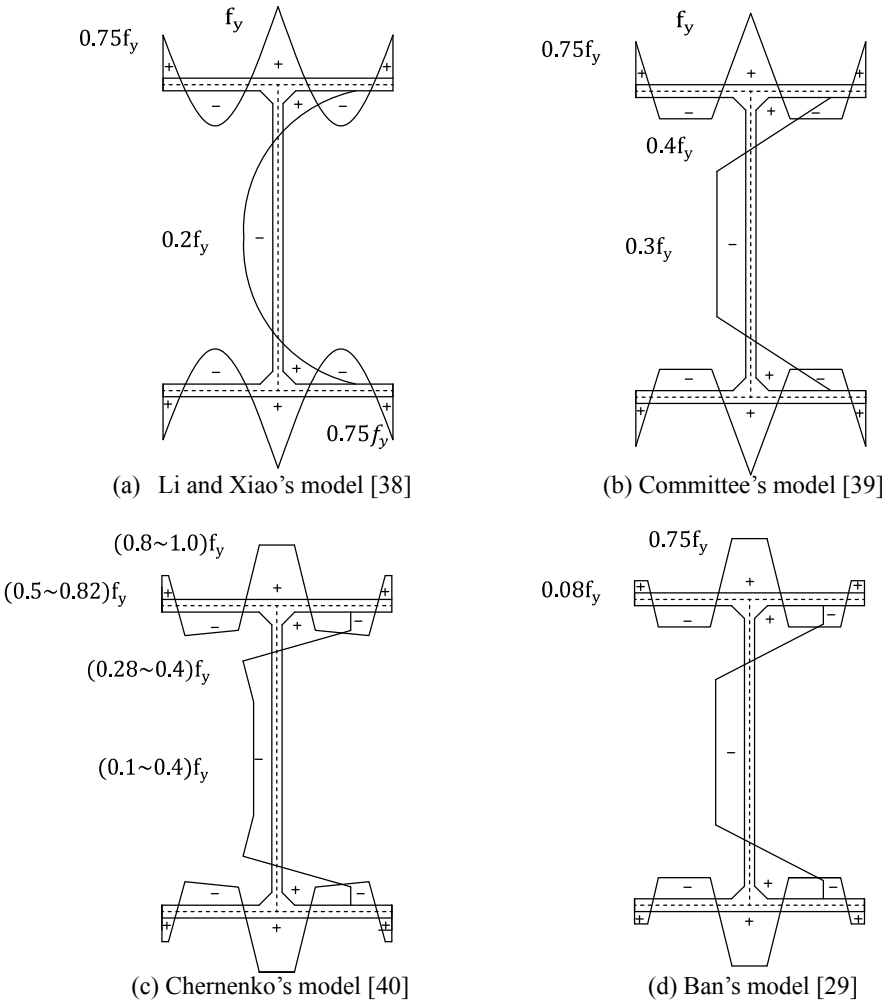

Figure 11. Existing models of residual stress for welded H-sections

7. RESIDUAL STRESS DISTRIBUTION MODEL

Residual stress distribution models are essential for the analysis and design of steel structural members. Figure 11 shows several existing models for welded H-sections. Chinese standard for steel structures [17] adopts Li and Xiao's model [38] and the model recommended by the code committee [39] for welded H-sections, which were mainly based on experiment tests on normal steel sections, regardless of steel grades and dimensions. Chernenko and Kennedy [40] proposed a residual stress distribution model after summarising available experimental data. Another model by Ban et al. [29] was based on the experimental tests on welded 460 MPa steel H-sections. In the model, tensile stresses were constant and compressive stresses were defined as a function of the plate thickness and width-to-thickness ratio.

In accordance with experimental results of welded Q345GJ steel H-sections, a residual stress model is proposed. Figures 12(a) and (b) show the data of residual stresses in the web and flanges. It is observed that the magnitude of residual stresses at the tip of flame-cut flanges is quite limited, ranging from $-0.18f_y$ to $0.18f_y$, much smaller than that suggested other models. Thus, a tensile stress value of $0.03f_y$ at the flange tip is suggested in the proposed model. In the flange, the mean value of peak tensile residual stresses is equal to $0.67f_y$, and the compressive residual stress is determined as $-0.22f_y$. In the web, the maximum tensile and compressive residual stresses are $0.96f_y$ and $-0.22f_y$, respectively.

The proposed model is significantly different from existing models in terms of the maximum tensile and compressive residual stresses in the flange, as shown in Figure 13. For instance, the peak tensile residual stress at the flange tip is only $0.03f_y$, much smaller than the values recommended by the Chinese code [17] ($0.75f_y$) and Chernenko and Kennedy [40] ($(0.5\sim0.82)f_y$) for normal steel. In the middle of the flange, the maximum tensile stress is $0.67f_y$, only 67% of the suggested value f_y. Similar results can also be obtained when comparisons are made among the compressive residual stresses in the flange. Nevertheless, limited differences exist between the residual stresses in the web calculated from the proposed and available models. It should be mentioned that the suggested residual stress distribution model is derived for welded Q345GJ H-sections with height-to-width ratios greater than 1.5 and plate thickness of about 10 mm. More experimental tests are needed for other welded H-sections.

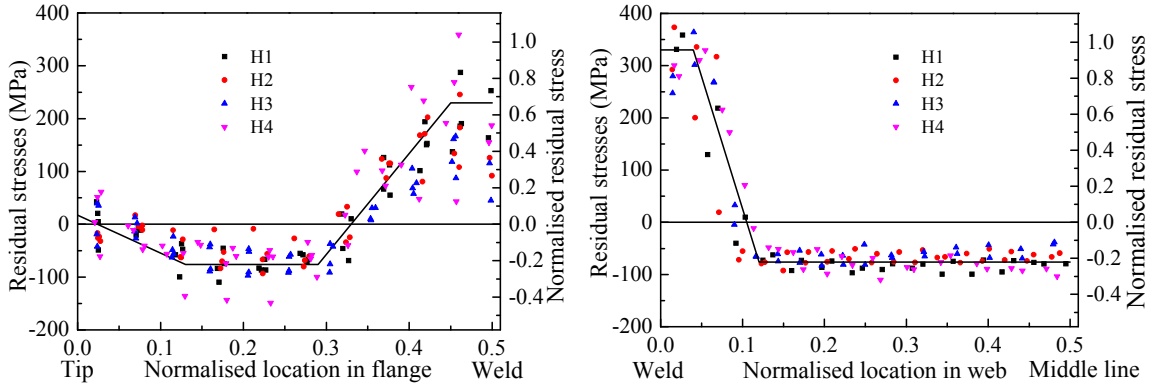

Figure 12. Residual stress distribution in the flange and web

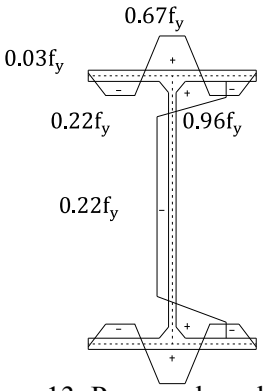

Figure 13. Proposed models of residual stress for welded H-sections

8. CONCLUSIONS

In this paper, the residual stress of four welded H-sections fabricated with flame-cut Q345GJ steel plates was investigated by using the sectioning method. For curved strips after sectioning, different curve correction methods were adopted. In addition to the circular correction method, straightening method was proposed to measure the total length of the middle-thickness layer. By using the methods, residual stresses in the web and flanges were calculated and a residual stress distribution model was developed for welded H-sections. The following conclusions were drawn from the study.

(1) Considerable differences exist between different curve correction methods, especially for curved strips after sectioning. Comparisons of the correction methods show that the parabolic and circular assumptions provide nearly the same results. However, the values are much larger than that calculated from the method by Tebedge and Tall [20].

(2) In the circular curve correction method, the residual stress at the middle-thickness layer of a strip can be determined from the measurements on one surface. However, it is highly sensitive to the strip thickness and strip offset value. Therefore, two surface measurements are still suggested to ensure the accuracy.

(3) Straightening method was proposed to measure the residual stresses in curved strips and the results were in good agreement with that obtained from the circular correction method. The closing error of residual stresses on each section was limited, indicating the accuracy of the proposed method for residual stress calculations. However, by using the straightening method, the number of measurements can be reduced by half. Besides, this method is particularly suitable for strips with large deformations.

(4) The residual stress profile in H-sections welded by Q345GJ steel plates with flame-cut edges was similar to that in welded normal steel H-sections. However, the peak tensile and compressive residual stresses in the flange were much lower than that given by existing models. Moreover, the tensile residual stresses close to welds were irrespective of sectional dimensions, while the compressive residual stresses were directly related to sectional dimensions.
Due to the differences in residual stresses in the flange, welded Q345GJ steel beams is expected to exhibit different behaviour from normal steel sections under vertical loads. Thus, further experimental tests are needed to evaluate the stability resistance of welded Q345GJ steel H-sections.

ACKNOWLEDGEMENTS

The authors gratefully acknowledge the financial supports provided by the National Natural Science Foundation of China (No. 51078368 and No. 50808185) and the Fundamental Research Funds for the Central Universities (No. CDJZR12200007).

REFERENCES

[1] Pocock, G., "High Strength Steel Use in Australia, Japan and the US", Structural Engineer, 2006, Vol. 84, No. 21, pp. 27-31.
[2] European Committee for Standardization, Eurocode 3: Design of steel structures: Part 1-12: Additional Rules for the Extension of EN 1993 up to Steel Grades S700, EN 1993-1-12, 2007.
[3] American Institute of Steel Construction, Specification for Structural Steel Buildings, ANSI/AISC 360-10, Chicago, Illinois, 2010.
[4] Standard Australia, Steel Structures, AS4100-1998, 1998.
[5] Graville, B.A., "Cold Cracking in Welds in HSLA Steels", International Conference on Welding of HSLA (Microalloyed) Structural Steels, American Society for Metals, 1976.
[6] Japanese Standards Association, Rolled Steel for Building Structure, JISG 3136, Tokyo, 2012.
[7] American Society for Testing and Materials, Standard Specification for Structural Steel Shapes, A922/A922M, West Conshohocken, PA, 2011.
[8] Bjorhovde, R., "Development and Use of High Performance Steel", Journal of Constructional Steel Research, 2004, Vol. 60, No. 3, pp. 393-400.
[9] Shi, Y.J., "Development and Application of High Strength and High Performance Steel in Buildings", The 3rd International Forum on Advances in Structural Engineering, Beijing, 2009.
[10] Stanardization Administration of China, Steel Plates for Building Structure, GB/T 19879-2005, Beijing, Standards Press of China, 2005 (in Chinese).
[11] Stanardization Administration of China, Carbon structural steels, GB/T 700-2006, Beijing, Standards Press of China, 2006 (in Chinese).
[12] Stanardization Administration of China, High strength low alloy structural steels, GB/T 1591-2008, Beijing, Standards Press of China, 2008 (in Chinese).
[13] Nie, S.D., Dai, G.X. and Yang, B., "Development and Application of High-performance GJ Steel in Construction Practices", The 9th National Modern Structure Conference, Jinan, 2009 (in Chinese).
[14] Fan, Z., Wu, X.M. and Yu, Y.Q., "Revised Preliminary Design of Steel Structure of National Stadium Beijing", Spatial Structures, 2005, Vol. 11, No. 3, pp. 3-13 (in Chinese).
[15] Chen, L.R., "The characteristics of structural steel for the main building in new location of China Central Television Station", Steel Structures, 2007, Vol. 22, No. 91, pp. 1-4 (in Chinese).
[16] Chen, L.R. and Chai, C., "Overview of Steel Consumption of Major Building Steel Structure Engineering", The 4th Symposium of China Steel Construction Association & National Steel Structural Congress 2006, Beijing, 2006 (in Chinese).
[17] Ministry of Construction, Code for design of steel structures, GB 50017-2003, Beijing, China Archetecture & Building Press, 2003 (in Chinese).
[18] Wei, M.Z., "Steel Structures", Wuhan University of Technology Press, 2000 (in Chinese).

[19] Ziemian, R.D., "Guide to Stability Design Criteria for Metal Structures", John Wiley & Sons, Inc, 2010.
[20] Tebedge, N., Alpsten, G. and Tall, L., "Residual-stress Measurement by the Sectioning Method", Experimental Mechanics, 1973, Vol. 13, No. 2, pp. 88-96.
[21] Wang, G.Z. and Zhao, W.W., "Residual Stress Measurement in Welded and Hot-rolled I section Steels", Industrial Construction, 1986, Vol. 16, No. 7, pp. 32-37 (in Chinese).
[22] Alpsten, G.A. and Tall, L., "Residual Stresses in Heavy Welded Shapes", Welding Research Supplement, 1970, Vol. 49, pp. 93-105.
[23] Rasmussen, K.J.R. and Hancock, G.J., "Tests of High Strength Steel Columns", Journal of Constructional Steel Research, 1995, Vol. 34, No. 1, pp. 27-52.
[24] Rasmussen, K.J.R. and Hancock, G.J., "Plate Slenderness Limits for High Strength Steel Sections", Journal of Constructional Steel Research, 1992, Vol. 23, No. 1, pp. 73-96.
[25] Wang, Y.B., Li, G.Q. and Chen, S.W., "The Assessment of Residual Stresses in Welded High Strength Steel Box Sections", Journal of Constructional Steel Research, 2012, Vol. 76, pp. 93-99.
[26] Wang, Y.B., Li, G.Q. and Chen, S.W., "Residual Stresses in Welded Flame-cut High Strength Steel H-sections", Journal of Constructional Steel Research, 2012, Vol. 79, pp. 159-165.
[27] Ban, H.Y., Shi, G. and Shi, Y.J., "Residual Stress Tests of High-strength Steel Equal Angles", Journal of Structural Engineering, 2012, Vol. 138, No. 12, pp. 1446-1454.
[28] Ban, H.Y., Shi, G., Shi, Y.J. and Wang, Y.Q., "Residual Stress of 460 MPa High Strength Steel Welded Box Section: Experimental Investigation and Modeling", Thin-Walled Structures, 2013, Vol. 64, pp. 73-82.
[29] Ban, H.Y., Shi, G., Bai, Y., Shi, Y.J. and Wang, Y.Q., "Residual Stress of 460 MPa High Strength Steel Welded I Section: Experimental Investigation and Modeling", International Journal of Steel Structures, 2013, Vol. 13, No. 4, pp. 691-705.
[30] Spoorenberg, R.C, Snijder, H.H., Cajot, L.G. and May, M.S., "Experimental Investigation on Residual Stresses in Heavy Wide Flange QST Steel Sections", Journal of Constructional Steel Research, 2013, Vol. 89, pp. 63-74.
[31] General Administration of Quality Supervision Inspection and Quarantine, Steel and steel products-Location and preparation of test pieces for mechanical testing, GB/T 2975-1998, Beijing, Standards Press of China, 1998 (in Chinese).
[32] Stanardization Administration of China, Metallic materials-Tensile testing-Part 1: Method of Test at Room Temperature, GB/T 228.1-2010, Beijing, Standards Press of China, 2010 (in Chinese).
[33] Ban, H.Y., Shi, G. and Xing, H.J., "Stability of Q420 High Strength Steel Equal-leg Angle Members under Axial Compression (I): Experimental Study on the Residual Stress", China Civil Engineering Journal, 2010, Vol. 43, No. 7, pp. 14-21 (in Chinese).
[34] Wang, Y.Q., Guan J., Zhang, Y., Shi, Y.J. and Yang, L., "Experimental Study on Residual Stress of Austenitic Stainless Steel 316 in Fabricated I-sections", Industrial Construction, 2012, Vol. 42, No. 5, pp. 44-50 (in Chinese).
[35] Cui, J., "Influence of Residual Stress on the Resistance of Welded I Sections Fabricated with Flame-cut Plates", Chongqing Institute of Archetecture and Engineering, Chongqing, 1983 (in Chinese).
[36] Sherman, D.R., "Residual Stress Measurement in Tubular Members", Journal of the Structural Division, 1969, Vol. 95, No. 4, pp. 635-647.
[37] Structural Stability Research Council, "Determination of Residual Stresses in Structural Shapes", Experimental Techniques, 1981, Vol. 5, No. 3, pp. 4-7.

[38] Li, K.X. and Xiao, Y.H., "Column Curves for Steel Compression Members", Journal of Chongqing Institute of Archetecture and Engineering, 1985, Vol. 1, pp. 24-33 (in Chinese).
[39] Committee for Code for Design of Steel Structures, Application of Code for Design of Steel Structures in China, Beijing, China Planning Press, 2003 (in Chinese).
[40] Chernenko, D.E. and Kennedy, D.J.L., "An Analysis of the Performance of Welded Wide Flange columns", Canadian Journal of Civil Engineering, 1991, Vol. 18, No. 4, pp. 537-555.

ORDER FORM

ISSN 1816-112X

Advanced Steel Construction, an international journal

Indexed by the Science Citation Index Expanded, Materials Science Citation Index and ISI Alerting Services

From: _____

To: ***Secretariat, Advanced Steel Construction, an international journal***
Fax: (852) 2334-6389

I/ We would like to enter a subscription to the ***International Journal of Advanced Steel Construction (IJASC)*** *published by The Hong Kong Institute of Steel Construction.*

Please complete the form and send to:

International Journal of Advanced Steel Construction
c/o Department of Civil and Environmental Engineering
The Hong Kong Polytechnic University
Hunghom, Kowloon, Hong Kong

Fax: (852) 2334-6389 Email: ceslchan@polyu.edu.hk

Published by : The Hong Kong Institute of Steel Construction
Website: http://www.hkisc.org/

Please tick the appropriate box

- ❑ Please enter my hard-copy subscription **(4 issues per year)**.
- ❑ Please send me a complimentary copy of the *Advanced Steel Construction, an International Journal (IJASC).*

Please tick the appropriate box(es)

	Print	**On-line is free**
Personal	❑ US$ 125	
Institutional	❑ US$ 280	

Total Amount **US$** _____

Methods of payment *(please tick the appropriate box(es))*

- ❑ Please invoice me
- ❑ Cheque enclosed for US$ _____ payable to Hong Kong Institute of Steel Construction Limited (No personal cheque accepted)

Ship to

Name (Prof./ Dr./ Mr./ Ms.) _____
Address _____
_____
_____
City/ State/ Postal Code _____
Country _____
Email _____ Fax _____